CHEMICAL REVIEWS

pubs.acs.org/CR

Review

Electrically Conductive Metal–Organic Frameworks

Lilia S. Xie,[†] Grigorii Skorupskii,[†] and Mircea Dincă*

Cite This: *Chem. Rev.* 2020, 120, 8536–8580

Read Online

ACCESS | Metrics & More | Article Recommendations

ABSTRACT: Metal–organic frameworks (MOFs) are intrinsically porous extended solids formed by coordination bonding between organic ligands and metal ions or clusters. High electrical conductivity is rare in MOFs, yet it allows for diverse applications in electrocatalysis, charge storage, and chemiresistive sensing, among others. In this Review, we discuss the efforts undertaken so far to achieve efficient charge transport in MOFs. We focus on four common strategies that have been harnessed toward high conductivities. In the "through-bond" approach, continuous chains of coordination bonds between the metal centers and ligands' functional groups create charge transport pathways. In the "extended conjugation" approach, the metals and entire ligands form large delocalized systems. The "through-space" approach harnesses the π–π stacking interactions between organic moieties. The "guest-promoted" approach utilizes the inherent porosity of MOFs and host–guest interactions. Studies utilizing less defined transport pathways are also evaluated. For each approach, we give a systematic overview of the structures and transport properties of relevant materials. We consider the benefits and limitations of strategies developed thus far and provide an overview of outstanding challenges in conductive MOFs.

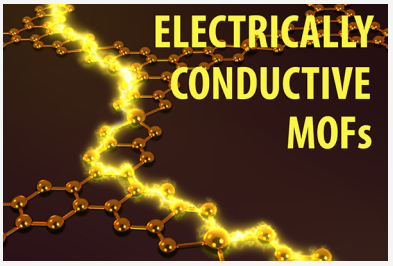

CONTENTS

1. INTRODUCTION

Metal–organic frameworks (MOFs) are a class of porous materials with high surface areas consisting of inorganic nodes connected by organic linkers.[1−3] Since the inception of the

Special Issue: Porous Framework Chemistry

Received: November 26, 2019
Published: April 10, 2020

https://dx.doi.org/10.1021/acs.chemrev.9b00766
Chem. Rev. 2020, 120, 8536–8580

field in the late 1990s and early 2000s, these materials have been investigated extensively for applications, such as gas storage,[4−7] separations,[8−11] and catalysis,[12−15] because of their high porosity and chemical tunability. In contrast, the electronic properties of MOFs have received comparatively little attention until recently, and the potential of this class of materials as electrically conductive porous materials has only begun to be realized. Despite the relative youth of this research area, many advances in designing, synthesizing, and characterizing electrically conductive MOFs have been made, and the field has experienced considerable expansion in just the last five years, the focus period for this Review (Figure 1)

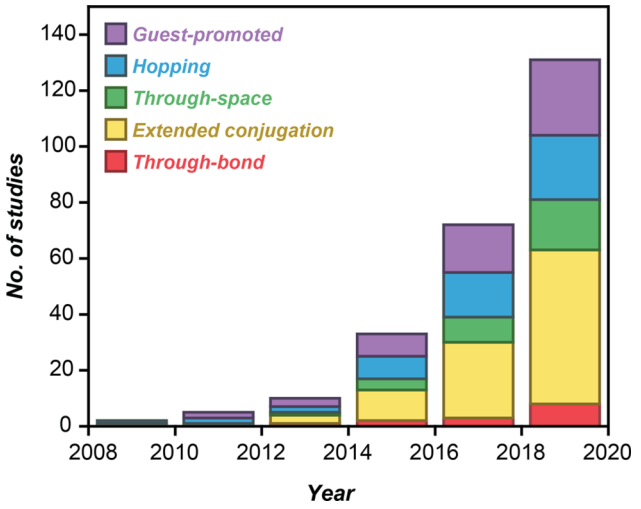

Figure 1. Histogram showing cumulative number of papers focusing on aspects of electrical conductivity in MOFs from 2008 to 2019, grouped according to the design strategy employed.

Electrically conductive MOFs are of considerable interest from many perspectives. They are relevant as active materials for many applications, including electrocatalysis,[16−20] chemiresistive sensing,[21−26] and energy storage technologies.[27−30] Their fundamental transport properties merit further study, as certain conductive MOFs have been predicted to host topologically nontrivial electronic structures.[31−36] Additionally, they may contain arrangements of inorganic or organic moieties that are unprecedented in other materials, potentially giving rise to new physical phenomena.[37,38] They also present exciting new avenues for creativity in ligand design, self-assembly, and crystal engineering.

This Review covers recent advances in the chemistry of this class of materials, with emphasis on design principles, experimental materials discovery, and characterization of transport properties. We focus the majority of our discussion on crystalline coordination networks with potential voids[39] with two- and three-dimensional connectivities for which electrical conductivity values are reported. Where appropriate, we also review chemically related materials (as demonstrated by compositional and structural characterization) that do not exhibit permanent porosity. While it is important to understand the mechanisms underlying the transport properties of the most conductive MOFs, we believe it can be equally instructive to examine structure−property relationships among materials that may not exhibit record conductivity values. In an effort to capture the granularity necessary to establish broader trends, the conductivities of the materials included in this Review span more than 17 orders of magnitude.

Many other reviews pertaining to electrically conductive MOFs have appeared in recent years. Sun et al. first provided an overview of porous conductive MOFs in 2016,[40] and Medina et al. provided an update to this work.[41] Several other perspectives on conductive MOFs, their applications, and outlooks have been written.[42−46] Ko et al.,[47] Zheng et al.,[48] and Solomos et al.[49] have focused on two-dimensional (2D) conductive MOFs, and Murase et al. analyzed mixed valency in conductive MOFs.[50] Application-focused reviews have covered electrocatalysis[51] and chemiresistive sensing.[52−54] Stassen et al. reviewed MOF integration into electronic devices.[55] Sun et al. described techniques for measuring the conductivity of MOFs.[56] For a critical review of mostly nonporous conductive coordination polymers, we direct readers to the work of Givaja et al.[57]

1.1. Design Strategies and Mechanisms

Electrical conductivity is a characteristic of a material that quantifies the efficacy of the transport of electrical charge. It is a convolution of the charge carrier concentration, n, and the carrier mobility, μ.[58] Control over either of these quantities is nontrivial and requires deep understanding of the electronic structure of the material, as well as the mechanisms underlying charge transport.

From a fundamental perspective, charge transport in solids can be described by one of two general mechanisms: hopping transport and ballistic (or band-like) transport (Figure 2).[40] In the former, the charges transfer between discrete, nonbonded sites, where the charge carriers are localized. This mechanism is common to disordered materials, glasses, and organic semiconductors. In the latter, strong interactions between the sites allow for formation of continuous energy bands with delocalized charge carriers. This mechanism is often found in crystalline inorganic materials.

In chemical terms, an analogy can be made between these two mechanisms and the Robin−Day classification of mixed-valence compounds.[59] In a material with strong covalent bonding, where we would expect band-like transport, the electrons are delocalized between the different states—similar to that of a class III mixed-valence compound. In contrast, charge transport in more ionic materials is better described by the hopping mechanism. In these cases, distinct sites with differing valences exist, and additional energy has to be applied to transfer the electron between them—similar to a class II mixed-valence compound. (Insulating materials with very low conductivities are analogous to class I mixed-valence compounds, in which the valences are trapped and even hopping is inaccessible.)

The key difference in observable parameters for the two mechanisms lies in the temperature dependence of conductivity. Hopping-type conductivity is always thermally activated: higher temperatures lead to higher conductivities. This dependence follows an exponential law and is described by $\sigma = \sigma_0 \exp[-(T_0/T)^{1/d}]$, where σ is the conductivity, T is the temperature, T_0 and σ_0 are constants specific to the material, and d is the dimensionality of the sample.[60,61]

In contrast to hopping, band-like transport can be both thermally activated and deactivated. In metallic materials with sufficiently high carrier concentrations, the conductivity is limited by various scattering processes, which are enhanced at higher temperatures, leading to less efficient transport. In

https://dx.doi.org/10.1021/acs.chemrev.9b00766
Chem. Rev. 2020, 120, 8536−8580

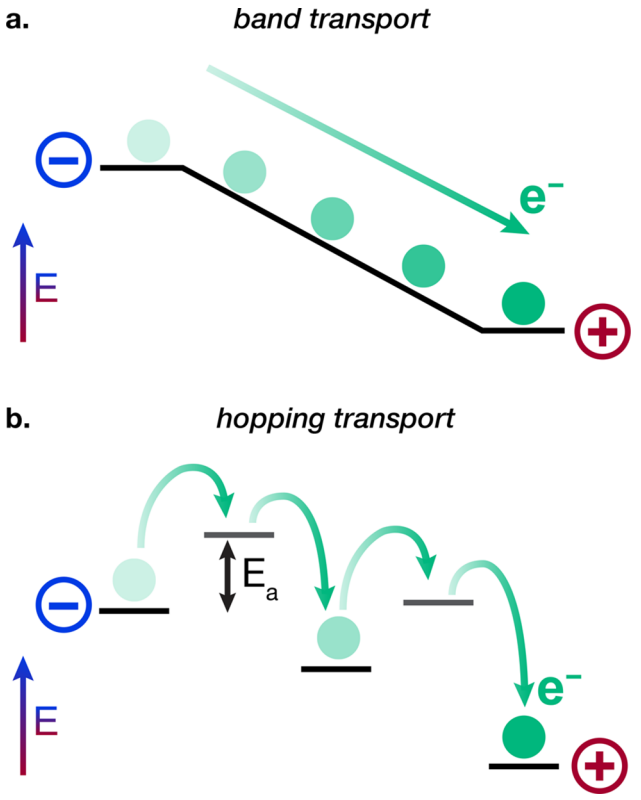

Figure 2. Schematic representations of (a) ballistic band-like charge transport and (b) hopping charge transport. In both modes of transport, electrons move from high to low electric potential energy (denoted as E). In band-like transport, movement of electrons proceeds along a smooth energy landscape, while in hopping transport, movement of electrons is gated by activation barriers (denoted as E_a).

semiconductors, the conductivity is generally limited by the charge carrier concentration. At higher temperatures, more free holes or electrons are generated, giving higher conductivities. Because very few MOFs are metallic, the specific temperature dependences for metals will not be discussed. The conductivity of semiconductors often follows an Arrhenius dependence, $\sigma = \sigma_0 \exp[-(E_a/kT)]$, where E_a is the activation energy. The value of E_a is tied to the width of the band gap, as well as the energy levels of dopants.[58]

The generalized electronic band structures of an insulator, semiconductor, and metal are illustrated in Figure 3. Generally, an insulator is defined by a large band gap (E_g), usually in excess of ∼4 eV, which results in very low population of the conduction band. A semiconductor has an intermediate E_g that allows promotion of free charge carriers to the conduction band (e.g., by thermal or optical excitation). A metal contains at least one band crossing the Fermi level (E_F), resulting in a continuum of allowed electronic states that leads to high conductivities.

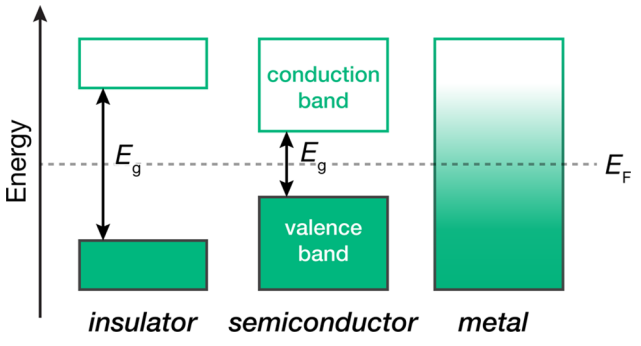

Figure 3. Electronic structures of a generic insulator, semiconductor, and metal, where E_g is the band gap and E_F is the Fermi level.

In practice, many factors complicate the determination of charge transport mechanisms. Specifically for conductive MOFs, two key issues are involved. First, most measurements in the literature have been carried out on polycrystalline pellets, and not on single crystals. This adds an inherent thermally activated contribution to the resistance from hopping between different grains of the material.[62] Second, significant disorder or defects can lead to creation of trap states, where charge carriers will be localized and would need to hop between.[60,61] It is also easy to imagine, for instance, how a missing linker defect could break up a charge transport pathway and create a barrier to charge transport; other types of defects would have similar effects.[63]

Ultimately, a decisive determination of the charge transport mechanism in a material would involve a combination of variable temperature *single-crystal* conductivity studies, electronic structure calculations, and optical spectroscopy, at the minimum. Few studies, however, provide such in-depth investigation of charge transport in MOFs, making the actual underlying mechanisms difficult to discuss in the context of this Review. Therefore, we have opted to discuss the approaches that researchers have applied to designing conductive MOFs and how successful these strategies have been.

Much of the early work on electrical transport in MOFs took inspiration from similar work on coordination polymers,[64] covalent organic frameworks (COFs),[37] and molecular conductors.[65] In fact, conductive MOFs can be thought of as porous molecular conductors, given that they are indeed composed of molecular building blocks. The general approaches taken toward achieving high conductivities in MOFs also originate from these more established fields. Two key strategies in particular are the so-called *through-bond* and *through-space* approaches. The former focuses on improving bonding between the metal and the ligands to achieve stronger charge delocalization; the latter targets noncovalent interactions between organic fragments, particularly $\pi-\pi$ stacking, to introduce continuous charge transport pathways. We anticipate that the nature of the transport pathways may affect the transport properties in MOFs, coordination polymers, COFs, and other conductors in similar ways despite other differences in the nature of these materials.

A number of unique characteristics of MOFs, however, tend to limit direct applications of these strategies. In particular, the inherent porosity of MOFs precludes close intermolecular contacts in many structural types, particularly in isotropic structures (i.e., high-symmetry structures where charge transport pathways are identical in all three crystallographic directions). In addition, the majority of MOFs are formed with carboxylate linkers, which usually form relatively ionic bonds with the metals, leading to large energy gaps and trapped valences/confined electronic states. That said, the chemical and structural tunability of MOFs, as well as their unique host−guest chemistry, have allowed for these approaches to evolve and produce materials with a variety of motifs favorable for conductivity (encompassing inorganic and

https://dx.doi.org/10.1021/acs.chemrev.9b00766
Chem. Rev. 2020, 120, 8536−8580

organic components). Below, we give a broad overview of the current form of these approaches toward achieving electrical conductivity in MOFs (Figure 4).

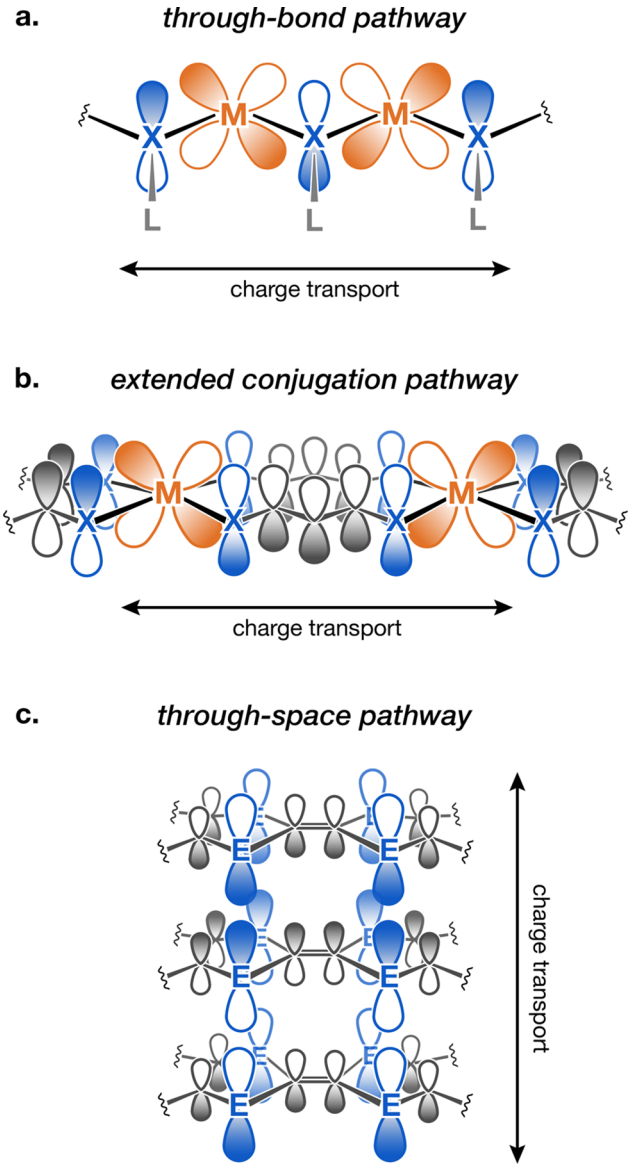

Figure 4. Orbital representations of potential charge transport pathways operative in MOFs. (a) The through-bond pathway involves orbitals from the metal and ligand functional groups. (b) The extended conjugation pathway also involves π–d conjugation including the ligand core (both are shown here for M = a transition metal). (c) The through-space pathway involves π–π stacking of organic moieties (E = S for tetrathiafulvalene, a common component in MOFs).

1.1.1. Through-Bond Pathways. Networks of coordination bonds in MOFs can form continuous routes for charge delocalization. In this work, we refer to bonding motifs involving metals and the ligand functional group (but not the organic core) as *through-bond* pathways. MOFs with continuous SBUs comprising metals and ligand moieties with well-matched energy levels and good orbital overlap can result in small band gaps and high charge mobilities, both of which are favorable for conductivity. Examples of 1D (most common)[66−70] and 3D pathways (much rarer)[68,71,72] have both been reported.

Many reports in this category focus on softer, more electropositive linkers, with sulfur or nitrogen coordinating to the metals, in which the energy matching and metal−ligand orbital overlap are improved.[66−68] Fe-based MOFs, particularly those with azolate ligands containing mixed-valent $Fe^{II/III}$ centers, exhibit the highest conductivities in this class of materials.[68−70,72] These directions follow principles previously demonstrated for inorganic chalcogenide chains,[73] as well as conducting metallopolymers.[74]

1.1.2. Extended Conjugation. Pairing transition metals with ligands containing chelating functional groups (e.g., ortho-diols, diamines, and dithiols) that are conjugated with the organic core results in frameworks with extended conjugation encompassing both the organic and inorganic components. Some of these MOFs with 2D structures have been proposed to be metal−organic analogs of graphene, referring to the similarity between their extended π–d conjugation within the *ab* plane, and the sp^2 hybridization of graphene. This π–d conjugation allows for efficient delocalization of charge carriers within the plane, with such frameworks exhibiting the highest conductivities for MOFs.[21,30,75−79]

The organic linkers found in MOFs with extended conjugation include dihydroxybenzoquinone, chloranilic acid, and hexa-substituted triphenylenes and benzenes. The redox-active nature of these aromatic cores is also important for enhancing conductivity: many of these ligands are partially oxidized during solvothermal growth, introducing charge carriers into the as-synthesized frameworks.

For the majority of the 2D-connected frameworks, charge transport within the π–d conjugated planes has been invoked to be the dominant mechanism behind conductivity. We note, however, that π–π interlayer interactions in the bulk structures may also be important for contributing to charge delocalization.

1.1.3. Through-Space Pathways. Organic components participating in π–π interactions with one another can form *through-space* charge transport pathways. For organic semiconductors, it is well-established that the spatial separation is inversely correlated with the magnitude of the transfer integral and hence the charge mobility.[80] In an analogous way, linkers that have a high propensity for π–π interactions can yield MOFs with high conductivities originating from the organic components. Work in this direction can be seen as extension of prior research on dense coordination polymers based on tetracyanoquinodimethane (TCNQ), which show electrical conductivities above 0.1 S/cm.[81−83]

Several well-known building blocks in organic electronics have been incorporated into conductive MOFs with through-space charge pathways. For example, MOFs with ligands based on tetrathiafulvalene (TTF), an electron-rich organosulfur molecule, exhibit conductivities varying systematically with the stacking distance between the ligands.[84−88] Conductive naphthalene-, anthracene-, and naphthalenediimide-based MOFs also exhibit π–π stacking.[38,89−91]

For conductive 2D MOFs that are fully conjugated within the *ab* plane, the role of through-space conductivity (i.e., transport along the *c* direction) remains to be fully elucidated. However, recent studies on triphenylene-based MOFs suggest charge transport through π–π stacking indeed contributes to the high bulk conductivities observed.[79,92]

https://dx.doi.org/10.1021/acs.chemrev.9b00766
Chem. Rev. 2020, 120, 8536−8580

1.1.4. Redox Hopping. In practice, it is difficult to unambiguously distinguish between the two general mechanisms through which charge transport in MOFs can proceed (i.e., band-like transport and charge hopping transport). Even in structures with ostensible high-mobility transport pathways, real defect concentrations are unknown, and grain boundary resistances in polycrystalline samples may obfuscate the intrinsic behavior. Hence, hopping conduction cannot be ruled out, especially at lower temperatures. However, for frameworks in which no crystallographic pathways that could facilitate band-like transport can be identified, it is reasonable to assume that conductivity proceeds via a hopping mechanism (Figure 5). In such materials, the presence of redox-active metals or linkers, as well as small spatial separation between these components, can promote charge hopping.

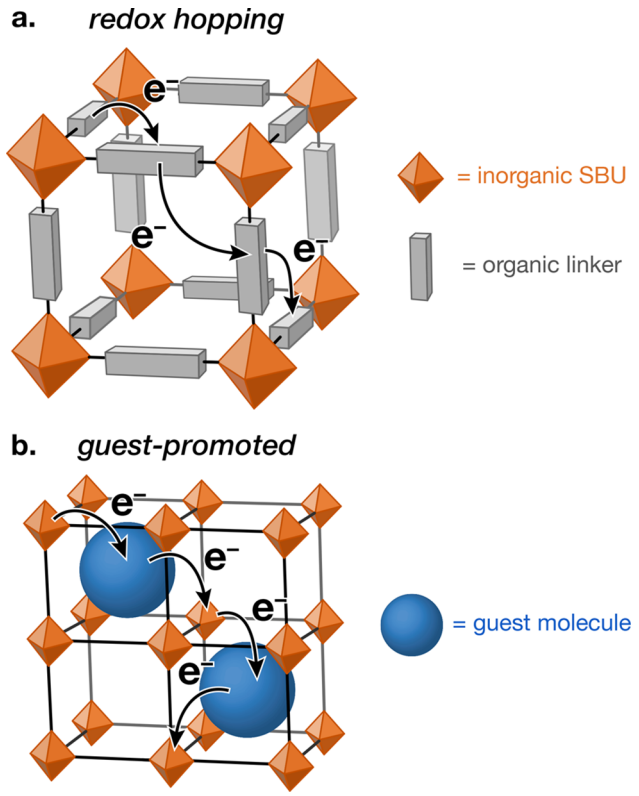

Figure 5. Schematic representations of electron transport via (a) a redox hopping mechanism between organic linkers and (b) a guest-promoted pathway involving host–guest interactions between the inorganic framework nodes and guest molecules.

1.1.5. Guest-Promoted Transport. The porosity of MOFs can present both a challenge and an opportunity with respect to conductivity. Many researchers have exploited the porosity of MOFs to induce conductivity by postsynthetically loading electroactive guest molecules into the framework. These guests then form charge transport pathways throughout the material through guest–guest or guest–framework interactions. A diverse set of approaches to introducing conductivity pathways into such materials exist, encompassing both the aforementioned strategies translated to host–guest interactions, as well as entirely new directions, such as incorporation of extended solid state or polymeric materials within the pores. In all cases involving this strategy, it should be noted that porosity is either significantly reduced or even completely eliminated, as may be expected by occupying the pores with bulky guests.

1.2. Electronic Structures of MOFs

Electronic energy levels in MOFs, like other extended solids, are conveniently represented as band structures, where the energies of orbitals are plotted versus *k*-space (the crystal momentum).[93] Although experimental band structures and densities of states (defined as the number of energy levels versus energy) can be probed using photoemission spectroscopies, in practice, these techniques have only rarely been applied to MOFs.[94,77] Therefore, the vast majority of band structures for MOFs are computed using density functional theory (DFT) calculations. They are commonly referenced to the electrostatic potential inside a pore.[95]

The calculated band structures for representative MOFs with insulating, semiconducting, and metallic electronic structures are shown in Figure 6. $Zn_4O(BDC)_3$ (BDC = benzene-1,4-dicarboxylate), or MOF-5, has a band gap of 4.6 eV, indicating that it is an insulator.[45] The majority of reported MOFs are expected to be insulators as well due to large energy gaps between their frontier orbitals. The computed band gap of Zn_2(TTFTB) (TTFTB = tetrathiafulvalene tetrabenzoate) is approximately 1.75 eV,[84] a typical value for a semiconductor. We note that, in the case of Zn_2(TTFTB), the computed electronic band gap and the optical band gap from a Tauc plot (2.0 eV) are in reasonable agreement.[96] However, in the absence of transport measurements, optical band gaps alone are not sufficient to determine that a compound is a semiconductor. Finally, the calculated band structure of $Ni_3(HIB)_2$ (HIB = hexaiminobenzene) contains bands crossing the Fermi level, suggesting metallic character.[77] Ultraviolet photoemission spectroscopy showed a nonzero density of states at the Fermi level, consistent with metallicity. Although temperature-dependent conductivity for polycrystalline samples of this compound indicated thermally activated transport, in seeming contradiction with the metallic nature predicted by computations, the authors proposed that scattering at grain boundaries dominated transport, which is otherwise metallic within each particle. The accuracy of a computed electronic band structure is necessarily determined by the quality of the input crystal structure and the functional used. Significant structural disorder and large unit cells in many MOFs can introduce considerable challenges for band structure calculations. The relevance of computed band structures to the real transport properties of a MOF should, therefore, always be considered in relation to the structural integrity of the model and practical constraints on computational resources.

1.3. Practical Considerations

To achieve fundamental understanding of charge transport in MOFs, it is necessary to deconvolute carrier concentration and mobility. Mobility can be obtained directly with noncontact measurements such as time-resolved terahertz spectroscopy (TRTS) or flash-photolysis time-resolved microwave conductivity (FP-TRMC). Hall effect measurements and field-effect transistors (FET) also allow determination of carrier mobility and identity (i.e., whether electrons or holes are the majority carriers). However, all of these measurements are challenging and have steep requirements for sample quality and preparation and, thus, have been rarely undertaken in MOFs. Furthermore, results obtained from one technique are not easily compared with those from other techniques. For instance, whereas FP-TRMC reports intrinsic mobility values,

https://dx.doi.org/10.1021/acs.chemrev.9b00766
Chem. Rev. 2020, 120, 8536–8580

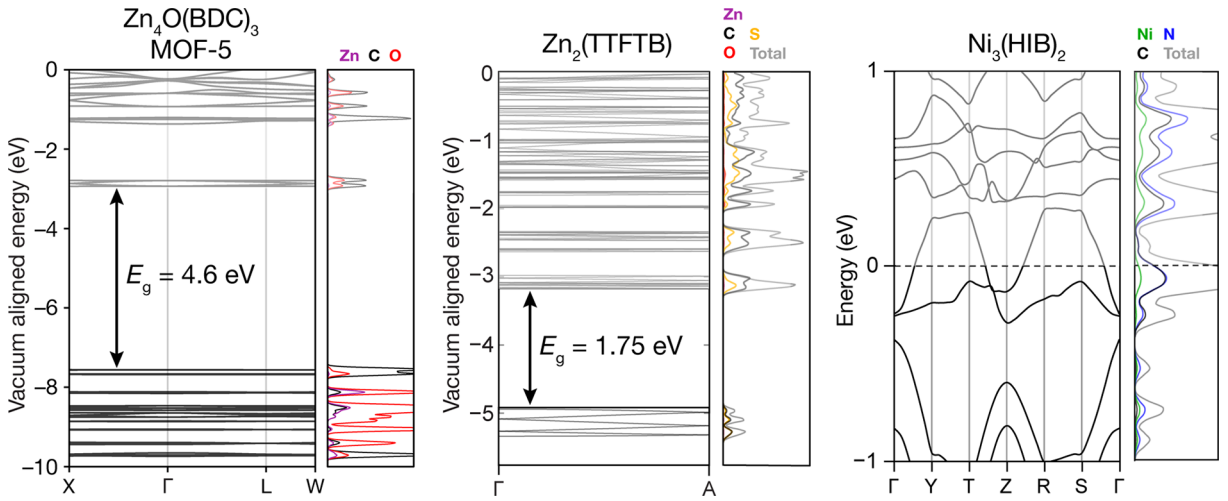

Figure 6. Calculated electronic band structures and densities of states for an insulating MOF, $Zn_4O(BDC)_3$ (MOF-5);[45] a semiconducting MOF, $Zn_2(TTFTB)$;[84] and a metallic MOF, $Ni_3(HIB)_2$.[77]

these are alternating current mobility values that cannot and should not be compared on a one-to-one basis with mobility values obtained from FET devices, which normally operate under direct current. As a result of all these factors, the majority of publications in this area simply report conductivity values without attempting to probe mobility or carrier concentration. Ideally, mobility values from contact (Hall or FET) measurements are preferable to supplement conductivity values because they provide additional insight into transport properties.

A number of previous reports described in detail the various methods of measuring electrical conductivity on MOFs and other coordination polymers.[56,57] Briefly, conductivity can be measured on either single crystals or on polycrystalline samples in the form of films or powders. Although clearly more technically challenging, single-crystal measurements are preferred because they eliminate contributions from grain boundary resistance, sample anisotropy, and other factors apart from the intrinsic conductivity of the material. In practice, however, because of particle size considerations and the considerable skill and effort required to produce single-crystal devices for many samples, powder or film measurements are used instead. Powders are generally pressed into compact pellets, while films are usually grown on or transferred onto insulating substrates to ensure that only the MOF material contributes to the measured conductivity.

Conductivity measurements—regardless of whether they are carried out on powders, films, or single crystals—are typically performed in either a two-probe or four-probe configuration. The former (Figure 7a) is simpler and involves simply contacting the material with two wires. In the conventional implementation, a known voltage is supplied to the sample, and the current that passes through it is measured to obtain the resistance through Ohm's law. Significant issues may arise when the contact between the wires and the sample is poor, as this configuration does not compensate for contact resistance. The use of the four-probe configuration, in which four wires are attached to the sample, eliminates contributions from contact resistance from the values measured. In the most common linear four-probe configuration, the outer two wires are used to supply a known current, and the inner two wires are used to measure the potential drop caused by the applied

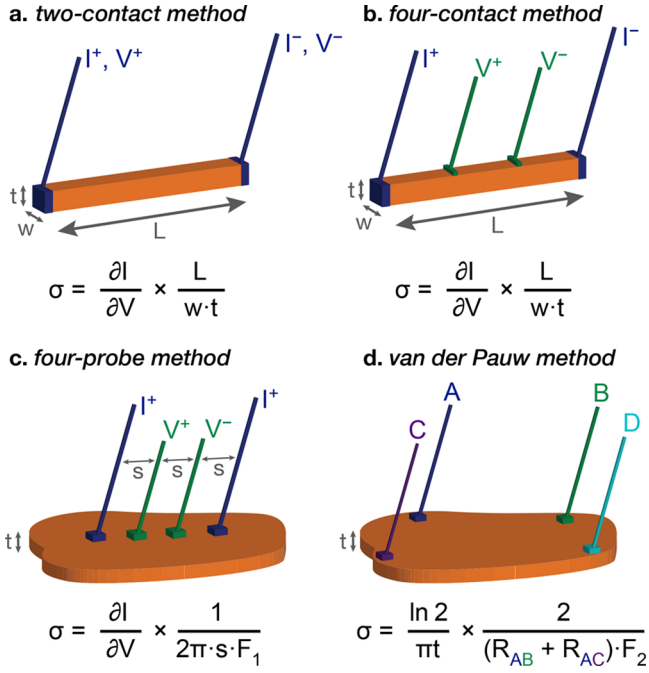

Figure 7. Measurement techniques commonly used for measuring electrical conductivity of MOFs.[56] *I* and *V* denote current and voltage, respectively, and *L*, *w*, and *t* denote the length, width, and thickness of the samples, respectively. *s* denotes the spacing between contacts. R_{AB} and R_{AC} are the resistances measured between contacts A and B and A and C, respectively. F_1 and F_2 are correction factors depending on the geometry of the sample and the values of R_{AB} and R_{AC}, respectively.

current. This method allows for precise determination of the intrinsic resistance of the sample and elimination of contact effects, so long as all contacts are identical and the geometry of the sample is rigorously determined. Other specific configurations for four-probe measurements exist, depending on the morphology of the studied material: for example, the van der Pauw method uses four wires placed around the outer perimeter of a sample.

When four-probe measurements are executed on single crystals, typically the four-contact configuration is used (Figure 7b). In this method, two sets of wires are attached to the material along the direction where the conductivity is being

https://dx.doi.org/10.1021/acs.chemrev.9b00766
Chem. Rev. 2020, 120, 8536−8580

evaluated. It is important that the contacts cover the full width of the crystal in the orthogonal direction to allow good estimates of the cross-section area through which current is passed. Here, the resistance of the device, R, is the numerical derivative of the measured voltage drop with respect to the applied current, in accordance with Ohm's law. The resistivity can be estimated using the formula $\sigma = L/(wtR)$, where L is the distance between the two inner contacts, w is the width, and t is the thickness of the sample.

On extended films and pellets, contact resistance can be analogously minimized with the four-point measurement (Figure 7c). In this case, four small contacts are attached to the surface, equally spaced along a line. The conductivity can be calculated from $\sigma = 1/(2\pi s F_1 R)$, where s is the spacing between the contacts and F_1 is a correction factor dependent on the geometry of the sample.

The van der Pauw method (Figure 7d) is generally less sensitive to the shape of the sample and should be preferred to the linear four-probe configuration when working with non-rectangular samples. For van der Pauw measurements, four small contacts are attached to four corners of the sample. Then, two resistances are estimated, with current applied along one side, and voltage measured along the opposite. Then, the conductivity of the sample is estimated with $\sigma = \frac{\ln 2}{\pi t} \cdot \frac{2}{(R_{AB} + R_{AC})F_2}$, where t is the thickness of the sample, R_{AB} and R_{AC} are the resistances along two orthogonal sides, and F_2 is a correction factor dependent on the two resistances.

The contacts are usually made of precious metals, such as Au, Ag, or Cu, and are attached with conductive adhesive, including carbon, gold, or silver paint, or by depositing a thin layer of metal on the surface of the sample to attach the wires to it. Generally, contact resistances can be minimized by matching the work functions of the sample of interest and the contact materials.

Accurate and precise determination of the conductivities of MOFs is the first step toward evaluating their utility in a range of applications.[51−53] For example, electrode materials in energy storage applications, such as supercapacitors or batteries, typically require relatively high conductivities on the order of 0.1 S/cm or higher.[27−30] High electrical conductivity alone is not sufficient, however, as ionic conductivity is crucial to enable operation at application-relevant currents.[27,29] Engineering composites that incorporate less conductive MOFs may also be a promising approach for energy storage applications.[97−99] For chemiresistive sensing, the requirements for conductivity are more flexible, as the electronics and device design can be tailored to accommodate different conductivities. MOFs showing promise as chemiresistive sensors have conductivities ranging from 10^{-4} to 8 S/cm.[25,100] Generally, the change in conductivity upon interaction with an analyte is more important than the absolute conductivity itself.[52−54] For electrocatalysis, conductivity requirements are likely to vary significantly depending on the rate of the reaction being studied. The higher the rate of the electrochemical reaction, the more stringent the requirements on the MOF conductivity, because electron transport within the electrode (here, the MOF) should not be the rate limiting step in an electrochemical system. MOFs with conductivities between 10^{-5} to 60 S/cm have been explored for different reactions, including oxygen reduction,[17,20] hydrogen evolution,[16] and carbon dioxide reduction.[101]

2. THROUGH-BOND PATHWAYS

The through-bond approach focuses on investigating frameworks with continuous coordination/covalent pathways that can promote efficient charge transport. A number of studies report control over both the carrier concentration and mobility and, thus, the electrical conductivity, owing to the intrinsic tunability of MOFs (Table 1).

In most cases, this approach is realized in frameworks with 1D inorganic SBUs, also known as rod-based MOFs.[102] The majority of such materials employ carboxylate linkers and $(-M-O-)_\infty$ chains. The relatively ionic bonding between transition metals and carboxylates generally leads to poor orbital overlap and low band dispersion—metal and ligand energy levels are relatively localized, leading to low conductivity.

The more successful studies have attempted to solve this issue by increasing the metal−ligand covalency. The general approach so far has been to work with softer ligands, in which the metal-binding atoms are sulfur and nitrogen rather than oxygen. One clear illustration of this concept is substitution of $(-M-O-)_\infty$ chains for $(-M-S-)_\infty$ SBUs in MOF-74/CPO-27 analogs, which led to increased conductivities and mobilities and decreased band gaps.[66,67]

As in most other approaches, the carrier concentration is generally controlled through introduction of mixed-valent species, although it is rarely precisely quantified. Specifically, in pyrazolate, triazolate, and tetrazolate MOFs, $Fe^{II/III}$ mixed valency has resulted in high conductivity values that were tunable and correlated with the concentration of charge carriers.[69−72] Interestingly, the abundance of detailed and systematic structure−function relationship studies for through-bond materials allows us to speculate that the limiting factor for electrical conductivity in many of these MOFs is indeed the carrier concentration: the mixed-valence $Fe^{II/III}$ materials show vastly higher conductivities than those with other *d*-metals, and the conductivities correlate strongly with the extent of mixed valency.

Although the majority of studies investigate rod MOFs with 1D conductivity pathways, select examples with isotropic 3D pathways exist, most notably the framework Fe(1,2,3-triazolate)$_2$.[68,71,72] That said, the vast majority of MOFs containing 1D rod SBUs or other continuous inorganic coordination motifs have not yet been studied for electronic transport, even though stable mixed valency has been demonstrated in some of these other 1D SBUs.[103−105] Applying principles to increase conductivity in through-bond pathways to these unexplored materials is likely to yield new conductive MOFs with even more structural diversity and tunability.

2.1. MOF-74-Type Frameworks

The family of M_2(DOBDC) (M = divalent metal; DOBDC = 2,5-dioxidobenzene-1,4-dicarboxylate) frameworks,[102,106−112] colloquially known as MOF-74 or CPO-27, exhibit 1D hexagonal channels and infinite SBUs consisting of $(-M-O-)_\infty$ chains (Figure 8). In the as-synthesized frameworks, which have the formula M_2(DOBDC)$(DMF)_2$, the metal ions occupy a pseudo-octahedral environment, with one DMF molecule coordinated to each metal center. Removal of this DMF molecule through activation allows for direct modification of the metals' coordination geometry, as well as access to coordinatively unsaturated metal sites.

https://dx.doi.org/10.1021/acs.chemrev.9b00766
Chem. Rev. 2020, 120, 8536−8580

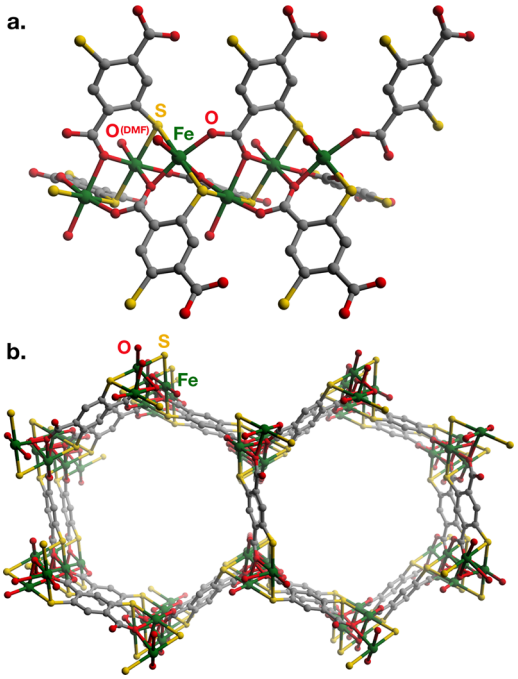

Figure 8. Structure of Fe_2(DSBDC), showing (a) the proposed through-bond conduction pathway comprising $(-Fe-S-)_\infty$ chains, as well as bridging ligand carboxylates and oxygens from coordinated DMF molecules, and (b) hexagonal 1D pores.[67]

In a comparative study of different structural families of rod MOFs, Sun et al. reported the conductivities of seven different M^{II}_2(DOBDC)$(DMF)_2$ materials (M = Mg, Mn, Fe, Co, Ni, Cu, Zn).[68] The conductivities of the Mg, Mn, Co, Ni, Cu, and Zn materials were very low, between 1.4×10^{-14} S/cm for Cu_2(DOBDC)$(DMF)_2$ and 3.0×10^{-13} S/cm for Mn_2(DOBDC)$(DMF)_2$. (Similar conductivity values for these materials were also reported by Scheurle et al.[113])

Sun et al. hypothesized that replacing the hydroxy group of the linker with a thiol group would increase the conductivity of the resulting frameworks due to better energy matching between the frontier orbitals of the thiolate and the metal. Indeed, the framework Mn_2(DSBDC)$(DMF)_2$ (DSBDC = 2,5-disulfidobenzene-1,4-dicarboxylate) exhibited a higher conductivity by about 1 order of magnitude (2.5×10^{-12} S/cm) than Mn_2(DOBDC) (3.9×10^{-13} S/cm).[66,67] The conductivities of the Fe analogs were approximately 6 orders of magnitude higher than those of the Mn materials, with the DSBDC MOF again being more conductive than the DOBDC MOF (3.9×10^{-6} S/cm for Fe_2(DSBDC), and 3.2×10^{-7} S/cm for Fe_2(DOBDC)).[67] The charge mobilities of methanol-exchanged and activated Mn_2(DSBDC), as measured by FP-TRMC, were 0.02 and 0.01 $cm^2\ V^{-1}\ s^{-1}$.[67]

These results suggest that replacing $(-M-O-)_\infty$ chains with $(-M-S-)_\infty$ chains creates a more efficient pathway for intrachain charge transport. The authors attributed the dramatically higher conductivities of the Fe MOFs to the loosely bound electrons in the β-spin d band of Fe^{II} (the analogous state is empty for high-spin Mn^{II}), effectively lowering the band gap for the Fe materials compared to the Mn analogs. Although these original studies did not detect Fe^{III} by Mössbauer spectroscopy, oxidation of a small fraction of framework Fe^{II} centers to Fe^{III} may also explain these differences in conductivity.[68]

A similar effect was observed in the M_2(DOBDC)$(DMF)_2$ materials, where the conductivity of Fe_2(DOBDC)$(DMF)_2$ was significantly higher than for the other metals, at 4.8×10^{-8} S/cm.[68] Oxidation of some Fe^{II} centers to Fe^{III} because of the low reduction potential of the $Fe^{II/III}$ couple was deemed likely from electron paramagnetic resonance (EPR) spectroscopy studies, despite the handling of Fe_2(DOBDC)$(DMF)_2$ under inert conditions. For these materials, the authors attributed the higher conductivity of the Fe^{II} MOF to the relatively higher energy valence orbitals of the high-spin Fe^{II} compared to other metals, leading to a smaller band gap.

Sun et al. also investigated the effects of pore guest DMF molecules on the electrical conductivities of M_2(DOBDC)-$(DMF)_2$ and M_2(DSBDC)$(DMF)_2$ ($M = Fe^{II}$, Mn^{II}).[67] Guest-free Mn and Fe DOBDC and DSBDC frameworks each exhibited lower conductivities by about 1 order of magnitude compared to the as-synthesized materials. This difference was hypothesized to be the result of defects introduced by the solvent exchange and evacuation process. Removal of coordinated DMF in Fe_2(DSBDC) was found to further reduce[114] the conductivity by an additional 2 orders of magnitude to 1.5×10^{-9} S/cm. DFT calculations indicated that coordinated DMF accepts electron density from Fe centers, effectively hole-doping the material and increasing charge density. Studying different solvation conditions for other MOFs with coordinated solvents may reveal broader trends related to the effect of solvents on their conductivities. For example, a rhodium iodide coordination polymer showed reversible conductivity changes of up to 5 orders of magnitude on removal of water solvent.[115]

Scheurle et al. incorporated anthracene into the MOF-74 structure by reacting the 4,4′-(anthracene-9,10-diyl)bis(2-hydroxybenzoate) linker with divalent Mg, Mn, Co, Ni, and Zn.[113] The anthracene moieties are separated by the relatively long distance of 5.7 Å, thus making the charge transport through $\pi-\pi$ stacking unlikely. Despite this, all of these MOFs were several orders of magnitude more conductive (between 5×10^{-9} S/cm for Mg and 4×10^{-7} S/cm for Ni) than their DOBDC analogs. This increase in conductivity was attributed to the presence of the electron-rich anthracene core, which likely affects the charge density of the material. Also of note is the high porosity of these materials, with Brunauer–Emmett–Teller (BET) surface areas above 1100 m^2/g.

2.2. Azolate Frameworks

MOFs with pyrazolate, triazolate, and tetrazolate linkers tend to exhibit pronounced electronic coupling between the metals and the linkers by virtue of the strong σ-donating and π-accepting character of azolates.[116] In such structures, 1D chain SBUs with bridging azolates are a common motif.[117] The short bridging lengths of azolates, along with their covalent bonding to the metal, are responsible for notable cooperative electronic properties. For example, many 1D coordination polymers containing $(-Fe-N-N-)_\infty$ motifs based on triazolate and tetrazolate ligands are spin-crossover materials.[118−120] Cooperative binding events in metal–triazolate MOFs also trigger spin-state transitions[121] and reversible charge transfer events[122] at the metal centers. These electronic considerations motivated the initial studies of the transport properties of such materials.

High conductivities have been reported in Fe–azolate frameworks with $Fe^{II/III}$ mixed valency, which effectively introduces mobile charge carriers into the $(-Fe-N-N-)_\infty$ chains (Figure 9). Intervalence charge transfer (IVCT)

https://dx.doi.org/10.1021/acs.chemrev.9b00766
Chem. Rev. 2020, 120, 8536−8580

Table 1. Selected Properties for MOFs with Through-Bond Pathways for Charge Transport

material[a]	description	σ (S/cm)[b]	σ method	E_a (eV)[c]	BET SA (m^2/g)[d]	μ ($cm^2\ V^{-1}\ s^{-1}$)	ref
			DOBDC MOFs				
Co_2(DOBDC)$(DMF)_2$	desolv.	1.5×10^{-13}	2-probe pellet	0.58			68
		6×10^{-13}	vdP pellet				113
Cu_2(DOBDC)$(DMF)_2$	desolv.	1.4×10^{-14}	2-probe pellet	0.69			68
Fe_2(DOBDC)$(DMF)_2$	solv.	3.2×10^{-7}	2-probe pellet	0.42	248		67
Fe_2(DOBDC)$(DMF)_2$	desolv.	4.8×10^{-8}	2-probe pellet		241		67
Mg_2(DOBDC)$(DMF)_2$	desolv.	2.1×10^{-14}	2-probe pellet	0.64			68
		6×10^{-13}	vdP pellet				113
Mn_2(DOBDC)$(DMF)_2$	solv.	3.9×10^{-13}	2-probe pellet		287		67
Mn_2(DOBDC)$(DMF)_2$	desolv.	3.0×10^{-13}	2-probe pellet	0.55			67
		4×10^{-13}	vdP pellet				113
Ni_2(DOBDC)$(DMF)_2$	desolv.	2.8×10^{-14}	2-probe pellet	0.62			68
		6×10^{-13}	vdP pellet				113
Zn_2(DOBDC)$(DMF)_2$	desolv.	3.3×10^{-14}	2-probe pellet	0.54			68
		6×10^{-12}	vdP pellet				113
			DSBDC MOFs				
Fe_2(DSBDC)$(DMF)_2$	solv.	3.9×10^{-6}	2-probe pellet		54		67
Fe_2(DSBDC)$(DMF)_2$	desolv.	5.8×10^{-7}	2-probe pellet	0.27	83		67
Fe_2(DSBDC)	act.	1.5×10^{-9}	2-probe pellet				114
Mn_2(DSBDC)$(DMF)_2$	solv.	2.5×10^{-12}	2-probe pellet		232	0.02 (FP-TRMC)[e]	66,67
Mn_2(DSBDC)$(DMF)_2$	desolv.	1.2×10^{-12}	2-probe pellet	0.81		0.01 (FP-TRMC)	66,67
			AnBHB MOFs				
Co_2(AnBHB)		4×10^{-8}	vdP pellet		1213		113
Mg_2(AnBHB)		5×10^{-9}	vdP pellet		1137		113
Mn_2(AnBHB)		3×10^{-8}	vdP pellet		1748		113
Ni_2(AnBHB)		4×10^{-7}	vdP pellet		1352		113
Zn_2(AnBHB)		6×10^{-8}	vdP pellet		1124		113
			Fe−azolate MOFs				
Fe(1,2,3-triazolate)$_2$		7×10^{-9}	2-probe pellet (AC)		370		72
Fe(1,2,3-triazolate)$_2$$(BF_4)_{0.33}$	ox. ($Th^{\bullet+}BF_4^-$)	0.3(1)	2-probe pellet	0.0571[f]	50		72
Fe(1,2,3-triazolate)$_2$	ox. (air)	3.0×10^{-6}	2-probe pellet	0.39	443		68
		7.7×10^{-5}	4-probe pellet		450		71
Fe(1,2,3-triazolate)$_2$	ox. (I_2)	1.0×10^{-3}	4-probe pellet				71
Fe_2(BDP)$_3$		9.6×10^{-3}	4-probe sc			0.02 (FP-TRMC)	69
$K_{0.8}Fe_2$(BDP)$_3$	red. ($K^+[C_{10}H_8]^{\bullet-}$)					0.29 (FP-TRMC)	69
$K_{0.98}Fe_2$(BDP)$_3$	red. ($K^+[C_{10}H_8]^{\bullet-}$)	0.025	2-probe sc (FET)			0.84 (e, FET)	69
Fe_2(BDT)$_3$	ox. (air)	1.2(4)	2-probe sc	0.16	614		70
Fe_2Cl_2(BTDD)		1.1×10^{-7}	2-probe pellet	0.39	365		68
			other azolate MOFs				
Cd(1,2,3-triazolate)$_2$		1.4×10^{-13}	2-probe pellet	0.75			68
Co(1,2,3-triazolate)$_2$		5.1×10^{-14}	2-probe pellet	0.64			68
Cu(1,2,3-triazolate)$_2$		3.2×10^{-14}	2-probe pellet	0.59			68
Mg(1,2,3-triazolate)$_2$		9.9×10^{-15}	2-probe pellet	0.74			68
Mn(1,2,3-triazolate)$_2$		8.2×10^{-14}	2-probe pellet	0.59			68
Zn(1,2,3-triazolate)$_2$		1.2×10^{-14}	2-probe pellet	0.77			68
Co_2Cl_2(BTDD)		3.7×10^{-13}	2-probe pellet	0.86			68
Mn_2Cl_2(BTDD)		1.3×10^{-14}	2-probe pellet	0.89			68
Ni_2Cl_2(BTDD)		2.8×10^{-13}	2-probe pellet	0.84			68
			other through-bond pathways				
[Cu_2(Hmna)(mn)][NH_4]		10.96	4-probe sc	0.006			129

[a]See Abbreviations. [b]Measured at room temperature (exact temperature unspecified) or 296 K. [c]Derived from Arrhenius model unless otherwise indicated. For materials exhibiting more than one distinct activation regions, E_a at 300 K is given. [d]Calculated from N_2 adsorption isotherms. [e]Measured for methanol-exchanged Mn_2(DSBDC). [f]Derived from polaronic nearest-neighbor hopping.

processes in these MOFs are expected to resemble those in molecular mixed-valence complexes of d^5−d^6 metal centers with π-acid bridging linkers.[123] The accessibility of metal-centered mixed valency likely results from the low reduction potential of Fe^{III} coupled with small reorganization energies of the coordination spheres, which in turn lead to faster electron transfer rates compared to other transition metals.[59] In other words, both thermodynamic and kinetic factors can be expected to play a role in enabling facile charge transport.

In their report of the M^{II}(1,2,3-triazolate)$_2$ series of isostructural MOFs (M = Mg, Fe, Co, Cu, Zn, and Cd),[124] Gándara et al. indicated that the Fe(1,2,3-triazolate)$_2$ material

https://dx.doi.org/10.1021/acs.chemrev.9b00766
Chem. Rev. 2020, 120, 8536−8580

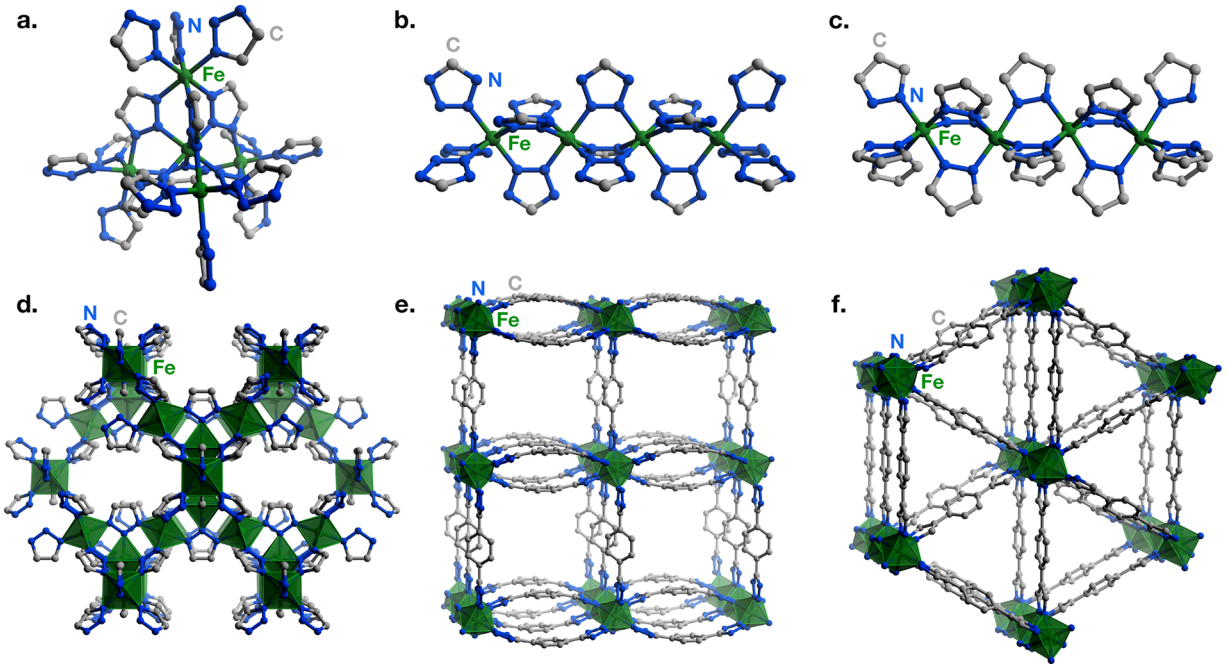

Figure 9. Structures of Fe−azolate MOFs. (a−c) SBUs of Fe(1,2,3-triazolate)$_2$,[72] $Fe_2(BDT)_3$,[125] and $Fe_2(BDP)_3$,[270] respectively, showing continuous $(-Fe-N-N-)_\infty$ chains. (d) Connectivity of Fe(1,2,3-triazolate)$_2$, showing continuous 3D diamondoid network of Fe−N bonds. (e and f) Connectivities of $Fe_2(BDT)_3$ and $Fe_2(BDP)_3$, respectively, showing 1D channels.

was conductive (7.7×10^{-5} S/cm) in its as-synthesized form.[71] In this structure, each triazolate linker bridges three octahedrally coordinated Fe^{II} centers, forming a 3D network with diamond topology containing $(-Fe-N-N-)_\infty$ chains (Figure 9a,d). The material is permanently porous, with a BET surface area of 450 m^2/g. Sun et al. later reported that the Mg, Mn, Co, Cu, Zn, and Cd MOFs with 1,2,3-triazolate are insulating (conductivities $<2 \times 10^{-13}$ S/cm) and measured a conductivity value of 3.0×10^{-6} S/cm for Fe(1,2,3-triazolate)$_2$, similar to the original study.[68]

In these reports, Fe(1,2,3-triazolate)$_2$ was handled in ambient atmosphere because no changes in powder X-ray diffraction (PXRD) patterns were observed after several weeks of air exposure (suggesting stability to these conditions). However, several pieces of evidence suggested that oxidation of the Fe^{II} centers is accessible and contributes to the conductivity. Gándara et al. found that the conductivity increased to 1.0×10^{-3} S/cm after exposure to I_2 vapor with retention of the structure. They surmised that some Fe^{II} sites were oxidized to Fe^{III}, enabling IVCT. Sun et al. showed that the room temperature EPR spectrum contained signals at $g \approx 2.0$ and 4.2, consistent with the presence of high-spin Fe^{III} centers. DFT electronic band structure calculations of Fe(1,2,3-triazolate)$_2$ with Fe^{III} defects revealed unoccupied Fe^{III} midgap states that could facilitate the formation of mobile valence band holes. Moreover, the calculated spin density distribution also indicated partial delocalization of unpaired electrons among Fe sites.

Definitive evidence of the importance of mixed valency on the conductivity of Fe(1,2,3-triazolate)$_2$ was shown by Park et al. via the systematic postsynthetic introduction of Fe^{III} sites.[72] By handling all reagents under rigorously air-free conditions, they obtained the Fe(1,2,3-triazolate)$_2$ material with a pink color, in contrast to the orange or brown powders reported previously. The material contained only low-spin Fe^{II} by Mössbauer spectroscopy, and its electrical conductivity was only $<7 \times 10^{-9}$ S/cm, about 3 orders of magnitude lower than previous reports.

Upon oxidation with stoichiometric amounts of thianthrene tetrafluoroborate, materials with the formula Fe(1,2,3-triazolate)$_2(BF_4)_x$ were obtained, in which BF_4^- counteranions charge-balance the Fe^{III} centers introduced into the framework. Critically, increasing the BF_4^- content (and hence the Fe^{III} concentration) increased the conductivities, which in the study was explained by a polaronic hopping model. The maximum achieved BF_4^- loading of $x = 0.33$ corresponds to one anion per pore; accordingly, Fe(1,2,3-triazolate)$_2(BF_4)_{0.33}$ showed a very low BET surface area of 50 m^2/g. The conductivity of Fe(1,2,3-triazolate)$_2(BF_4)_{0.33}$, 0.3(1) S/cm, is among the highest reported for 3D frameworks, and represents an increase of nearly 8 orders of magnitude over the starting material. In addition, detailed Mössbauer spectroscopy measurements revealed that charges were delocalized between Fe^{II} and Fe^{III} on the measurement time scale ($\sim 10^{-8}$ s) at 290 K.

Correlation between introduction of $Fe^{II/III}$ mixed valency into $(-Fe-N-N-)_\infty$ chains and increased conductivity was also demonstrated for an Fe^{II} framework with benzene-1,4-ditetrazolate (BDT).[70] This material, $Fe_2(BDT)_3$ (Figure 9b,e), was initially reported as an all-Fe^{II} compound with mixed spin states and a black color.[125] Xie et al. found that crystals synthesized under anaerobic conditions were orange-red in color, gradually darkening to black after several days in ambient atmosphere with no changes in the PXRD patterns. The air-exposed material remained porous, with a BET surface area of 614 m^2/g. The single-crystal conductivities measured along the direction of the $(-Fe-N-N-)_\infty$ direction increased from $6(2) \times 10^{-5}$ S/cm for the as-synthesized material to 1.8 S/cm after 30 days in air. UV−vis−NIR spectroscopy and DFT band structure calculations further confirmed IVCT between Fe^{II} and Fe^{III} centers as the likely mode of charge transport in this material. The method of oxidation and results

https://dx.doi.org/10.1021/acs.chemrev.9b00766
Chem. Rev. 2020, 120, 8536−8580

observed in this work are similar to a study of a porous vanadyl analog of Prussian blue.[126]

The Fe^{II} framework with bis[1,2,3-triazolo[4,5-*b*],[4′,5′-*i*]]dibenzo[1,4]dioxin (BTDD), $Fe_2Cl_2(BTDD)$, also contains $(-Fe-N-N-)_\infty$ chains as part of the rod SBUs in a hexagonal structure similar to MOF-74. Sun et al. reported the conductivity of this material to be 1.1×10^{-7} S/cm,[68] almost 6 orders of magnitude higher than the Mn^{II}, Co^{II}, and Ni^{II} isostructural materials.[127] Unintentional doping with Fe^{III} was again invoked to explain the higher conductivity.

Achieving $Fe^{II/III}$ mixed valency with an all-Fe^{III} starting material was demonstrated by Aubrey et al. with the framework $Fe_2(BDP)_3$ (BDP = benzene-1,4-dipyrazolate) (Figure 9c,f).[69] Reduction of $Fe_2(BDP)_3$ with potassium naphthalenide afforded materials with the formula $K_xFe_2(BDP)_3$ ($0 < x \leq 2.0$). Single crystals were incorporated into FET devices by depositing platinum/carbon contacts between the MOF and prepatterned electrodes. The highest conductivity measured for one such device was 0.025 S/cm for $K_{0.98}Fe_2(BDP)_3$ (corresponding to about half of the Fe^{III} centers reduced to Fe^{II}). The electron mobility from the same device was 0.84 $cm^2\ V^{-1}\ s^{-1}$. In comparison, a device of the original $Fe_2(BDP)_3$ material exhibited a conductivity of 3.5×10^{-7} S/cm and electron mobility of 2×10^{-3} $cm^2\ V^{-1}\ s^{-1}$. The authors suspected that the true intrinsic conductivity of the material was underestimated because of contact resistance in the two-probe configuration. Indeed, a four-probe device of $Fe_2(BDP)_3$ showed a significantly higher conductivity of 9.6×10^{-3} S/cm, suggesting that the values for the reduced material may also be underestimated to some extent.

In many of the cases presented above, electronic structure calculations have shown significant band dispersion, confirming the strong coupling between Fe d orbitals and azolate π-orbitals.[68−70] This feature, however, appears to not be unique to iron-based materials. Indeed, the calculated band structures of M(1,2,3-triazolate)$_2$ frameworks with other metals suggest that they may also exhibit mobile charge transport pathways and relatively small band gaps.[68] If free carriers can be introduced into MOFs with related structural motifs, they will likely comprise additional platforms for conductivity. We note also that triazolate and pyrazolate frameworks generally exhibit high chemical stability because of the strong donating ability of these ligands, and therefore may be of interest for applications in which stability and conductivity are both important.[128]

Pathak et al. attempted[129] to extend the through-bond approach to two dimensions by incorporating extended 2D Cu−S sheets in $[Cu_2(Hmna)(mna)][NH_4]$ (Hmna = 6-mercaptonicotinic acid). Although this framework is completely nonporous and cannot be strictly called a MOF, it showed some of the highest conductivities reported to date for coordination polymer single crystals, up to ∼11 S/cm. The material behaved as a semiconductor with a low E_a of ∼6 meV, noticeably lower than the calculated bandgap (1.2 eV) or observed optical bandgap (1.34 eV).

3. EXTENDED CONJUGATION

The discovery of free-standing graphene[130] in 2004 precipitated an avalanche of interest in the electronic properties of 2D materials.[131−136] In addition to the "top-down" methods commonly used for the preparation of these nanoscale compounds, the possibility of creating synthetic 2D materials via "bottom-up" approaches has also been explored.[134−138] Conductive 2D MOFs made via solvothermal self-assembly have emerged as 2D materials with promising transport properties. Calculated band structures suggest that they may host exotic electronic properties, including topologically protected surface states.[31,32,34−36] Members of this class exhibit the highest conductivities for porous, crystalline framework materials.

The MOFs in this section feature linkers based on conjugated organic cores and redox-noninnocent chelating groups such as ortho-diols (catechols), -diamines, and -dithiols (Figure 10). The oxidation states for a catechol fragment,

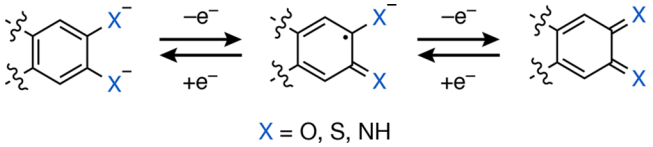

Figure 10. Redox series of 2−, 1−, and 0 charge states for a deprotonated catecholoid fragment, a common motif in conductive MOFs with extended conjugation.

hydroquinone, semiquinone, and quinone, can also be accessed in the nitrogen- and sulfur-containing analogs. In most cases, the ligands are partially oxidized during synthesis, which favors deprotonation and subsequent framework formation. The resulting MOFs contain mixed-valent linkers—potentially leading to high carrier densities—with some examples of charge states that can be tuned postsynthetically. Although 2D frameworks have received the most attention and constitute the vast majority of examples, we also discuss several frameworks with 3D structures showing extended metal−linker conjugation and high conductivities.

The metal−organic linkages in these MOFs are analogous to motifs known to promote charge delocalization in inorganic complexes. For example, the redox-noninnocent ligands in metal−dithiolene complexes facilitate electron delocalization between the metal and linker.[139,140] Such compounds are components in many molecular conductors (and even superconductors).[141] Ligand radical character in the bis(*o*-diiminobenzosemiquinonate) Ni^{II} complex is known to be stabilized by the metal binding.[142−144] Dihydroxybenzoquinone-type linkers also demonstrate strong electronic and magnetic coupling in transition metal complexes, especially in their oxidized radical forms.[145−147]

We note that the structures of these materials are considered to be 2D in the sense that covalent bonds extend only within the *ab* plane. However, to date, mono- or few-layer samples of 2D MOFs displaying extended conjugation have not been studied in detail. Moreover, only one study on single crystals contacted along the conjugation direction has been reported.[79] Hence, interlayer effects are expected to influence the reported bulk properties. Molecular metal−dithiolene and diiminobenzosemiquinonate complexes exhibit semiconducting or metallic behavior with the highest conductivities along the stacking direction,[141,143] suggesting that transport facilitated by non-covalent *c* direction interactions may also contribute to the conductivities measured in powder samples of 2D MOFs. This intuition is supported by existing cross-plane conductivity measurements[79,148] and transport studies of related MOFs with no π−d conjugation.[92]

3.1. Frameworks with Ditopic Redox Noninnocent Linkers

A number of materials built with tetraoxolene ligands, such as dihydroxybenzoquinonate (dhbq) and chloranilate (Cl_2dhbq),

https://dx.doi.org/10.1021/acs.chemrev.9b00766
Chem. Rev. 2020, 120, 8536−8580

Table 2. Selected Properties for MOFs with dhbq and Related Ligands

material[a]	description	σ (S/cm)[b]	σ method[c]	E_a (eV)[d]	BET SA (m^2/g)[e]	ref
$[Cr_2(dbhq)_3][(H_2NMe_2)_{1.5}]$		$1.2(1) \times 10^{-4}$	2-probe pellet	0.44	collapse	152
$[Fe_2(dhbq)_3][(Bu_4N)_2]$ (3D)		0.16(1)	2-probe pellet		dense	153
$[Fe_2(dhbq)_3][Na_{0.9}(Bu_4N)_{1.8}]$ (3D)	red. ($Na^+[C_{10}H_8]^{\bullet-}$)	$6.2(1) \times 10^{-3}$	2-probe pellet		dense	153
$[Fe_2(Cl_2dhbq)_3][(Me_2NH_2)_2]$	solv.	0.014	2-probe pellet			149
$[Fe_2(Cl_2dhbq)_3][(Me_2NH_2)_2]$	act.	$1.0(3) \times 10^{-3}$	2-probe pellet		1175	149
$[Fe_2(Cl_2dhbq)_3][(Cp_2Co)_{1.43}(Me_2NH_2)_{1.57}]$	red. (Cp_2Co)	$5.1(3) \times 10^{-4}$	2-probe pellet			149
$[Fe_2(Cl_2dhbq)_3][(H_3O)(phz)_3]$		0.031(8)	2-probe sc (‖)			151
		$1.0(9) \times 10^{-4}$	2-probe sc (⊥)			151
		4×10^{-5}	2-probe pellet	0.16		156
$[Fe_2(Br_2dhbq)_3][(H_3O)(phz)_3]$		$3(1) \times 10^{-3}$	2-probe sc (‖)			151
		$6(2) \times 10^{-6}$	2-probe sc (⊥)			151
$[Mn_2(Cl_2dhbq)_3][(Me_4N)_2]$		$1.14(3) \times 10^{-13}$	2-probe pellet	0.74		150
$[Mn_2(Cl_2dhbq)_3][Na_3(Me_4N)_2]$	red. ($Na^+[C_{10}H_8]^{\bullet-}$ and $[C_{12}H_{10}]^{\bullet-}$)	$2.27(1) \times 10^{-8}$	2-probe pellet	0.489		150
$[Mn_2(Cl_2dhbq)_3][Na(Me_4N)]$	ox.	$1.45(2) \times 10^{-13}$	2-probe pellet			150
$[Ti_2(Cl_2dhbq)_3][(H_2NMe_2)_2]$		$2.7(2) \times 10^{-3}$	2-probe pellet	0.27[f]	collapse	152
$[V_2(Cl_2dhbq)_3][(H_2NMe_2)_2]$		0.45(3)	2-probe pellet	0.064[g]	collapse	152
$[Zn_2(Cl_2dhbq)_3][(H_2NMe_2)_2]$		$1.5(3) \times 10^{-9}$	2-probe pellet			149
$CrCl_2(pyz)_2$		3.2×10^{-2}	2-probe pellet			157

[a]See Abbreviations. [b]Measured at room temperature (exact temperature unspecified) or between 295 and 300 K under N_2 or Ar atmosphere. [c]‖ denotes device contacted in-plane/parallel to 2D layers; ⊥ denotes device contacted cross-plane/perpendicular to 2D layers. [d]Derived from Arrhenius model unless otherwise indicated. For materials exhibiting more than one distinct activation regions, E_a at 300 K is given. [e]Calculated from N_2 adsorption isotherms. [f]Derived from polaronic nearest-neighbor hopping. [g]Derived from Efros-Shklovskii variable-range hopping.

show high electrical conductivity concurrent with intrinsic porosity (Table 2). Although this class of materials is quite expansive,[145] charge transport studies have focused on a family of layered honeycomb anionic frameworks, $[M_3(X_2dhbq)_2]^{n-}$ (X = H, Cl, Br)[149−152] and structurally related 3D phases,[153,154] discussed in detail below.

The easily accessible redox couples of these ligands and their resulting ability to form stable radicals form the origin of strong magnetic coupling in a number of magnetic molecular complexes.[145−147] The incorporation of these ligands into MOFs harnessed these features to produce materials with permanent porosity, high electrical conductivity, and magnetic ordering. Notably, the $Fe^{II/III}$-based materials display some of the highest conductivities and magnetic ordering temperatures in MOFs.

The mechanism of conductivity in these materials is up for debate: while most works propose hopping between either redox-active metal sites or radical organic linkers to be responsible for charge transport, many of these MOFs display high degrees of electron delocalization between the linker and the metal. As a result, they show similarities to the materials in the following section, which exhibit extended conjugation between the metal and ligand.

3.1.1. Two-Dimensional Layered Frameworks with Ditopic Linkers. This structure type, which was initially reported for Mn^{II} and Cd^{II} chloranilates,[155] consists of hexagonal layered structures with solvent-accessible pores of ∼1.5 nm in diameter. The metal atoms are each octahedrally coordinated by three ligands (Figure 11). The frameworks are all anionic, with charge-balancing cations located either within the pore or between the layers. For simplicity, most of the following observations will discuss only the anionic framework.

The Harris group reported[149] early studies of electrical conductivity in chloranilate frameworks, focusing initially on the Fe^{III} and Zn^{II} materials. The materials were produced through the reaction of the corresponding divalent metal salt and chloranilic acid and are charge-balanced by dimethylammonium ions that reside in the pores of the framework. The low barrier to oxidation of Fe^{II} results in electron transfer from the Fe^{II} ions to the ligands, converting two-thirds of these to the 3− radical state ($Cl_2dhbq^{3-\bullet}$), and leaving the remaining third in the closed-shell Cl_2dhbq^{2-} state (Figure 12). This ligand-based mixed valency resulted in the high conductivity of $1.4(7) \times 10^{-2}$ S/cm. When desolvated, the conductivity decreased to $1.0(3) \times 10^{-3}$ S/cm, attributed to slight framework distortions. Chemical reduction of the MOF by excess Cp_2Co led to full conversion of the ligands to the $Cl_2dhbq^{3-\bullet}$ radical state, which caused a further decrease in conductivity to $5.1(3) \times 10^{-4}$ S/cm. The lower conductivity upon the loss of mixed valency is consistent with charge

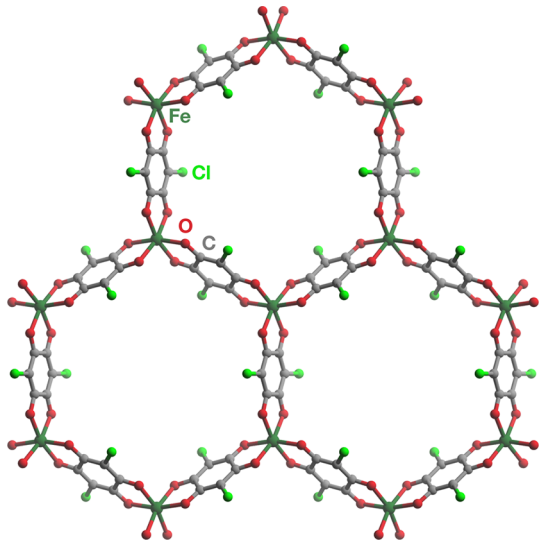

Figure 11. Structure of $[Fe_2(Cl_2dhbq)_3]^{2-}$, showing a honeycomb arrangement of $Fe^{II/III}$ and Cl_2dbhq^{2-} within a single 2D layer (charge-balancing $[Me_2NH]^+$ cations occupying pore volume not shown).[149]

https://dx.doi.org/10.1021/acs.chemrev.9b00766
Chem. Rev. 2020, 120, 8536−8580

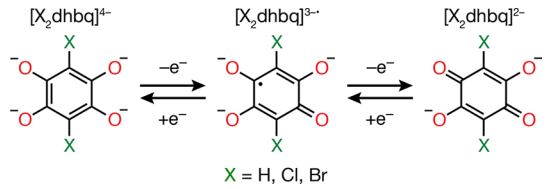

Figure 12. Redox series of 4−, 3−, and 2− charge states for linkers based on dihydroxybenzoquinone (dhbq).

transport facilitated by electron transfer between $Cl_2dhbq^{3-\bullet}$ and Cl_2dhbq^{2-} in the as-synthesized material. The temperature dependence of conductivity for the different states of $[Fe_2(Cl_2dhbq)_3]^{n-}$ showed similar semiconductor-type behavior with Arrhenius activation energies of ∼0.3 eV.

The presence of strong coupling between metal centers via radical bridging ligands was further corroborated by the magnetic behavior of $[Fe_2(Cl_2dhbq)_3]^{2-}$. Solvated $[Fe_2(Cl_2dhbq)_3]^{2-}$ ordered ferromagnetically at 80 K, whereas the desolvated (and less conductive) material ordered at 22 K, suggesting weaker coupling. The reduced material ordered at a higher temperature of 105 K, as would be expected for more Fe^{III} ions being bridged by radical-containing ligands in the reduced material.

In the Zn−chloranilate framework, the oxidation of Zn^{II} by Cl_2dhbq^{2-} is not thermodynamically accessible, resulting in the full ligand population of $[Zn_2(Cl_2dhbq)_3]^{2-}$ remaining in the closed-shell Cl_2dhbq^{2-} states. Accordingly, the conductivity of this material was relatively low ($1.5(3) \times 10^{-9}$ S/cm). The authors proposed that the closed-shell configuration of Zn^{II} with filled d orbitals introduces a barrier to charge transport between the ligands, leading to lower conductivity. The relative influence of the d shell filling vs the ligand oxidation states could be probed via reduction of the zinc material to a similar mixed-valence state as in the Fe analog.

An isostructural Mn^{II}-based system, $[Mn_2(Cl_2dhbq)_3]^{2-}$, showed an increase in conductivity upon reduction.[150] The conductivity value rose from $1.14(3) \times 10^{-13}$ S/cm for the fully oxidized version with Cl_2dhbq^{2-} diamagnetic linkers, to $2.27(1) \times 10^{-8}$ S/cm for the reduced version, $[Mn_2(Cl_2dhbq)_3]^{5-}$, containing $Cl_2dhbq^{3-\bullet}$ radical linkers. To explain the difference in conductivities between the Mn^{II} and Fe^{II} materials, the authors proposed a poorer energetic match between the Mn atoms and the linker compared to Fe. This mismatch may have also led to noticeably higher activation energies of 0.489(8) eV for the reduced and 0.74(3) eV for the oxidized Mn frameworks. The change in conductivity was fully reversible upon chemical oxidation to the initial state $[Mn_2(Cl_2dhbq)_3]^{2-}$. Notably, like the Fe^{III}-based framework, $[Mn_2(Cl_2dhbq)_3]^{5-}$ displayed a ferromagnetic transition, albeit with a lower T_c of 41 K.

The charge transport behavior of chloranilate frameworks with the same overall honeycomb structure and mixed-valent $Fe^{II/III}$ was also studied. The first report, by Shilov et al.,[156] discussed the structure and electronic properties of $[Fe^{II}Fe^{III}(Cl_2dhbq^{2-})_2(Cl_2dhbq^{3-\bullet})]^{2-}$. Unlike the aforementioned $[Fe^{III}_2(Cl_2dhbq)_3]^{2-}$ system, in which the charge balancing $(Me_2NH)^+$ ions are located mainly inside the pores, the framework charge in the mixed-valent $Fe^{II/III}$ framework is balanced by hydrogen-bonded layers of $[(H_3O)_2(phenazine)]^{2+}$. Shilov et al. were unable to isolate single crystals of this material, and conducted a thorough investigation of its electronic properties on polycrystalline powder samples. Mössbauer spectroscopy combined with magnetometry revealed the mixed-valent nature of the material, with the Fe atoms present both in pure 2+ and 3+ states, as well as in the mixed-charge 2.5+ state, with relative concentrations dependent on the temperature. The material showed a relatively high conductivity of 4×10^{-5} S/cm (polycrystalline pellet) and an Arrhenius E_a of 0.16 eV.

A later study reported single-crystal measurements on a material with the same nominal formula, $[Fe^{II}Fe^{III}(Cl_2dhbq^{2-})_3]^-$, assigned to different charge states (with all the ligands in their closed-shell Cl_2dhbq^{2-} configurations, and no organic radicals).[151] Despite the lack of organic radicals, the MOF showed a high conductivity of 0.031(8) S/cm from single-crystal measurements parallel to the layers, and $1.0(9) \times 10^{-4}$ S/cm orthogonal to the layers. Similar conductivities, $3(1) \times 10^{-3}$ S/cm (parallel) and $6(2) \times 10^{-6}$ S/cm (orthogonal), were obtained for the isostructural framework containing bromanilate instead of chloranilate. The high anisotropy of the conductivity confirmed that charge transport is mainly limited within the *ab* plane. Though these values were from single-crystal measurements (vs powder pellet values for $[Fe^{III}_2(Cl_2dhbq)_3]^{2-}$), it is remarkable that the conductivities were of the same magnitude. This result demonstrates that ligand mixed valency and metal mixed valency can both enable charge transport in these systems, consistent with strong electronic coupling between metals and ligands.

A series of structurally related frameworks based on early first row transition metals, $[V_2(Cl_2dhbq)_3]^{2-}$, $[Ti_2(Cl_2dhbq)_3]^{2-}$, and $[Cr_2(dhbq)_3]^{1.5-}$ showed similarly high conductivities.[152] Precursors containing the highly reducing divalent early 3d transition metal ions Ti^{II}, V^{II}, and Cr^{II} were combined with Cl_2dhbq^{2-} and $dhbq^{2-}$, reducing the linkers to the corresponding radical anions. The more diffuse orbitals of the early transition metals (as compared to the later Ni, Co, or Cu) were hypothesized to allow for orbital overlap with the ligand and thus more efficient charge delocalization. This approach proved successful, producing materials with conductivities of $2.7(2) \times 10^{-3}$ S/cm for $[Ti_2(Cl_2dhbq)_3]^{2-}$, 0.45(3) S/cm for $[V_2(Cl_2dhbq)_3]^{2-}$, and $1.2(1) \times 10^{-4}$ S/cm for $[Cr_2(dhbq)_3]^{1.5-}$. The observed conductivities followed the same trend as the degree of electronic delocalization observed by optical spectroscopy, where the Ti and Cr-based materials can be classified as Robin−Day class II and the V-based material as class III, indicating much stronger charge delocalization in the latter.

The charge states of both the ligands and the metals in these three materials differed. From elemental analysis, optical spectroscopy, and magnetization measurements, the three materials had the following assignments: $[Ti^{IV}_2(Cl_2dhbq^{3-})_2(Cl_2dhbq^{4-})]^{2-}$, $[V^{III}_2(Cl_2dhbq^{2-})(Cl_2dhbq^{3-})_2]^{2-}$ (assigned putatively, as electronic delocalization did not allow full resolution of the metal/ligand charge states), and $[Cr^{III}_2(dhbq^{2-})_{1.5}(dhbq^{3-})_{1.5}]^{1.5-}$. The stronger charge delocalization and significantly higher conductivity in the V-based materials are explained by a better energy match between the ligand orbitals and the metal 3*d* shell. Interestingly, $[Ti_2(Cl_2dhbq)_3]^{2-}$ displayed strong antiferromagnetic coupling between the organic radical spins, with a Curie−Weiss temperature of −223 K, although no ordering was observed in it or the other two materials. Variable temperature conductivity measurements revealed semiconducting behavior fitting well with either polaronic nearest-neighbor

https://dx.doi.org/10.1021/acs.chemrev.9b00766
Chem. Rev. 2020, 120, 8536−8580

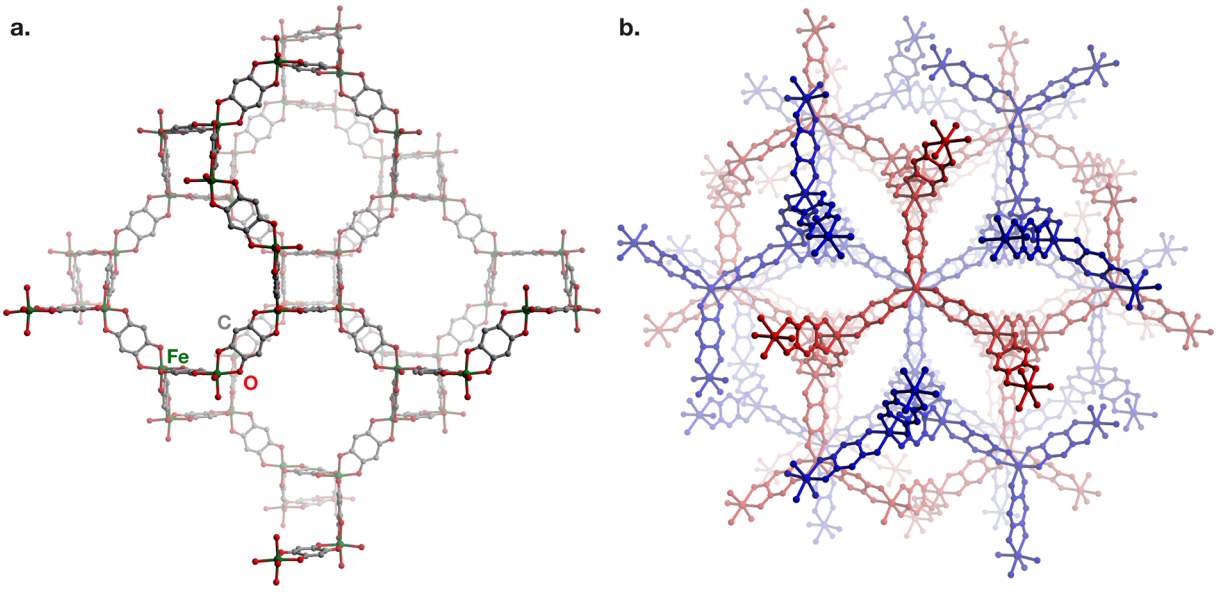

Figure 13. Structure of $[Fe_2(dhbq)_3]^{2-}$, showing (a) a single sublattice illustrating local coordination environments of Fe^{III} and $dhbq^{2-/3-\bullet}$, and (b) two interpenetrated nets (charge-balancing Bu_4N^+ cations not shown).[153]

hopping (Ti- and Cr-based materials) or the Efros−Shklovskii variable range hopping (VRH) model (V-based material). These mechanisms differed from the Fe-based materials, perhaps as a result of the wider temperature range fitted (a narrower region may yield an Arrhenius-type dependence).

A similar approach was later applied[157] to dense pyrazine-based square lattice coordination polymers, in which the reaction of a Cr^{II} salt with pyrazine led to the formation of a highly conductive nonporous framework. As in the dhbq materials, the conductivity originated from the reduction of pyrazine to its radical anion form, which led to improved ligand π-system−metal d-orbital overlap, as well as introduction of mobile charge carriers. The material, $CrCl_2(pyz)_2$ (pyz = pyrazine), showed a relatively high conductivity of 3.2×10^{-2} S/cm for a pressed pellet, along with a semiconductor-type temperature dependence, which could be fitted to the Mott law for two dimensions.

3.1.2. Three-Dimensional Frameworks Based on dhbq. Dihydroxybenzoquinone also forms 3D frameworks with many late transition[158] and rare-earth metals.[159] The charge transport properties of the Fe material have been evaluated in detail.[153] $[Fe_2(dhbq)_3]^{2-}$ is a cubic interpenetrated 3D framework with octahedral Fe^{III} sites containing radical $dhbq^{3-\bullet}$ anions, with the as-synthesized formula $[Fe^{III}_2(dhbq^{3-\bullet})_2(dhbq^{2-})]^{2-}$ (Figure 13a). The two component sublattices are enantiomeric and fully independent from each other (Figure 13b). Due to the bulky tetrabutylammonium ions compensating the charge, the material is essentially nonporous (though a high theoretical surface area of 5070 m^2/g was calculated for the fully oxidized material with charge-balancing cations removed from the pores). The as-synthesized material showed an impressive electrical conductivity of 0.16(1) S/cm from a 2-probe pellet measurement. This is one of the highest values reported to date for a 3D material with likely isotropic charge transport. The authors proposed that the high conductivity arises from charge hopping between $dhbq^{3-\bullet}$ and $dhbq^{2-}$ centers. This agrees with the lower conductivity ($6.2(1) \times 10^{-3}$ S/cm) observed upon reduction of the material by an average of 0.7 e^- per ligand to $[Fe^{III}_2(dhbq)_3]^{2.7-}$, which effectively lessened the extent of ligand-based mixed valency and hence the concentration of available charge hopping sites. Interestingly, both the as made and the reduced materials displayed a very low-energy absorption edge suggestive of Robin−Day type-II/III mixed valency originating from the $dhbq^{2-/3-\bullet}$ couple. This assignment implies that the charges are significantly delocalized and that description of the charge transport from a band-like perspective may be appropriate.

A Tb^{III}-based chloranilate MOF with a three-dimensional structure has been reported to have an electrical conductivity of 6.25×10^{-4} S/cm.[154] This lower value compared to transition metal chloranilate MOFs is likely due to the strongly ionic bonding character between the ligand and the lanthanide.

3.2. Frameworks with Flat, Multitopic, Conjugated Linkers

Layered two-dimensional frameworks based on flat, fully conjugated ligands with trigonal geometries constitute one of the most prominent classes of conductive MOFs (see Tables 3−5). To the best of our knowledge, these materials show the highest conductivities observed for ordered microporous materials. The clear and consistent strategy underlying these high conductivities, which are usually thought to originate from the strong electron delocalization within the 2D layers, also contributes to the broad appeal of these materials. The high conductivity values and straightforward design principles drive the growing number of studies on these materials.

The strong delocalization is produced by covalent bonding between the metal and the linker to form an extended π-conjugated framework (Figure 14). Three key features of the ligands enable this electronic structure. First of all, the catecholoid linkers are highly susceptible to oxidation, producing organic radicals in the MOF. Second, full conjugation within the linker, which consists of one large π-system, facilitates the delocalization and stabilization of said radicals. Finally, good energy matching between the linker and the metal frontier orbitals allows the conjugated system to extend throughout the full layer. The overall geometry of the material is also important for the extended conjugation of the π-systems, as coplanar linkers form flat 2D layers.

https://dx.doi.org/10.1021/acs.chemrev.9b00766
Chem. Rev. 2020, 120, 8536−8580

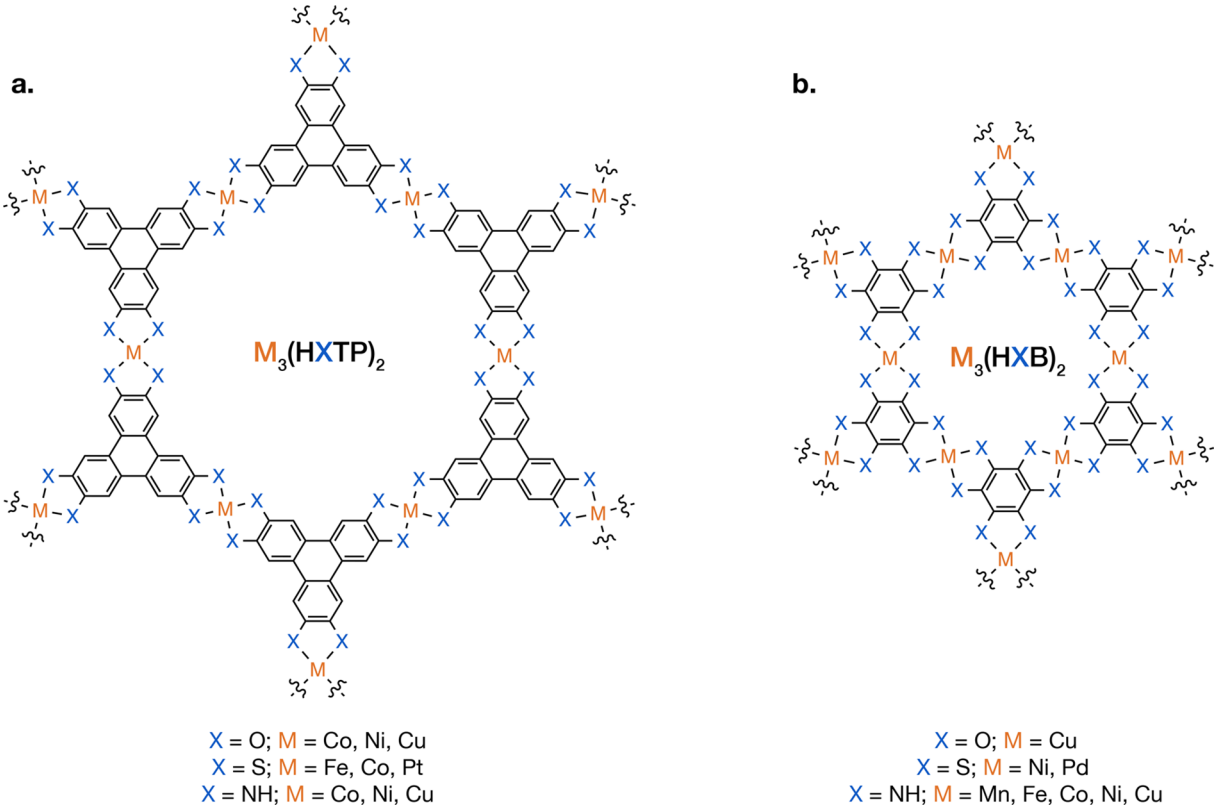

Figure 14. Representations of the structures of 2D honeycomb sheets in porous MOFs exhibiting extended conjugation with (a) triphenylene-based linkers and (b) benzene-based linkers, both with various functional groups (X) and framework metals (M).

Materials in this class can be divided into three broad categories, based on the linker used: semiquinoid-based materials with oxygen-based linkers, iminosemiquinoid-based materials with nitrogen-based linkers, and dithiolene-based materials with sulfur-based linkers. With the exception of several recent reports, each category consists of two families: one with larger hexa-substituted triphenylene linkers, and one with smaller hexa-substituted benzene linkers, with the former being more porous, and the latter typically being dense. Overall, increasing the bond strength between the metal and the ligand (i.e., moving from oxygen-based to nitrogen- to sulfur-based linkers) and increasing the framework density (moving from a triphenylene core to a benzene core) both appear to result in higher conductivities.

Although some trends are emerging, the limited number of materials in this class still precludes more detailed correlations among composition, structure, and properties. Although many metal−ligand pairs have been reported, comparative studies designed to isolate compositional variables (i.e., the ligand core, functional group, and metal) are necessary to disentangle their influence on conductivities. Small crystallite size or low crystallinity in many of these materials introduce uncertainties regarding the exact structures, especially related to the layer stacking arrangements. The exact oxidation and protonation states of redox noninnocent linkers are often ambiguous as well. Significant variance is also observed between different reports of the same material by different groups with respect to conductivity, crystallinity, and purity. Therefore, a more systematic approach to these materials, including standardization of synthetic and measurement techniques, will be central to the elucidation of underlying trends.

Despite these challenges for accurate, consistent structural and compositional characterization of 2D conductive MOFs, their high conductivities have attracted significant interest from applied studies in electrocatalysis,[16−20] chemiresistive sensing,[21−25] and energy storage technologies.[27−30] An excellent overview of potential applications of these materials is provided in ref 47.

3.2.1. Semiquinoid Linker-Based Materials. *3.2.1.1. Hexahydroxytriphenylene MOFs.* In 2012, the Yaghi group reported the first materials of this family with Co^{II}, Ni^{II}, and Cu^{II}, which crystallize in two different structures.[148] On the basis of synchrotron PXRD and transmission electron microscopy (TEM), they found that Cu^{II} and 2,3,6,7,10,11-hexahydroxytriphenylene (H_6HOTP) form a layered honeycomb framework with each metal coordinated by two linkers in a square planar environment, resulting in an overall formula of $Cu_3(HOTP)_2$. Co^{II} and Ni^{II} produced MOFs with similar honeycomb layers, but with the metal sites in octahedral environments with two terminal aqua ligands. Additionally, the framework layers in the Co and Ni MOFs are interleaved with layers of molecular $[(H_2O)_4M]_3HOTP$ clusters, which contribute to an overall formula $M_9(HOTP)_4$ (discounting solvent molecules) (Figure 15). Both the Cu and the Co/Ni structure types have a near-eclipsed arrangement of the layers, resulting in permanent microporosity, with surface areas in the range of 400−500 m^2/g.

As implied by their distinct formulas, these two structure types also contain different ligand charge states (HOTP is assumed to be fully deprotonated in both cases). In $Cu_3(HOTP)_2$, all linkers are $HOTP^{3-}$, (i.e., oxidized by 3 electrons). In $Co_9(HOTP)_4$ and $Ni_9(HOTP)_4$, the average charge state is $HOTP^{4.5-}$. Hmadeh et al. proposed that the

https://dx.doi.org/10.1021/acs.chemrev.9b00766
Chem. Rev. 2020, 120, 8536−8580

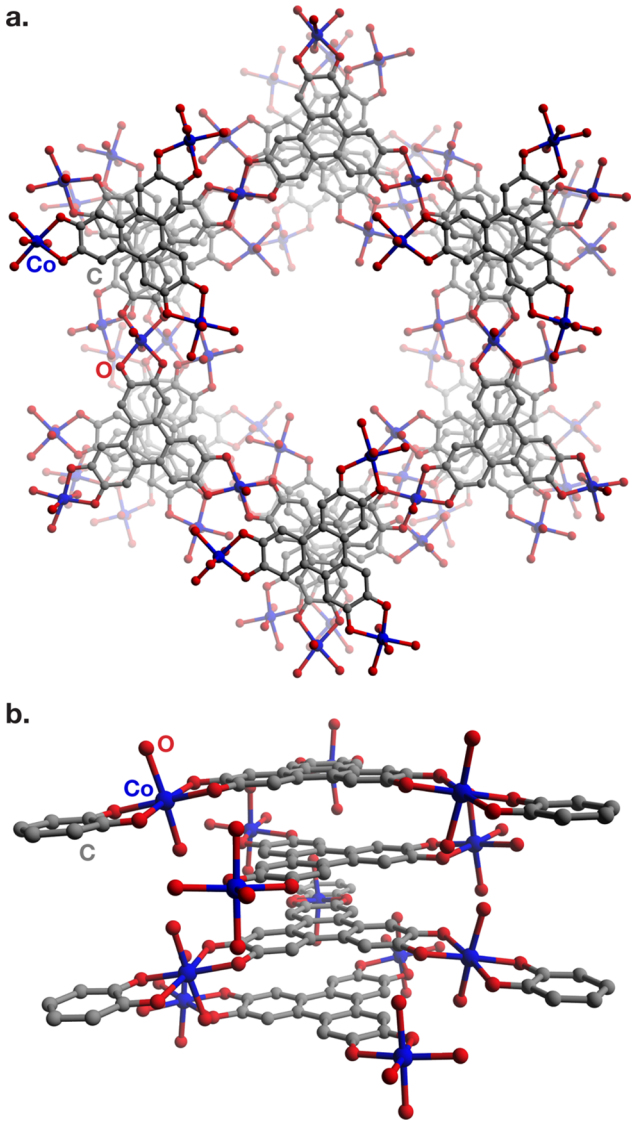

Figure 15. Structure of $Co_9(HOTP)_4$, showing (a) view of 2D honeycomb layers with octahedrally coordinated Co centers bridging triphenylene-based linkers, alternating with layers of trinuclear molecular clusters, and (b) stacking arrangement of the extended and molecular layers in the material.[148]

framework layers retain the same $M^{II}_3HOTP^{3-}_2$ configuration, while the molecular clusters have the neutral $[(H_2O)_5M^{II}]_3HOTP^{6-}$ assignment. However, we note that HOTP and M−O bond lengths in the clusters and in the framework are nearly identical, differing by <0.01 Å. Therefore, a model with homogeneous ligand oxidation states, in which the anionic $[M^{II}_{1.5}HOTP^{4.5-}]^{1.5-}$ framework layers are charge-balanced by the cationic $\{[(H_2O)_4M^{II}]_3HOTP^{4.5-}\}^{1.5+}$ layers, should also be considered.

Although the authors of the initial report focused on the structural aspects of the materials, they also measured the electrical conductivity of $Cu_3(HOTP)_2$ to be 0.1 S/cm in a single-crystal device contacted along the *c* axis—the highest value at the time for a porous MOF. Similar values have been reported for $Cu_3(HOTP)_2$ powders and films (from 0.02 to 0.2 S/cm).[22,160−167] Although the initial report did not include conductivity data for $Co_9(HOTP)_4$ and $Ni_9(HOTP)_4$, later studies[20,23,161,163,164,168] provided pressed powder pellet values in the range from 3×10^{-3} to 0.1 S/cm for $Ni_9(HOTP)_4$ and from 3×10^{-6} S/cm to 3×10^{-3} S/cm for $Co_9(HOTP)_4$ (see Table 3). Although an Fe-based HOTP material has also been reported, showing a conductivity of 3×10^{-3} S/cm, it appeared to be completely amorphous by PXRD.[163]

Recently, Song et al. synthesized thin films of $Cu_3(HOTP)_2$ with preferential orientation of the *ab* plane parallel to the substrate surface via a layer-by-layer method.[169] Four-probe measurements across the surface of the film (i.e., comprising predominantly in-plane contributions) showed a high conductivity of 0.29 S/cm. Variable-temperature measurements revealed an Arrhenius E_a of 0.13 eV above 240 K, with Mott VRH behavior below 200 K. The thin films were investigated as potential spin-valve materials in the same study.

In a recent report, Day et al. optimized the synthesis of $Cu_3(HOTP)_2$ to produce micron-sized crystals.[79] A detailed TEM and PXRD investigation showed that the layers in $Cu_3(HOTP)_2$ are in fact stacked in a slightly offset fashion with a continuous shift along the *c* direction, creating a tilted stack, as opposed to the straight stack of $Co_9(HOTP)_4$ (Figure 16). The authors also achieved synthetic control over the morphology of the crystallites, obtaining both needle-shaped crystals with the long axis aligned with the stacking direction, as well as shorter prism-shaped crystals with nearly isotropic dimensions. Sonication-assisted liquid-phase exfoliation of the prism-shaped crystals produced thinner hexagonal flakes. The authors used electron-beam lithography to fabricate four-point probe devices measuring conductivity both perpendicular to the MOF layers ("cross-plane"; measured on the needle crystals), and within the MOF layers ("in-plane"; measured on the exfoliated flakes). Surprisingly, the measured values of 1.5 S/cm for cross-plane devices and 0.5 S/cm for in-plane devices were within the same order of magnitude. This result challenges the view that conductivity in these materials is primarily due to intralayer transport; the most likely explanation to the high cross-plane conductivity values is interlayer charge transport mediated by close stacking and interactions between the π-systems of neighboring layers.

The significance of $\pi-\pi$ stacking with respect to the charge transport of 2D layered MOFs showing intralayer extended conjugation remains an open question. The single-crystal studies by Day et al.[79] suggest significant $\pi-\pi$ stacking contributions, as equally high conductivities were found for in-plane and cross-plane devices for $Cu_3(HOTP)_2$. More focus was put toward $\pi-\pi$ stacking in this class of MOFs in a study by Skorupskii et al. investigating a series of $Ln_{1+x}(HOTP)$ (Ln = La^{III}, Nd^{III}, Ho^{III}, Yb^{III}) materials.[92] In contrast with the structure of $Cu_3(HOTP)_2$, the lanthanides are not located in the same plane as the linkers, but rather in-between the linker layers, connecting them into a 3D framework (Figure 17). In this structure, the HOTP linkers form continuous stacks with extremely close $\pi-\pi$ interactions of 3.0−3.1 Å. In addition, the precise $\pi-\pi$ stacking distances were found to correlate directly with the sizes of the lanthanide cations. The authors found that despite the lack of conjugation in the layers, these materials displayed high conductivities of up to 0.05 S/cm (for $Ho_{1+x}(HOTP)$). Importantly, the conductivity decreased with longer stacking distances separating the linkers: the conductivity of $La_{1+x}(HOTP)$ was 1×10^{-3} S/cm, which was attributed to the larger La^{III} pushing the layers farther apart. DFT calculations of the band structure of $Ln_{1+x}(HOTP)$ showed high band spread and metallicity in the cross-plane direction, with negligible contribution of Ln^{III} to the frontier

https://dx.doi.org/10.1021/acs.chemrev.9b00766
Chem. Rev. 2020, 120, 8536−8580

Table 3. Selected Properties for MOFs Based on O-Functionalized Flat, Conjugated Linkers

material[a]	description	σ (S/cm)[b]	σ method[c]	E_a (eV)[d]	BET SA (m^2/g)[e]	μ (cm^2 V^{-1} s^{-1})	ref
triphenylene-based MOFs							
$Co_9(HOTP)_4$		0.1	4-probe pellet				163
		0.032	vdP pellet		465		161
		3.3×10^{-3}	vdP film				161
		2×10^{-3}	2-probe pellet				20
$Cu_3(HOTP)_2$		1.5	4-probe sc (⊥)				79
		0.5	2-probe sc (∥)				79
	vac.	0.29	4-probe film	0.13			169
	vac.	0.21	4-probe sc				148
	Ar	0.045	vdP pellet		512		160
		0.027	vdP pellet		306		161
		0.02	2-probe pellet	0.16			162
		0.02	4-probe pellet				163
		0.02	2-probe film	0.16			162
		0.01	2-probe pellet				167
		$7.6(3) \times 10^{-3}$	4-probe pellet				164
		3×10^{-3}	2-probe pellet		540		165
		2×10^{-3}	2-probe pellet				22
		1×10^{-4}	4-probe film	0.24			166
$Fe_3(HOTP)_2$	amorphous	3×10^{-3}	4-probe pellet				163
$Ni_9(HOTP)_4$		0.010(3)	4-probe pellet				164
		0.01	4-probe pellet				168
		6.8×10^{-3}	vdP pellet		430		161
		6×10^{-3}	2-probe pellet				20
		1.1×10^{-3}	vdP film				161
		$1.6(2) \times 10^{-4}$	2-probe film				23
		2.7×10^{-6}	4-probe pellet				163
$La_{1+x}(HOTP)$	N_2	8.2×10^{-4}	2-probe pellet	0.26	325		92
$Nd_{1+x}(HOTP)$	N_2	8.0×10^{-4}	2-probe pellet	0.24	513		92
$Ho_{1+x}(HOTP)$	N_2	0.053	2-probe pellet	0.25	208		92
$Yb_{1+x}(HOTP)$	N_2	0.010	2-probe pellet	0.25	452		92
MOFs based on other linkers							
$Cu_3(HOB)_2$	N_2	7.3×10^{-8}	vdP pellet	0.5	158		170
$Cu_3(HOTP)(THQ)$	Ar	2.35×10^{-5}	2-probe pellet	0.3	441		171
$Cu_2[Cu(OPc)]$		$\sim 1 \times 10^{-7}$	2-probe pellet		358		172
$Cu_2[Ni(ONPc)]$		0.0313	4-probe pellet		267		25
$Cu_2[Ni(OPc)]$		0.0143	4-probe pellet		284		25
$K_3Fe_2[Fe(OPc)]$		$\sim 1 \times 10^{-5}$	vdP pellet	0.261	206	4.35 (h, pellet Hall) 15(2) (TRTS)	173
$Ni_2[Ni(ONPc)]$		0.0178	4-probe pellet		174		25
$Ni_2[Ni(OPc)]$		7.22×10^{-4}	4-probe pellet		101		25

[a]See Abbreviations. [b]Measured at room temperature (exact temperature unspecified) or between 295 and 302 K. [c]∥ denotes device contacted in-plane/parallel to 2D layers; ⊥ denotes device contacted cross-plane/perpendicular to 2D layers. [d]Derived from Arrhenius model. For materials exhibiting more than one distinct activation regions, E_a at 300 K is given. [e]Calculated from N_2 adsorption isotherms.

bands—indicating that the transport occurs primarily through π−π interactions of organic linkers and not Ln−O chains. Taken together, these findings demonstrated the importance of the cross-plane charge transport in these materials.

3.2.1.2. Other Semiquinoid Linkers. $Cu_3(HOB)_2$, a material based on the smaller hexahydroxybenzene (H_6HOB) linker and Cu^{II}, was also investigated for its charge transport properties.[170] The structure of the material resembles $Cu_3(HOTP)_2$ but with smaller pores due to the smaller ligand core. Despite the similarities, the material showed a significantly lower conductivity of 7.3×10^{-8} S/cm in a two-probe pellet configuration at room temperature. The temperature dependence of the conductivity was fitted to give an Arrhenius E_a of 0.45 eV, similar to many other materials in this class. A curious feature of $Cu_3(HOB)_2$ is the extremely close stacking of its layers, which are separated by only 2.96 Å, which may lead to a more significant contribution of cross-plane charge transport to the electrical conductivity.

A hybrid of $Cu_3(HOTP)_2$ and $Cu_3(HOB)_2$ was recently reported by Yao et al.[171] In $Cu_3(HOTP)(HOB)$, the two linkers alternate within the layer, forming an ordered layered trigonal network. The layers stack in an eclipsed fashion, forming continuous 1D channels, similar to $Cu_3(HOTP)_2$. This structure resulted in high intrinsic porosity, with a BET surface area of 441.2 m^2/g. Two-probe pressed pellet measurements revealed a conductivity of 2.53×10^{-5} S/cm, considerably lower than that of $Cu_3(HOTP)_2$ (up to 0.2 S/cm), but higher than $Cu_3(HOB)_2$ (7.3×10^{-8} S/cm). The temperature dependence of the conductivity similarly showed an E_a of 0.30 eV—in-between those of $Cu_3(HOTP)_2$ and $Cu_3(HOB)_2$. This work served as another demonstration of the tunability of MOFs.

https://dx.doi.org/10.1021/acs.chemrev.9b00766
Chem. Rev. 2020, 120, 8536−8580

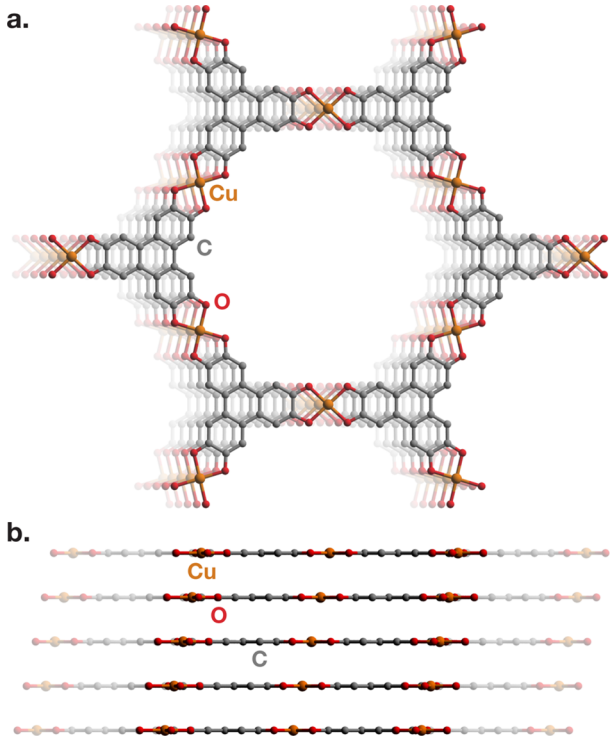

Figure 16. Structure of $Cu_3(HOTP)_2$, showing (a) 2D honeycomb layers with square planar Cu centers bridging triphenylene-based linkers and (b) continuous slipped stacking arrangement of layers.[79]

A number of semiquinoid linkers with metallophthalocyanine (M′(OPc))[25,172] and metallonaphthalocyanine (M′(ONPc))[25] cores were also used to synthesize conductive MOFs. The resulting frameworks have the formulas $M_2[M'(OPc)]$ and $M_2[M'(OPc)]$, respectively, where M is the framework metal and M′ is the central (Pc) metal. From simulations based on PXRD patterns, $Cu_2[Cu(OPc)]$ consists of 2D square grids of Cu(OPc) linkers connected by Cu^{II} atoms in a square-planar environment, similar to $Cu_3(HOTP)_2$ (Figure 18). The authors proposed an eclipsed stacking model for the materials with square channels of ∼15 Å in diameter. Permanent porosity was confirmed by N_2 adsorption, which revealed a BET surface area of 358 m^2/g. The electrical conductivity of pressed pellets ranged between 10^{-8} S/cm and 10^{-6} S/cm, significantly lower than for HOTP-based materials. A later study reported Ni^{II} and Cu^{II}-based Ni(OPc) and Ni(ONPc) MOFs, which were found to be isostructural to $Cu_2[Cu(OPc)]$.[25] These materials showed considerably higher conductivities, ranging from 10^{-4} to 10^{-2} S/cm, with the Cu^{II}-based materials showing higher values compared to Ni^{II} (the authors did not propose an explanation for this difference).

Feng and co-workers also reported an all-Fe phthalocyanine-based framework with the formula $K_3Fe_2[Fe(OPc)]$.[173] X-ray photoelectron spectroscopy (XPS) indicated a mixture of Fe^{II} and Fe^{III} in the samples (the authors were not able to distinguish between the framework and central Pc Fe sites). The relatively low BET surface area, 206 m^2/g, was attributed to the K^+ counterions in the pores. The conductivity of a van der Pauw pellet was $\sim 1 \times 10^{-5}$ S/cm at 300 K, with a high-temperature E_a of 0.26 eV. Hall measurements revealed p-type behavior with a hole concentration of $\sim 2.4 \times 10^{-14}$ cm^{-3} and mobility of ∼0.1 $cm^2\ V^{-1}\ s^{-1}$. Noncontact TRTS measurements estimated a higher mobility of 15(2) $cm^2\ V^{-1}\ s^{-1}$ for

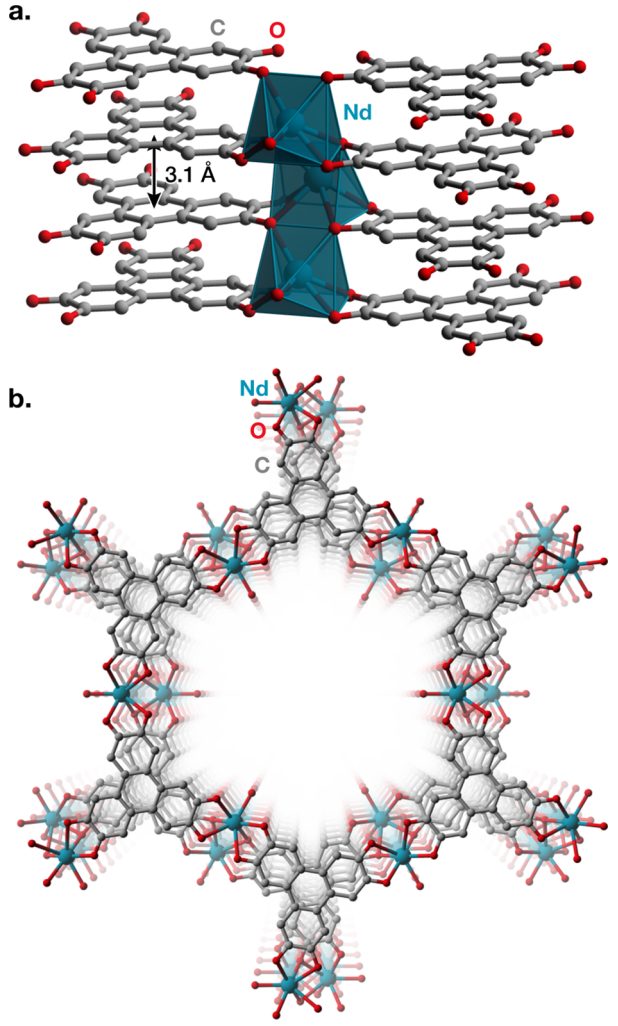

Figure 17. Structure of $Nd_{1+x}(HOTP)$,[92] showing (a) Nd coordination environment and close $\pi-\pi$ stacking distances among triphenylene linkers and (b) 1D channels along the ligand stacking direction.

photogenerated carriers. Ferromagnetic ordering up to 350 K in this material was also observed through magnetometry.

3.2.2. Thiolate Linker-Based Materials. *3.2.2.1. Triphenylenehexathiolate MOFs.* Initial work on MOFs with thiol-functionalized triphenylenes[174] and benzenes[65] was largely inspired by the nickel bis(dithiolene) motif in molecular complexes.[175] This fragment exhibits strong charge delocalization and planar geometry, which are enabled by the redox noninnocence of the ligand. Nickel bis(dithiolene) complexes are also redox-active, exhibiting several reversibly accessible states. These features led researchers to believe that extending the motif into a coordination polymer would allow for the formation of an extended π-conjugated sheet akin to graphene.

The framework $Pt_3(THT)_2$ (THT = 2,3,6,7,10,11-triphenylenehexathiolate), reported in 2014 by Xu and Cui,[174] exhibited both permanent porosity (300–400 m^2/g) and electrical conductivity (1.4×10^{-6} S/cm). The as-made material was anionic but could be oxidized into an almost neutral framework with I_2. No significant impact of oxidation on the conductivity was observed. As expected from the very strong and covalent bonding between Pt and thiol ligands, the material was not highly crystalline, with only broad peaks present in the PXRD pattern. Nevertheless, the unit cell

https://dx.doi.org/10.1021/acs.chemrev.9b00766
Chem. Rev. 2020, 120, 8536–8580

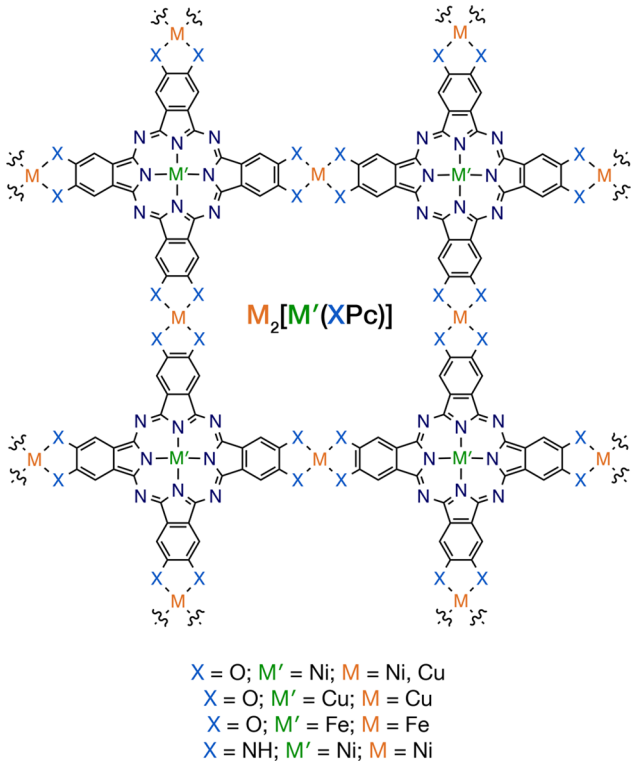

Figure 18. Representation of the structure of square 2D sheets in MOFs based on phthalocyanine (Pc) linkers with various functional groups (X) and framework and central Pc metals (M and M′, respectively).

dimensions agreed with a structure containing the ligands connected by square-planar Pt^{II} ions into a hexagonal net.

Materials with similar structures were also isolated with Co^{II} and Fe^{III}.[78,176] $Co_3(THT)_2$ shows somewhat improved crystallinity compared to $Pt_3(THT)_2$ and was first investigated as an electrocatalyst for H_2 evolution.[16] The material was porous (370 m^2/g) and exhibited a conductivity of 1.4×10^{-3} S/cm at 300 K in a van der Pauw geometry, considerably higher than the Pt analog. The temperature dependence of the conductivity was complex and warrants further investigation: the authors saw an increase in resistivity with decreasing temperature (as would be expected for a semiconductor) for temperatures close to room temperature, and the opposite (as would be seen for a metal) in the low-temperature regime (below ~180 K). We caution that similar behavior can be interpreted as phase artifacts in alternating current measurements of resistive samples. Interestingly, from the theoretical computations, the authors concluded that despite the highly covalent bonding in the sheet, the main mechanism for charge transport is expected to be along the *c* (stacking) direction. Also of note is the mixed valency of the metal ions: magnetometry results suggested that the correct charge assignment for the material is $[Co^{III}_2Co^{II}(THT)_2]^{3-}$.

$Fe_3(THT)_2$ displayed the highest conductivity to date among THT materials, reaching 3.4×10^{-2} S/cm at 300 K in a four-probe device.[78] This material was permanently porous, with a BET surface area of 526 m^2/g. Although the PXRD patterns were not of sufficiently high quality to resolve the exact stacking sequence, both PXRD and high-resolution TEM measurements proved the overall layered honeycomb structure, similar to $Pt_3(THT)_2$ and $Co_3(THT)_2$. The study reported Hall effect and THz spectroscopy measurements to extract a charge mobility value of ~200 $cm^2\ V^{-1}\ s^{-1}$, depending on the measurement. We note that discussions of the material as both heavily doped semiconductor (in the main text) and as an intrinsic semiconductor (in the Supplementary Information) are present in ref 78. The overall semiconducting behavior, however, was conclusively proven by variable temperature conductivity measurements. Optical absorption data suggested a direct band gap of 0.245 eV, matching well with the DFT calculated value of 0.350 eV. Interestingly, although the authors started with Fe^{II} salts and allowed no exposure to oxidants during the reaction, the metal charge state in the final material is Fe^{III}. As metal-based mixed valency provides an excellent way to introduce free carriers, a more rigorously air-free synthesis could allow access to a $Fe^{II/III}$ mixed material. A later work[177] proposed different Fe oxidation states and reported unusual maxima in variable temperature conductivity behavior (as with the report on the Co analog of this material,[176] we caution that similar behavior can be interpreted as phase artifacts). Clearly, this is a material that warrants further investigation and that could benefit from a systematic variation of synthetic conditions, as well as additional transport measurements.

The Feng group also reported a related material with Fe^{III}, $Fe_3(PTC)$ (PTC = perthiolated coronene).[178] This framework was essentially nonporous: the type II N_2 adsorption isotherm revealed a (primarily external) surface area of 210 m^2/g. The simulated structures contained acetylacetonate-like coordination modes of the thiols to the metal, unlike the typical catechol-like mode observed in $Pt_3(THT)_2$. Although the authors discussed several potential layer stacking sequences, they did not elaborate on the assignment of this particular Fe−S coordination mode. Similar to $Fe_3(THT)_2$, despite using an Fe^{II} salt in oxidant-free conditions, the metal charge state in the material was assigned unambiguously to Fe^{III}. The material displayed very high conductivities of up to 10 S/cm for pressed pellets in van der Pauw geometries. The conductivity increased with decreasing temperature with an Arrhenius E_a of 0.2 eV, similar to most MOFs discussed in this section. Importantly, this material was also ferromagnetic below ~20 K and is the only material in this class with reported magnetic ordering.

THT materials with Ni^{II} and Cu^{II} have also been reported,[179] but the structural analysis was based on PXRD patterns with essentially no discrete peaks, and thus no definite conclusions on the structures can be made.

3.2.2.2. Benzenehexathiolate MOFs. In a foundational work in 2013, Kambe et al. incorporated the nickel bis(dithiolene) motif into a π-conjugated 2D material, the $Ni_3(BHT)_2$ (BHT = benzenehexathiolate) framework.[65] The as-synthesized material, which was characterized as a thin black film, showed a two-probe pressed pellet conductivity value of 0.15 S/cm and a four-probe conductivity of 2.8 S/cm (reported in a later work by the same group).[94] The higher four-probe value is likely the result of eliminating contact resistance.

These authors also probed the charge states of nickel bis(dithiolene) fragments in the MOF, and the dependence of conductivity on the redox assignments. Infrared (IR) spectroscopy and XPS studies showed that the as-synthesized material contained mixed-valence 0 and −1 charge states, with an average charge of −3/4. Both the pure 0 and −1 states were accessible through electrochemical means and chemical oxidation/reduction (in contrast with molecular species, only the 0/−1 couple appeared to be reversible). Compared to the

https://dx.doi.org/10.1021/acs.chemrev.9b00766
Chem. Rev. 2020, 120, 8536−8580

Table 4. Selected Properties for MOFs Based on S-Functionalized Flat, Conjugated Linkers

material[a]	description	σ (S/cm)[b]	σ method	E_a (eV)[c]	BET SA (m^2/g)[d]	μ ($cm^2\ V^{-1}\ s^{-1}$)	ref
triphenylene-based MOFs							
$Co_3(THT)_2$	He	$1.39(14) \times 10^{-3}$	4-probe pellet		370		176
$Fe_3(THT)_2(NH_4)_3$	vac.	0.034	4-probe film		526	125(9) (TRTS) 211(7) (TRTS) 229(33) (film Hall)	78
$Pt_3(THT)_2$		3.86×10^{-4}	2-probe pellet				174
	act.	2.47×10^{-4}	2-probe pellet		329		174
	ox. (I_2)	1.09×10^{-4}	2-probe pellet		391		174
benzene-based MOFs							
$Ag_3(BHT)_2$	He	363	4-probe film		dense		185
$Ag_5(BHT)$	He	250	4-probe film	0.0163	dense		184
	He	50	4-probe pellet		dense		184
	red. ($LiBHEt_3$)	0.073	4-probe pellet		dense		184
$Au_3(BHT)_2$		1.12×10^{-4}	4-probe film				185
$Cu_3(BHT)$		2500	4-probe film		dense		186
	He	1580	4-probe film	0.002	dense	116 (*e*), 99 (*h*) (FET)	76
		280	4-probe pellet		dense		187
		48	4-probe pellet		dense		187
$Ni_3(BHT)_2$	ox., vac.	160	4-probe film	0.010			94
	vac.	2.80	4-probe film	0.026			94
		0.15	2-probe pellet				65
	red.	6.7×10^{-3}	2-probe pellet				65
$Pb_3(BHT)$		2×10^{-6}	2-probe pellet	0.37	dense		183
$Pb_{2.96}Tl_{0.04}(BHT)$	doped (Tl^+)	1×10^{-4}	2-probe pellet		dense		183
$Pd_3(BHT)_2$		2.8×10^{-2}	4-probe film				180
MOFs based on other linkers							
$Cu_3(BHSe)$		110	4-probe pellet		dense		182
$Fe_3(PTC)$	vac.	10	vdP pellet		210		178

[a]See Abbreviations. [b]Measured at room temperature (exact temperature unspecified) or between 295 and 300 K. [c]Derived from Arrhenius model. For materials exhibiting more than one distinct activation regions, E_a at 300 K is given. [d]Calculated from N_2 adsorption isotherms.

as-synthesized mixed-valent MOF (2.8 S/cm), the fully reduced material in the −1 state showed a lower conductivity of 6.7×10^{-3} S/cm. The oxidized material in the 0 state showed the highest conductivity of 160 S/cm.

DFT calculations and photoelectron spectroscopy (PES) suggested that both the as-made and the reduced materials were metallic in nature. However, the temperature dependence of the conductivity showed thermally activated behavior characteristic for a narrow-gap semiconductor. The authors proposed that the discrepancy could be a result of structural disorder in the real materials.

A palladium coordination polymer of BHT was later reported by the same group[180] and was proposed to have a similar structure to $Ni_3(BHT)_2$ based on TEM data. However, PXRD analysis revealed no discrete peaks, and the electron diffraction data were of poor quality, prohibiting detailed structural characterization. Initial synthetic attempts led to coprecipitation of Pd^0 nanoparticles, along with the proposed MOF. Addition of an oxidizing buffer in the form of $K_3[Fe(CN)_6]$ allowed the authors to generate pure $Pd_3(BHT)_2$, as evidenced by TEM. The material exhibited a similar charge state to $Pd_3(BHT)_2$, with the palladium bis(dithiolene) fragment present in mixed-valence 0/−1 states. The average charge state was found to be −0.19, which was higher than seen in as-made $Ni_3(BHT)_2$, likely because of the oxidizing buffer added to prevent formation of Pd^0 nanoparticles. The electrical conductivity of the pure $Pd_3(BHT)_2$ material was reported to be of similar magnitude to the Pd^0-contaminated material (2.8×10^{-2} S/cm), though the precise value was not specified. This conductivity is noticeably lower than that of $Ni_3(BHT)_2$, although the sample quality of $Pd_3(BHT)_2$ was significantly worse as well, prohibiting any definite conclusions.

The dense coordination polymer $Cu_3(BHT)$ reported by Huang et al. in 2015 holds the record for the highest conductivity in MOFs with low or minimal porosity (Table 4).[76] Although the material is nonporous, its structure and composition are related to other materials in this family, meriting inclusion in this Review. In contrast to $Ni_3(BHT)_2$, in which the BHT linker acts as a tritopic ligand, in $Cu_3(BHT)$ the ligand bonds to six Cu^{II} ions, thus increasing the framework density (Figure 19). The conductivities of $Cu_3(BHT)$ are the highest values reported for coordination polymers. Initial four-probe measurements on thin films revealed a value of 1580 S/cm at room temperature. In later studies by the same group on more crystalline samples,[181] the conductivities reached 2500 S/cm for a similar configuration. Interestingly, while the initial work reported a 3D Mott VRH dependence of electrical conductivity, which is characteristic for semiconductors, the later study showed a metallic dependence. As the authors noted, this is likely due to the drastically improved crystallinity of the material in the later study. Field-effect transistors based on $Cu_3(BHT)$ films[76] displayed very high (~100 $cm^2\ V^{-1}\ s^{-1}$) electron and hole mobilities, along with low (~10) on/off ratios, which the authors likened to the behavior of gapless graphene. The very low on/off ratios are in good agreement with the metallic temperature dependence shown in the later study. Importantly,

https://dx.doi.org/10.1021/acs.chemrev.9b00766
Chem. Rev. 2020, 120, 8536−8580

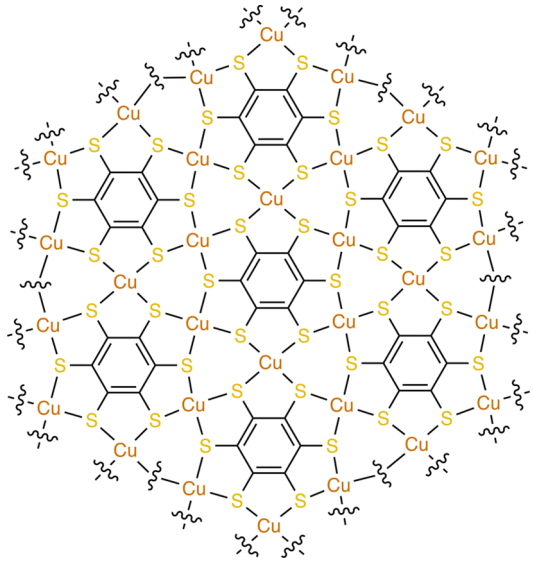

Figure 19. Representation of the structure of a 2D layer of the coordination polymer $Cu_3(BHT)$, showing dense coordination of square planar Cu centers by benzenehexathiolate linkers.

$Cu_3(BHT)$ was also reported to transition into a superconducting state (exhibiting zero electrical resistance) below 0.25 K, marking the first such observation for a coordination polymer or MOF.[181] The components of this structure responsible for the superconductivity—or even the metallic transport—in this material remain to be definitively identified. More efficient stacking, higher framework density, or stronger Cu−S bonds all potentially play a role.

The Zhu group also reported the selenolate analog of $Cu_3(BHT)$, denoted as $Cu_3(BHSe)$.[182] The conductivity of a pressed pellet of this dense coordination polymer was 110 S/cm, similar to that of $Cu_3(BHT)$. Although thermally activated conductivity was observed, the authors proposed that $Cu_3(BHSe)$ may also be metallic due to weak temperature dependence and strong absorption throughout the IR region, with semiconductor-like behavior induced by grain boundaries.

Another dense phase structurally related to $Cu_3(BHT)$ was reported in 2008 by Turner et al.[183] This framework, $Pb_3(BHT)$, has the same overall placement of linkers in layers but contains larger Pb^{II} atoms sitting in between the layers and binding them into a 3D solid. The material showed only low conductivities of 2×10^{-6} S/cm for a two-probe pressed pellet. The conductivity nevertheless increased by 2 orders of magnitude to 0.1×10^{-3} S/cm after doping with Tl^{I}.

A well-characterized dense Ag^{I} BHT polymer was also reported,[184] with a structure unrelated to $Cu_3(BHT)$ or $Ni_3(BHT)_2$. The material showed high conductivity values of up to 250 S/cm. Its structure contains many potential pathways for conductivity, including infinite Ag−Ag and Ag−S−Ag chains, and the origin of charge transport is likely different from that in $Cu_3(BHT)$ and $Ni_3(BHT)_2$. Another work reported Ag^{I} and Au^{I} coordination polymers based on BHT, which were inferred to be dense phases isostructural to $Cu_3(BHT)$.[185] However, the reported PXRD patterns bear little resemblance to those of the Cu analog, and no attempts at fitting were shown. The materials showed high conductivities of up to 363 S/cm for $Ag_3(BHT)$, and up to 1.12×10^{-4} S/cm for $Au_3(BHT)$.

3.2.3. Iminosemiquinoid Linker-Based Materials.

3.2.3.1. Hexaiminotriphenylene MOFs. The highest conductivity in a porous MOF to date belongs to $Ni_3(HITP)_2$ (HITP = 2,3,6,7,10,11-hexaiminotriphenylene), first reported by Sheberla et al.[75] Just like $Ni_3(BHT)_2$ is inspired by metal dithiolene complexes, the design of $Ni_3(HITP)_2$ is based on the $Ni(isq)_2$ complex, which has a fully conjugated biradical ground state.[188] As was initially proposed based on DFT calculations and later confirmed in a detailed TEM study,[79] $Ni_3(HITP)_2$ forms a structure similar to $Cu_3(HOTP)_2$, where the honeycomb layers stack in a slipped but near-eclipsed fashion, creating micropores of ∼1.6 nm in diameter (Figure 20). Unlike $Cu_3(HOTP)_2$, the offset direction in $Ni_3(HITP)_2$

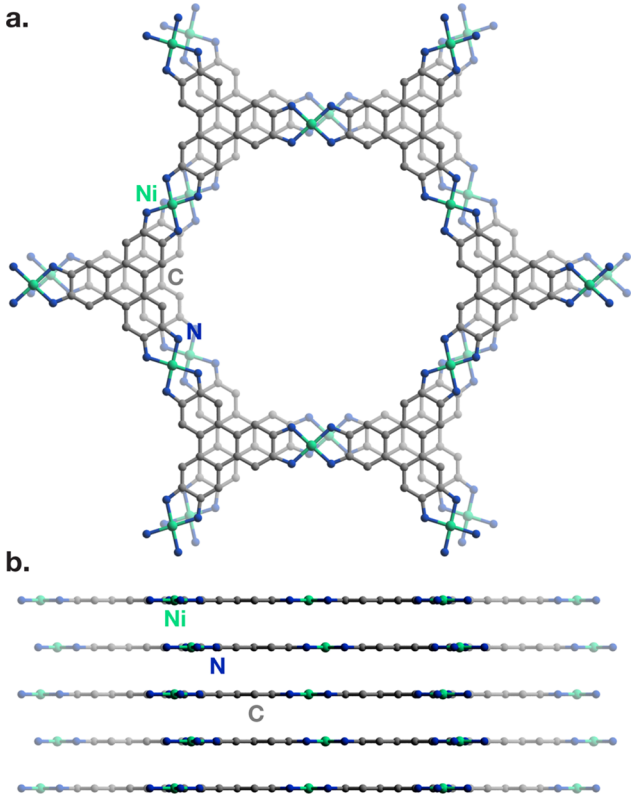

Figure 20. Structure of $Ni_3(HITP)_2$, showing (a) 2D honeycomb layers with square planar Ni centers bridging triphenylene-based linkers, and (b) ABAB stacking arrangement of layers.[75,79]

alternates every layer (ABAB), creating a straight rather than a tilted stack. The initial paper reported four-probe film and pressed pellet conductivities of 40 and 10 S/cm, respectively, which were the highest values shown by a porous material at the time. The temperature dependence of the conductivity was thermally activated and linear over an unusually large temperature range. Although consistent with semiconductor-type behavior, this behavior did not fit to a specific transport model. The material showed intrinsic microporosity with a relatively high surface area of 630 m^2/g.[17] A number of later studies reported conductivities ranging from $2.6(3) \times 10^{-3}$ to 150 S/cm for $Ni_3(HITP)_2$.[22,23,27,79,189]

High quality thin films of this landmark material were later reported by Wu et al., who fabricated field-effect transistors[190] from $Ni_3(HITP)_2$. These devices revealed p-type semiconducting behavior with a high hole mobility of ∼40 $cm^2 V^{-1} s^{-1}$. This mobility is higher than for most organic

https://dx.doi.org/10.1021/acs.chemrev.9b00766
Chem. Rev. 2020, 120, 8536−8580

Table 5. Selected Properties for MOFs Based on N-Functionalized Flat, Conjugated Linkers

material[a]	description	σ (S/cm)[b]	σ method	E_a (eV)[c]	BET SA (m^2/g)[d]	μ (cm^2 V^{-1} s^{-1})	ref
triphenylene-based MOFs							
$Co_3(HITP)_2$		8×10^{-4}	4-probe pellet		340		191
$Co_{2.14}Ni_{0.86}(HITP)_2$		5×10^{-3}	4-probe pellet				191
$Co_{1.27}Ni_{1.73}(HITP)_2$		0.024	4-probe pellet				191
$Co_{0.73}Ni_{2.27}(HITP)_2$		0.032	4-probe pellet				191
$Cu_3(HITP)_2$		0.2	2-probe pellet				21
		0.2	2-probe pellet				22
$Ni_3(HITP)_2$	vac.	150	4-probe sc (‖)[e]				79
	vac.	50	vdP pellet		630[17]		27
		40	vdP film				75
	vac.	2	2-probe pellet				75
		2	2-probe pellet				22
		1.9	4-probe pellet		282		191
		0.228	2-probe film				189
	amorphous	$2.6(3) \times 10^{-3}$	2-probe film				23
						48.6 (*h*, FET)	190
						45.4 (*h*, FET)	197
benzene-based MOFs							
$Co_3(HIB)_2$	vac.	1.57	4-probe pellet		240		28
$Cu_3(HIB)_2$	vac.	13	vdP pellet	0.608	114		77
$Fe_3(HIB)_2$		149.2	vdP pellet				30
$Mn_3(HIB)_2$		107.7	vdP pellet				30
$(Mn/Fe)_3(HIB)_2$		359	vdP pellet		2298		30
$Ni_3(HIB)_2$	vac.	8	vdP pellet		151		77
	vac.	0.7(15)	4-probe pellet				29
	vac.	0.11(3)	4-probe pellet		353		29
MOFs based on other linkers							
$Ni_2[Ni(IPc)]$	He	0.2	4-probe film	0.11	593		193
$Ni_3(HITP)_2$ (annulated)	ox. (I_2)	0.01	4-probe pellet		47		194
		insulating	4-probe pellet				194
$Ni_3(TABTT)_2$	ox.	0.1	vdP pellet	0.041			195
	Ar or N_2	3×10^{-6}	vdP pellet				196

[a]See Abbreviations. [b]Measured at room temperature (exact temperature unspecified), 298 K, or 300 K. [c]Derived from the Arrhenius model. For materials exhibiting more than one distinct activation region, E_a at 300 K is given. [d]Calculated from N_2 adsorption isotherms. [e]‖ denotes device contacted in-plane/parallel to 2D layers.

semiconductors and is likely responsible for the high electrical conductivity of the material. The depletion-mode behavior of the FETs indicated that the as-made material possessed a sufficiently high carrier concentration. The FETs exhibited high on/off ratios of up to 1000.

The excellent bulk transport properties align well with what chemical intuition would predict based on the structure of $Ni_3(HITP)_2$. Strong in-plane bonding between the iminosemiquinone $HITP^{3-}$ linker and Ni^{II} and close (3.35 Å) near-eclipsed stacking of the π-conjugated layers both contribute to charge delocalization and high mobility. Further oxidation of the iminosemiquinone linkers leads to removal of electrons—formation of excess holes—in the material, producing a p-type semiconductor. These results, taken together with the temperature dependence, are consistent with $Ni_3(HITP)_2$ being a semiconductor.

Surprisingly, in a later study, Day et al. fabricated single-crystal four-probe devices of $Ni_3(HITP)_2$, which revealed higher conductivities (up to 100 S/cm) and, more importantly, a nonzero conductivity at temperatures approaching 0 K.[79] Day et al. proposed that this behavior can be explained by metallic charge transport in the material.[79] This apparent disagreement between the FET study and the single-crystal study can perhaps be resolved by a computational investigation by Foster et al.,[63] which showed that disorder and defects in $Ni_3(HITP)_2$ can lead to the opening of a band gap in the otherwise metallic material.

A Cu^{II}-based HITP material has also been reported, with a structure apparently similar to $Ni_3(HITP)_2$. $Cu_3(HITP)_2$ showed conductivities as high as 0.2 S/cm for two-probe pressed pellet measurements.[21] Poor air stability of the material precluded further investigations.

Recently, Lian et al. reported the novel $Co_3(HITP)_2$ MOF, as well as mixed-metal $Co_xNi_{3-x}(HITP)_2$ MOFs.[191] However, the crystallinity of the $Co_3(HITP)_2$ samples was very poor and may be at least partially responsible for the relatively low bulk conductivity of 8×10^{-4} S/cm, several orders of magnitude lower than that of pure $Ni_3(HITP)_2$ synthesized via similar methods (0.19 S/cm). The mixed-metal Co/Ni MOFs showed increasing conductivities with increasing Ni content. Because of the lack of structural data, it remains to be determined whether the lower conductivity of $Co_3(HITP)_2$ compared to $Ni_3(HITP)_2$ is a result of different electron counts, structural distortions, layer stacking patterns, or other factors.

3.2.3.2. Hexaiminobenzene MOFs. A number of materials based on hexaiminobenzene (HIB), the nitrogen-containing analog of benzenehexathiol and hexahydroxybenzene, have also been made. The first report of a coordination polymer based

https://dx.doi.org/10.1021/acs.chemrev.9b00766
Chem. Rev. 2020, 120, 8536−8580

on this linker was in 2017 by Lahiri et al.[192] The study showed synthesis of thin films of HIB materials based on Cu^{II}, Ni^{II}, and Co^{II}. Although little experimental evidence was provided in support of structural claims, the materials showed hexagonal symmetry based on electron diffraction patterns. No conductivity values were reported, although FET devices were fabricated, demonstrating semiconducting behavior.

Two later reports discussed the Cu^{II} and Ni^{II}-based frameworks in more detail, showing that their structures were both similar to that of $Ni_3(BHT)_2$.[29,77] In $Ni_3(HIB)_2$ and $Cu_3(HIB)_2$, however, the hexagonal honeycomb layers stacked in a slipped-parallel fashion, as opposed to the eclipsed arrangement in $Ni_3(BHT)_2$. The reported conductivities varied between the different reports, ranging from 0.7 S/cm to 10 S/cm for $Ni_3(HIB)_2$ and from 0.11 S/cm to 0.7 S/cm for $Cu_3(HIB)_2$. Ultraviolet photoemission spectroscopy for both materials showed a nonzero charge density at the Fermi level—similar to $Ni_3(BHT)_2$—indicating metallicity. However, the temperature dependence of the electrical conductivity of both $Ni_3(HIB)_2$ and $Cu_3(HIB)_2$ again showed a semiconductor-type dependence and was attributed to intergrain contributions dominating charge transport that is otherwise intrinsically metallic (i.e., metallic transport within a single-crystal particle but temperature-activated transport between particles). $Ni_3(HIB)_2$ and $Cu_3(HIB)_2$ showed BET surface areas of 100−150 m^2/g with type II N_2 adsorption isotherms, indicating mostly external surface adsorption—unsurprising given the extremely small particle size (∼10 nm) and small pore diameter (<1 nm).

A Co^{II}-based material with a structure similar to that of $Ni_3(HIB)_2$ was reported by Park et al., who proposed an eclipsed arrangement of the layers in the Co analog (unlike the Cu and Ni materials).[28] This stacking mode led to permanent microporosity with a BET surface area of 240 m^2/g. The electrical conductivity of the material, as determined from two-probe pressed pellet measurements, ranged from ∼0.1 to 1.57 S/cm, similar to the Cu^{II} and Ni^{II} materials.

Nanoparticulate $Fe_3(HIB)_2$ and $Mn_3(HIB)_2$ showed some of the highest conductivities observed in MOFs,[30] reaching 100−360 S/cm at 300 K for pressed pellets. The authors attributed the transport properties to high crystallinity of their materials: the PXRD patterns appear to be better resolved than for other $M_3(HIB)_2$ materials. PXRD and TEM suggested that the materials have an eclipsed arrangement of the 2D layers, which may also have contributed to the higher conductivities. Interestingly, the materials were obtained as multishelled hollow sphere hierarchical structures, which led to very high surface areas of over 2300 m^2/g.

3.2.3.3. Other Iminosemiquinoid Linkers. Jia et al. reported an octaiminophthalocyanine (IPc)-based Ni^{II} MOF, similar in structure to $M_2[M'(OPc)]$ materials mentioned above.[193] Consistent with the general trend of imino-functionalized linkers engendering higher conductivities than their oxy-functionalized counterparts, $Ni_2[Ni(IPc)]$ showed a significantly higher conductivity as compared to $Ni_2[Ni(OPc)]$, with values as high as 0.2 S/cm reported for four-probe pellet measurements.

In a recent report, Jiang et al. studied a material based on $Ni_3(HITP)_2$ in which the $[NiN_4]$ sites were capped with propylene fragments, forming macrocyclic tetraaza[14]-annulene linkages.[194] This framework exhibited the same honeycomb structure as $Ni_3(HITP)_2$ and was calculated to favor a similar slipped-parallel stacking. The as-made material, synthesized in air-free conditions, was fully insulating, but oxidation with I_2 led to a drastic increase in conductivity to 0.01 S/cm. While technically the material could be considered a covalent organic framework beyond the scope of this Review, this work showcases the structurally tunable nature of conductive MOFs. Further work is necessary to determine the origin of the substantial differences in charge transport behavior of this material and $Ni_3(HITP)_2$.

The group of Nishihara, which originally reported $Ni_3(BHT)_2$, later reported a Ni^{II} coordination polymer based on 1,3,5-triaminobenzene-2,4,6-trithiol, which can be thought of as a hybrid of benzenehexathiol and hexaaminobenzene. Both an oxidized[195] and a reduced form of this material have been reported.[196] The reduced form showed sharp PXRD peaks ascribed to the staggered arrangement of the hexagonal conjugated layers, similar to $Ni_3(BHT)_2$. The oxidized form presumably has a similar structure. The reduced material exhibited a low conductivity of 3×10^{-6} S/cm, which increased to 0.3 S/cm upon oxidation, as indicated by pressed pellet measurements. This change is unsurprising given that the reduced form is unlikely to possess a significant number of free carriers, which typically originate from the oxidation of the amino moieties into their radical iminosemiquinonate form. The relative conductivities are also consistent with a DFT study of the material, which indicated the oxidized form to be metallic, and the reduced form to be a semiconductor with a band gap >1.0 eV. The two forms of the material were interconvertible by solution-phase oxidation with ferrocenium tetrafluouroborate or reduction with decamethylcobaltocene.

4. THROUGH-SPACE PATHWAYS

Unlike the previous two strategies, the through-space approach focuses on intermolecular interactions of organic linkers instead of covalent metal−ligand bonds. Largely inspired by organic semiconductors and charge-transfer salts, this approach utilizes the high propensity of planar conjugated organic ligands to form structures containing $\pi-\pi$ stacking in the solid state. The intrinsic tunability of MOFs can allow for fine control over the stacking sequence and distance to a degree that is difficult to achieve in classical polymeric and molecular materials. As is the case for the other approaches, mixed valency plays a crucial role: partial oxidation of organic ligands[37,85,198] provides charge carriers and potentially even biases the system toward the formation of $\pi-\pi$ interactions during synthesis.[199]

Frameworks based on tetrathiafulvalene (TTF), an archetypal organic semiconductor building block, constitute a large portion of MOFs designed with this approach in mind. Some of the most detailed studies correlating $\pi-\pi$ stacking configuration and conductivity were performed on materials made from TTF-based ligands. In particular, these studies demonstrate how varying parameters such as metal size[84] and solvent ratios[85] can result in structural changes that allow control over transport properties. That said, studies of these materials are not limited to TTF-based MOFs, and $\pi-\pi$ stacking between a diverse set of other organic cores, including anthracene,[38] naphthalene,[89] and napthalenediimide,[90,91] has so far enabled efficient charge transport (Table 6). Clearly, given the vast arsenal of organic molecules that have been employed in organic semiconductors with $\pi-\pi$ stacking in mind, we expect that this approach will become much more popular in the future.

https://dx.doi.org/10.1021/acs.chemrev.9b00766
Chem. Rev. 2020, 120, 8536−8580

Table 6. Selected Properties of MOFs with Through-Space Pathways for Charge Transport

material[a]	description	σ (S/cm)[b]	σ method[c]	E_a (eV)[d]	BET SA (m^2/g)[e]	μ ($cm^2\ V^{-1}\ s^{-1}$)	ref
tetrathiafulvalene tetrabenzoate-based MOFs							
Cd_2(TTFTB)		$2.9(5) \times 10^{-4}$	2-probe sc		559		84
		$2.5(5) \times 10^{-4}$	2-probe sc	0.293			56
		1.91×10^{-4}	4-probe sc				56
		4.39×10^{-6}	4-probe pellet				56
		2.7×10^{-6}	vdP pellet				56
		$2.1(1) \times 10^{-6}$	2-probe pellet				56
		$2.4(7) \times 10^{-7}$	2-probe sc (⊥)[f]				56
Co_2(TTFTB)		$1.5(3) \times 10^{-5}$	2-probe sc		665		84
Mn_2(TTFTB)		$9(1) \times 10^{-5}$	2-probe sc		594		84
Zn_2(TTFTB)		5.0×10^{-4}	TRTS				206
		$4.0(6) \times 10^{-6}$	2-probe sc		662	0.2 (FP-TRMC)	37, 84
	ox. (I_2)	$2.5(2) \times 10^{-10}$	EIS				198
La_4(TTFTB)$_4$		$2.5(7) \times 10^{-6}$	2-probe pellet	0.28	596		85
La(TTFTB)		$9.0(4) \times 10^{-7}$	2-probe pellet	0.20	454		85
La_4(TTFTB)$_3$		$1.0(5) \times 10^{-9}$	2-probe pellet	0.44	362		85
Gd_3(TTFTB)$_2$(OAc)(OH)		2.0×10^{-7}	4-probe pellet				86
Tb_3(TTFTB)$_2$(OAc)(OH)		1.5×10^{-6}	4-probe pellet				86
Dy_3(TTFTB)$_2$(OAc)(OH)		3.9×10^{-7}	4-probe pellet				86
Ho_3(TTFTB)$_2$(OAc)(OH)		6.7×10^{-6}	4-probe pellet				86
Er_3(TTFTB)$_2$(OAc)(OH)		7.4×10^{-6}	4-probe pellet				86
Er_4(TTFTB)$_3$(I_3)$_2$	ox. (I_2)	2×10^{-8}	2-probe pellet				87
Er_4(TTFTB)$_3$		1×10^{-9}	2-probe pellet				87
Tb_4(TTFTB)$_3$(I_3)$_2$	ox. (I_2)	4×10^{-8}	2-probe pellet				87
Tb_4(TTFTB)$_3$		1×10^{-8}	2-probe pellet				87
Dy_4(TTFTB)$_3$(I_3)$_2$	ox. (I_2)	1×10^{-8}	2-probe pellet				87
Dy_4(TTFTB)$_3$		7×10^{-9}	2-probe pellet				87
Ho_4(TTFTB)$_3$(I_3)$_2$	ox. (I_2)	8×10^{-9}	2-probe pellet				87
Ho_4(TTFTB)$_3$		1×10^{-9}	2-probe pellet				87
Dy(TTFTB)		3×10^{-7}	4-probe pellet				86
Yb_6(TTFTB)$_5$		$9(7) \times 10^{-7}$	2-probe pellet				88
Lu_6(TTFTB)$_5$		$3(2) \times 10^{-7}$	2-probe pellet				88
tetrathiafulvalene tetrapyridyl-based MOFs							
Fe(dca)[TTF(py)$_4$](ClO_4)		1.2×10^{-7}	2-probe pellet				207
	ox. (I_2)	7.6×10^{-5}	2-probe pellet				207
Fe(dca)$_2$[TTF(py)$_4$]$_{0.5}$		4.1×10^{-9}	2-probe pellet				207
	ox. (I_2)	1.3×10^{-6}	2-probe pellet				207
Mn(dca)$_2$[TTF(py)$_4$]$_{0.5}$		6.3×10^{-9}	2-probe pellet				208
Mn(N_3)[TTF(py)$_4$](ClO_4)		1.5×10^{-9}	2-probe pellet				208
$MnCl_2$[TTF(py)$_4$]		2×10^{-10}	2-probe pellet				208
MOFs based on other linkers							
$ZnNa_2$(AnBEB)$_2$		$1.3(5) \times 10^{-3}$	2-probe sc		collapse		38
Cd(DPNDI)		0.033	2-probe sc				90
		7.6×10^{-6}	2-probe pellet				90
	act.	0.037	2-probe pellet				90
Cu(DPNDI)$_2$		1.2×10^{-5}	2-probe sc				91
$Cd_{2.39}$(TPDAP)$_3$		1×10^{-6}	2-probe sc				210
Cd_2(TPDAP)$_2$		insulating	2-probe sc				210

[a]See Abbreviations. [b]Measured at room temperature (exact temperature unspecified) or between 293 and 300 K. [c]Single-crystal devices are contacted parallel to the π−π stacking direction unless otherwise indicated. [d]Derived from Arrhenius model. For materials exhibiting more than one distinct activation regions, E_a at 300 K is given. [e]Calculated from N_2 adsorption isotherms. [f]Contacted perpendicular to π−π stacking direction.

In most of the existing examples, π−π stacking between ligands results in the formation of 1D conduction pathways. However, more unusual and complex arrangements, such as zigzag chains and orthogonal orientations, have also been reported.[38,88] Many 2D extended conjugation MOFs also exhibit significant π−π stacking among the covalently bonded layers, and as previously discussed, this stacking may in fact contribute as much to the conductivity as the in-plane conjugation. Therefore, charge transfer between organic components is a pervasive motif in conductive MOFs regardless of their categorization.

4.1. Tetrathiafulvalene-Based Frameworks

TTF is an organosulfur compound that is an excellent electron donor.[200] The stability of its radical cation form has made it a popular component in conducting charge-transfer salts, in which π−π stacking and close intermolecular contacts in

https://dx.doi.org/10.1021/acs.chemrev.9b00766
Chem. Rev. 2020, 120, 8536−8580

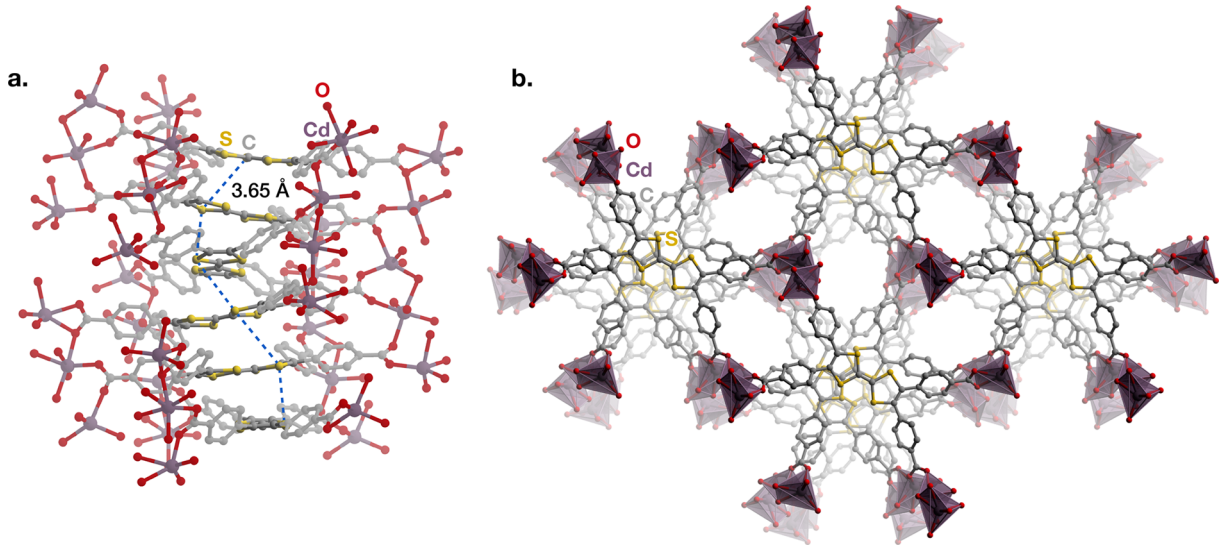

Figure 21. Structure of Cd_2(TTFTB) showing (a) infinite 1D helical stacking of tetrathiafulvalene cores with a continuous close S···S contact of 3.654(2) Å and (b) 1D channels parallel to the stacking direction.[84]

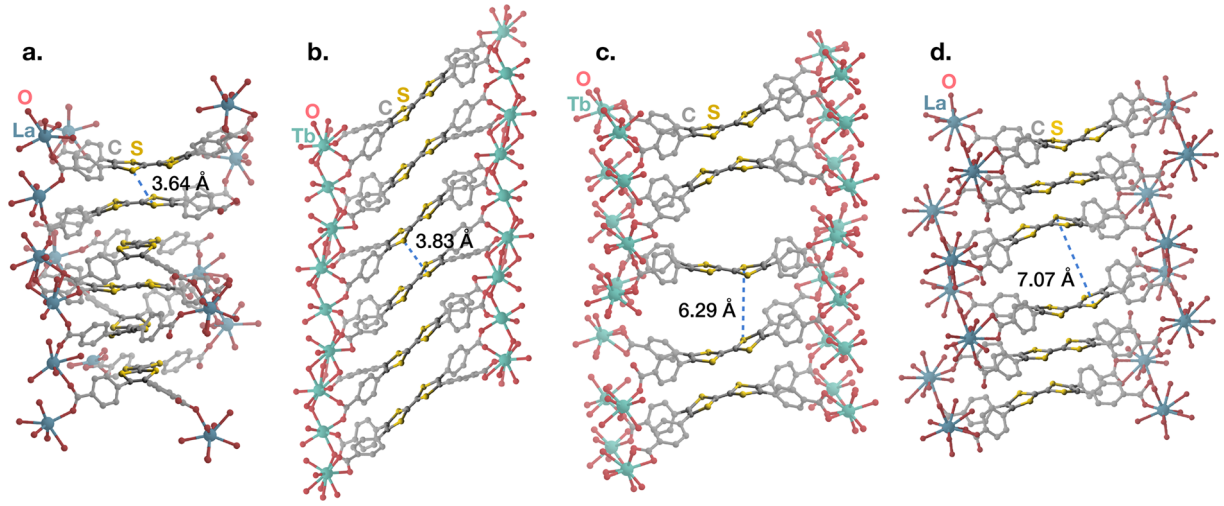

Figure 22. Structures of (a) La_4(TTFTB)$_4$, (b) Tb_3(TTFTB)$_2$(OAc)(OH), (c) Tb_4(TTFTB)$_3$, and (d) La_4(TTFTB)$_3$ with the longest S···S contact distances indicated.[85−87]

oxidized TTF stacks facilitate charge transport.[201] Functionalized TTF derivatives are also used in supramolecular chemistry because of their redox activity and participation in noncovalent interactions.[202,203] As a result of their electroactive nature and $\pi-\pi$ stacking propensity, ligands based on TTF form conductive MOFs with a diverse range of structures. We note that conductive, nonporous coordination polymers containing TTF-based linkers, such as TTF tetracarboxylate,[204] have been reported and reviewed.[205]

The isostructural series of M^{II}_2(TTFTB) frameworks (M = Mn, Co, Zn, and Cd; TTFTB = tetrathiafulvalene tetrabenzoate) reported by Narayan et al.[37] and Park et al.[84] contain infinite 1D helical stacks of TTF (Figure 21). They are permanently porous, with BET surface areas between 559 and 665 m^2/g. The single-crystal structures of these MOFs showed that the TTF moieties within the stacks have a single close S···S contact distance of <3.8 Å. As the size of the M^{II} cation increases, the stack effectively becomes pinched, shortening the S···S distance from 3.773(3) Å for Co^{II} to 3.654(2) Å for Cd^{II}.

The single-crystal conductivities measured along the stacking direction for the M_2(TTFTB) frameworks showed a striking correlation with the S···S distances, with average values of $2.9(5) \times 10^{-4}$ S/cm for Cd_2(TTFTB), $9(1) \times 10^{-5}$ S/cm for Mn_2(TTFTB), $1.5(3) \times 10^{-5}$ S/cm for Co_2(TTFTB), and $4.0(6) \times 10^{-6}$ S/cm for Zn_2(TTFTB). DFT band structure calculations indicated that the valence band comprises S and C orbitals from the ligand TTF core, and has a large dispersion of 400 meV. Increasing the size of the metal cation and contracting the stacking distance increases the overlap of S p_z orbitals and, thus, the charge mobility along the TTF stacks. Detailed investigations of the electrochemical and spectroscopic properties of these MOFs further confirmed the central role of the TTF core, showing that ligand-based IVCT mediates the charge transport.[198] The large band dispersion leads to high charge mobilities in these frameworks: FP-TRMC and TRTS studies of Zn_2(TTFTB) revealed a mobility value[37] of 0.2 $cm^2\ V^{-1}\ s^{-1}$, and photoconductivity (with 400 nm pump-pulses) of 5×10^{-4} S/cm.[206]

https://dx.doi.org/10.1021/acs.chemrev.9b00766
Chem. Rev. 2020, 120, 8536−8580

The large (up to 1 mm in length), high-quality single crystals that can be obtained for these M_2(TTFTB) phases have enabled thorough characterization of their properties: for example, Cd_2(TTFTB) was used as a model system for a comparative study of techniques to measure conductivity in MOFs.[56]

Several different TTFTB MOFs based on lanthanides show diverse structures, while retaining the general trend of conductivities correlating inversely with S···S contact distances. Xie et al. reported three TTFTB MOFs with La^{III} which crystallize with 1D stacks of TTFTB ligands and rectangular pores.[85] Notably, the H_2O to DMF ratio used in their synthesis appeared to play a role in determining the extent of $\pi-\pi$ stacking. The two more conductive phases showed average conductivity values of $2.5(7) \times 10^{-6}$ and $9(4) \times 10^{-7}$ S/cm, respectively, with longest S···S contacts of 3.640(4) and 4.083(3) Å. The third phase was significantly less conductive ($1.0(5) \times 10^{-9}$ S/cm) and has a much longer S···S contact of 7.072(7) Å. The BET surface areas of these polymorphs ranged between 362 and 596 m^2/g.

TTFTB-based MOFs with middle and late lanthanides also showed polymorphism dependent on the synthesis conditions (Figure 22). Castells-Gil et al. reported[86] two structure types of TTFTB frameworks with Gd^{III}, Tb^{III}, Dy^{III}, Ho^{III}, and Er^{III}. M_3(TTFTB)$_2$(OAc)(OH), featuring continuous $\pi-\pi$ stacking with S···S contact distances of <4 Å, showed consistently higher conductivities, with the highest value of 1.5×10^{-5} S/cm measured in the Tb^{III} material. A different family of frameworks with Tb^{III}, Dy^{III}, Ho^{III}, and Er^{III} reported by Su et al. do not have close or continuous $\pi-\pi$ stacking and consistently exhibited relatively low conductivities between 10^{-9} and 10^{-8} S/cm, with marginal increases upon doping with I_2.[87] The smallest lanthanides, Tm^{III}, Yb^{III}, and Lu^{III}, form TTFTB MOFs with unusual 2D structures and showed conductivities up to 2.6×10^{-6} S/cm.[88] In contrast with the 1D TTF stacks in most other phases with this ligand, these MOFs contain one ligand oriented orthogonally to the others.

Assuming that electron transfer between TTF cores dominates charge transport in TTFTB MOFs, the longest S···S contact in 1D ligand stacks should limit the overall rate of charge transfer in the stack. Hence, the value of the shortest S···S contact between each pair of adjacent ligands, denoted as $(S\cdots S)_{min}$, should be correlated with the conductivity. Indeed, plotting the conductivities of these materials vs the longest crystallographic $(S\cdots S)_{min}$ contacts in each structure shows an inverse correlation between these parameters (Figure 23).[85] This general trend suggests that intermolecular TTF distances determine the bulk conductivities of these MOFs across different structures and compositions. Similar trends should be observed for other MOFs where the dominant transport pathway is through close ligand···ligand π-based interactions.

For instance, other TTF-containing frameworks have been synthesized with the tetrathiafulvalene tetrapyridyl (TTF-(py)$_4$) ligand. Wang et al. reported two polymorphic Fe^{II} materials, Fe(dca)$_2$[TTF(py)$_4$]$_{0.5}$ and Fe(dca)[TTF(py)$_4$]-(ClO_4).[207] They lack continuous $\pi-\pi$ stacking pathways and have conductivities on the order of 10^{-9} S/cm in their as-synthesized forms. Upon treatment with I_2, their conductivities increased to 1.3×10^{-6} and 7.6×10^{-5} S/cm because of the oxidation of the TTF cores to their radical cation state. Notably, the incorporation of I_3^- proceeded via a single crystal-to-single crystal transformation in the latter MOF. Yu et al. reported three Mn^{II} frameworks with TTF(py)$_4$ with similar

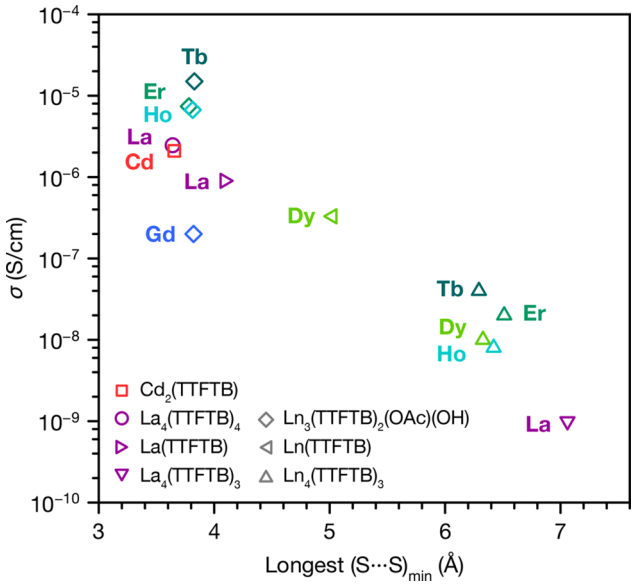

Figure 23. Pressed pellet conductivities of MOFs with the TTFTB ligand[85] and different metals plotted versus the longest crystallographic S···S contact distance between two neighboring ligands.

conductivities as the undoped Fe^{II} analogs (between 2.0×10^{-10} and 6.3×10^{-9} S/cm) because of the absence of close-stacking interactions in their structures.[208]

Wang et al. also combined the TTF(py)$_4$ ligand with TCNQ as both a second ligand and an interstitial guest in MOFs with Zn^{II} and Cd^{II}.[209] Though the combination of donor−acceptor systems in a single MOF framework is appealing for increasing conductivity, the conductivities of these frameworks were relatively low (~10^{-8} S/cm). After treatment with I_2, the conductivity of the Cd^{II} framework increased slightly to 2.16×10^{-7} S/cm, but no evidence of additional TTF(py)$_4$ oxidation was apparent (the interstitial $TCNQ^{\bullet-}$ was replaced with I_3^-). The modest conductivity values were attributed to large separation between the redox-active moieties and the orthogonality of TTF and TCNQ.

In most of these reports, EPR and optical absorption spectroscopy studies on TTF-based frameworks have generally indicated that they contain some $TTF^{\bullet+}$ species in their as-synthesized forms. Therefore, IVCT between partially oxidized TTF cores appears to be the general mechanism responsible for conductivity in these materials.

4.2. Other $\pi-\pi$ Stacked Frameworks

A number of other planar organic cores have been used to make electrically conductive MOFs, including anthracene, naphthalenediimide, and naphthalene. The resulting materials have generally been studied in isolated reports, and unifying or comparative studies have yet to be carried out. Nonetheless, some of the highest conductivity values for the through-space approach have been achieved in these MOFs. Hence, more systematic investigations into non-TTF $\pi-\pi$ stacked frameworks and their conductivities will accelerate development in this area and point out worthy synthetic targets for new linkers.

Chen et al. reported a mixed-metal MOF with the formula $ZnNa_2$(AnBEB)$_2$ (AnBEB = 4,4′-(anthracene-9,10-diylbis-(ethyne-2,1-diyl))dibenzoate) containing unusual zigzag packing of the anthracene moieties, with an interplanar distance of approximately 3.4 Å between neighboring ligands.[38] The conductivity from single-crystal measurements was 1.3(5) ×

https://dx.doi.org/10.1021/acs.chemrev.9b00766
Chem. Rev. 2020, 120, 8536−8580

10^{-3} S/cm. This high value was attributed to the relatively close stacking distances and the zigzag packing motif. In contrast to other MOFs in this category, there was no evidence of ligand-based mixed valency for this framework. After activation, crystallinity and porosity were lost due to structural collapse from removal of coordinated solvents.

Another study reported a porous Cd^{II} material with the *N*,*N*′-di(4-pyridyl)-1,4,5,8-naphthalenetetracarboxdiimide (DPNDI) linker.[90] The structure is a $\pi-\pi$ stacked assembly of linear $[Cd(OH_2)_4(DPNDI)]$ polymers, which arrange into a hexagonal framework. The interlayer stacking distance is remarkably short, at only 3.18 Å (compared to typical distances of ∼3.3 Å for napthalenediimide (NDI)-based molecules). This close stacking, along with the ability of the NDI core to form stable radical anions, led to high conductivities up to 3.3×10^{-3} S/cm measured on single crystals along the stacking axis. Measurements on pressed pellets yielded much lower values up to 7.6×10^{-6} S/cm, perhaps due to the considerable anisotropy of the material. Unexpectedly, the desolvated form showed a higher conductivity than either of the above (3.7×10^{-2} S/cm). However, the material exhibited a structural transition upon solvent removal, and its final structure was not fully determined.

Kuang et al. studied $Cu^{I}(DPNDI)_2$, an NDI-based framework with considerably further stacking distances than in the Cd^{II} material, with closest contacts of ∼3.7 A.[91] The NDIs are also offset horizontally, leading to reduced overlap of their π-systems. Despite this, the MOF demonstrated a relatively high conductivity of 1.2×10^{-5} S/cm, as determined from single-crystal measurements.

Another Cd^{II}-pyridyl-based framework, with the redox-active conjugated linker 2,5,8-tri(4-pyridyl)1,3-diazaphenalene, showed single-crystal conductivities of $\sim 1 \times 10^{-6}$ S/cm.[210] The intrinsically porous structure consists of continuous columns of the linkers, with a relatively short stacking distance of 3.3 Å. The same linker was also found to form a different framework with Cd^{II} without continuous stacking, which was insulating. The different transport properties between these two MOFs demonstrate the importance of a continuous charge transport pathway.

Dense naphthalene-based MOFs with $\pi-\pi$ stacking have also been reported to be conductive. Haider et al. obtained a dense Sr^{II} framework with 1,4,5,8-naphthalenetetracarboxylate that exhibited white-light emission.[89] This structure contains 2D sheets with Sr−carboxylate chains and closely stacked naphthalene cores separated by ∼3.4 Å and showed a conductivity of $\sim 10^{-4}$ S/cm.

Panda and Banerjee fabricated field-effect transistors based on a series of indium isophthalate frameworks.[211] Out of the three materials investigated, only one featured close $\pi-\pi$ stacking and showed a hole mobility of 4.6×10^{-3} cm^2 V^{-1} s^{-1}. Electrical conductivity of the material was not reported.

5. REDOX HOPPING

In this section, we summarize the transport properties of MOFs that do not conform to the above-mentioned design strategies. In general, these materials do not contain well-defined crystallographic pathways that could allow for band-like charge transport. Although many of these MOFs do contain redox-active components, they are separated by distances long enough to preclude direct orbital overlap. Therefore, charge hopping is the likely mechanism of conduction in these materials.

On average, the greater separation between hopping sites in these materials can be expected to coincide with lower charge mobilities compared to other classes of conductive MOFs. Consistent with this expectation, the highest conductivities for MOFs in this category[26,212,213] are lower than those falling under other design strategies. However, the wide range of conductivity values reported (Table 7) suggest that the factors limiting charge transport may vary widely among different materials (e.g., carrier concentration, carrier mobility, or grain boundary resistance), and can be difficult to predict from structural and compositional information alone.

In general, higher conductivities in this category appear to correlate with the presence of redox-active components in the MOFs (e.g., linkers featuring metal−dithiolene units,[26,64,214] conjugated organic cores,[213,215] and azo groups[212,216−219]). Excitation of mobile carriers from these motifs presumably facilitates conductivity.

5.1. Metal-Based Hopping

In 2009, Takaishi et al. reported $Cu[Cu(pdt)_2]$ (pdt = pyrazine-2,3-dithiolate], which exhibited a conductivity of 6×10^{-4} S/cm.[64] The authors hypothesized that linking the known electron acceptor $[Cu^{III}(pdt)]^-$ with donating Cu^{I} ions could lead to the formation of an electrically conductive MOF. The authors obtained a 3D porous framework with Cu centers in a square-planar geometry (Figure 24) upon reaction of $Na[Cu(pdt)_2]\cdot 2H_2O$ and CuI. Analysis of the bond lengths and angles from the X-ray crystal structure indicated that electron

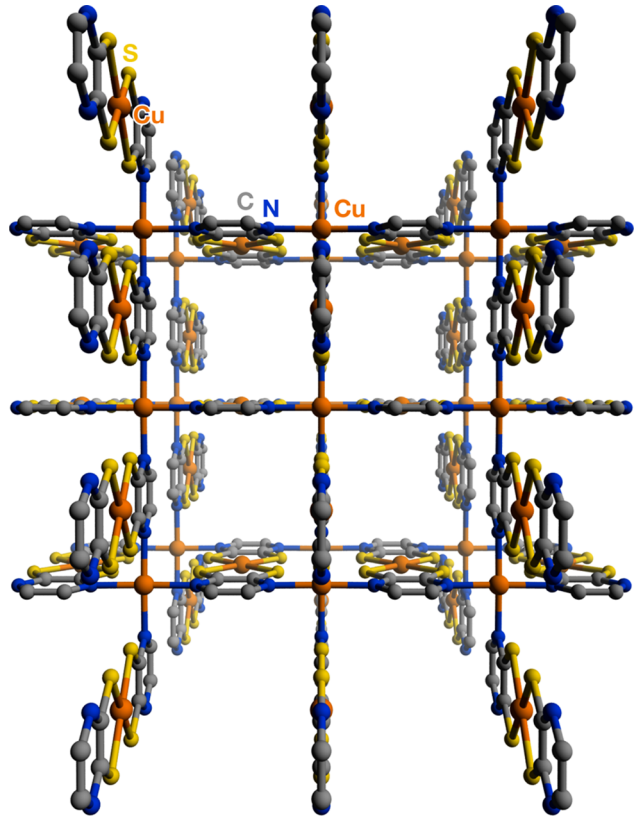

Figure 24. Structure of $Cu[Cu(pdt)_2]$ showing square channels formed by pyrazine-linked Cu centers and redox-active $[Cu(pdt)_2]^{2-}$ units.[64]

https://dx.doi.org/10.1021/acs.chemrev.9b00766
Chem. Rev. 2020, 120, 8536−8580

transfer had occurred between the donating and accepting fragments of the MOF, bringing both copper sites to a formal oxidation state of Cu^{II}. This oxidation state assignment was further corroborated by the paramagnetic behavior of the compound. The authors attributed the relatively high conductivity of the MOF to redox hopping among the Cu centers, perhaps facilitated by the charge bistability of $Cu^{I}[Cu^{III}(pdt)_2]$ and $Cu^{II}[Cu^{II}(pdt)_2]$ units.

While the crystal structure of $Cu[Cu(pdt)_2]$ contains 1D square channels filled with disordered solvent, Kobayashi et al. reported that the compound amorphized and collapsed upon desolvation.[214] They were able to synthesize the structural analog $Cu[Ni(pdt)_2]$, with Ni replacing Cu in the dithiolene-coordinated site. This mixed-metal MOF retained crystallinity and microporosity after activation, exhibiting a BET surface area of 385 m^2/g. The conductivity of as-synthesized $Cu[Ni(pdt)_2]$ was reported to be 1×10^{-8} S/cm in the original study and 2.6×10^{-6} S/cm in a later study.[26] Upon exposure to I_2 vapor, the conductivity increased to 1×10^{-4} S/cm without measurable incorporation of iodine species into the framework. Analogous to the case of $Cu[Cu(pdt)_2]$, redox hopping among partially oxidized nickel-dithiolene units is the likely mechanism of conduction. These results constitute the first example of a permanently microporous MOF with conductivity tunable over several orders of magnitude through doping.

Dolgopolova et al. studied the influence of exchanging Co^{II} into $Cu_3(BTC)_2$ (BTC = benzene-1,3,5-tricarboxylate) on its conductivity.[220] The particular choice of Co^{II} was motivated by an earlier computational study, which investigated the effects of partial metal substitution in MOF-5 on its electronic structure.[221] $Cu_{2.4}Co_{0.6}(BTC)_2$ was found to be somewhat more conductive than monometallic $Cu_3(BTC)_2$, with the conductivity increasing from 2.0×10^{-10} S/cm to 1.4×10^{-8} S/cm with the introduction of Co^{II}. In the same study, Dolgopolova et al. also provided a microwave conductivity investigation of the materials, showing that the effective conductivity of the exchanged material was approximately one order of magnitude higher than that of the original. This difference was attributed to the presence of Co^{II} midgap states, which can lower the energetic barrier to charge hopping.

An analogous strategy was employed by the same group to increase the conductivity of a bimetallic actinide framework $U_{1.23}Th_{4.77}O_4(OH)_4(NO_3)_2(Me_2BPDC)_5$ (Me_2BPDC^{2-} = 2,2′-dimethylbiphenyl-4,4′-dicarboxylate).[222] Introduction of Co^{II} ions into the framework led to the extension of the hexanuclear cluster node to give the formula $U_{1.23}Th_{4.77}Co_3O_4(OH)_4(NO_3)_2(Me_2BPDC)_5$ and resulted in enhancement of the electrical conductivity from 7.0×10^{-10} S/cm to 1.4×10^{-7} S/cm. DFT calculations showed narrowing of the bandgap upon addition of Co^{II} due to the addition of midgap Co−O-based states. This result is similar to what was observed in the previous $Cu_3(BTC)_2$ study and is most likely responsible for the improved charge transport.

5.2. Linker-Based Hopping

Dolgopolova et al. also investigated ways of controlling charge transport in photoresponsive MOFs using linker isomerization.[213] The authors synthesized a set of mixed-linker frameworks with photoactive spiropyran and diarylethene fragments in the linkers. The spiropyran fragments isomerize on exposure to UV light to form merocyanine zwitterions. Similarly, diarylethene moieties form more extended conjugated (closed) systems under UV-irradiation, which break up (open) following exposure to visible light at 590 nm (Figure 25a). The authors used these two transformations as switches

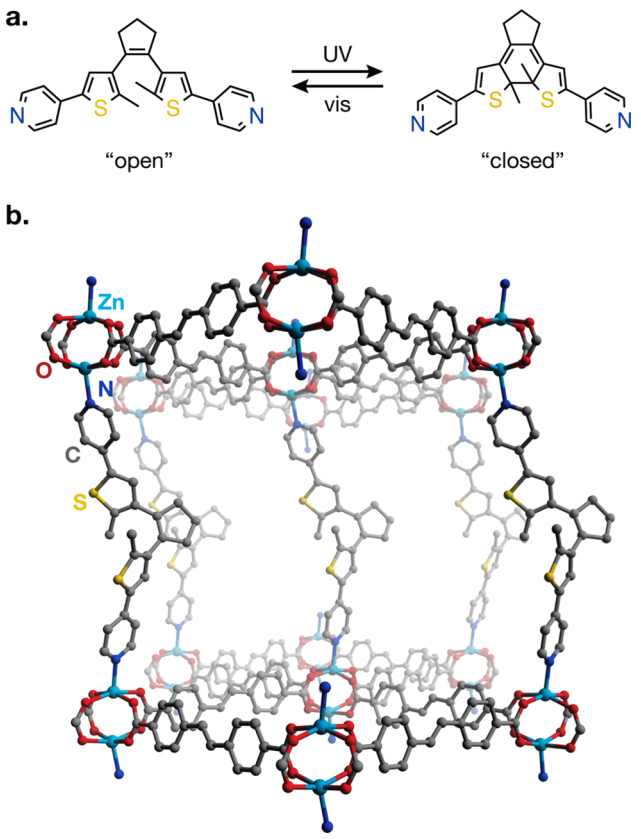

Figure 25. (a) Scheme showing photoswitchable isomerization of "open" and "closed" forms of diarylethene derivatives and (b) structure of $Zn_2(SDC)_2(BPMTC)$ with the "open" form of the diarylethene linker.[213]

for charge transport, hypothesizing that the different charge distribution and size of the conjugated system between the nonisomerized and isomerized linkers would affect the energetic and spatial separation between hopping sites, thus allowing control over the conductivity. They found that a spiropyran-containing MOF exhibited a reversible increase in the conductance of single crystals upon UV irradiation. Reverse isomerization of merocyanine at ambient conditions complicated the study, so the authors focused on photoactive systems using diarylethene (Figure 25b). Both in situ and ex situ conductivity and diffuse reflectance measurements on three different Zn^{II}- and Zr^{IV}-based frameworks containing diarylethene motifs showed small but statistically significant ($p < 0.05$) three- to four-fold increases in conductivity upon isomerization of the linker into its "closed" form (Table 7). This study demonstrated the first realization of photoswitchable charge transport in MOFs.

Goswami et al. studied the conductivity of $Zr_6(OH)_{16}(TBAPy)_2$ (NU-1000; TBAPy = tetrakis(p-benzoate) pyrene) thin films at 1.6 V vs Ag/AgCl using EIS.[223] At this potential, the TBAPy linker is expected to be present in both its closed-shell $TBAPy^{4-}$ and radical trianion $TBAPy^{\bullet 3-}$ forms. They discovered higher conductivities for films with preferential orientation along the *c* direction than those oriented along the *ab* direction, which is consistent with

https://dx.doi.org/10.1021/acs.chemrev.9b00766
Chem. Rev. 2020, 120, 8536−8580

Table 7. Selected Properties of MOFs Exhibiting Conduction Based on Redox Hopping Mechanisms

material[a]	description	σ (S/cm)[b]	σ method	E_a (eV)[c]	BET SA (m^2/g)[d]	ref
		metal-based hopping				
Cu[Cu(pdt)$_2$]		6×10^{-4}	(not reported)	0.193	collapse	64,214
Cu[Ni(pdt)$_2$]		2.6×10^{-3}	2-probe pellet			26
		1×10^{-8}	2-probe film	0.49	385	214
	ox. (I_2)	1×10^{-4}	2-probe film	0.18		214
$Cu_{2.4}Co_{0.6}(BTC)_2$		1.4×10^{-8}	2-probe pellet			220
$U_{1.23}Th_{4.77}O_4(OH)_4(NO_3)_2(Me_2BPDC)_5$		7×10^{-10}	2-probe pellet			222
$U_{1.23}Th_{4.77}Co_3O_4(OH)_4(NO_3)_2(Me_2BPDC)_5$	Co^{II} on nodes	1.4×10^{-7}	2-probe pellet			222
		linker-based hopping				
$Zn_2(BPDC)_2(BPMTC)$		$6.4(9) \times 10^{-7}$	2-probe pellet		dense	213
	irrad.	$1.7(3) \times 10^{-6}$	2-probe pellet		dense	213
$Zn_2(SDC)_2(BPMTC)$		$9.5(21) \times 10^{-7}$	2-probe pellet		dense	213
	irrad.	$2.9(7) \times 10^{-6}$	2-probe pellet		dense	213
$Zn_4O(NDC)_3$		0.0398	4-probe film			225
$Zr_6O_4(OH)_8(Me_2BPDC)_4$	with BCMTC	$1.3(3) \times 10^{-5}$	2-probe pellet			213
	with BCMTC, irrad.	$2.3(2) \times 10^{-5}$	2-probe pellet			213
$Zr_6(OH)_{16}(TBAPy)_2$ (NU-1000)	electrophoretic film	1.3×10^{-9}	thin film EIS (1.6 V vs Ag/AgCl)			223
	solvothermal film	1.2×10^{-7}	thin film EIS (1.6 V vs Ag/AgCl)			223
		mixed metal- and linker-based hopping				
Cd(3-bpd)(SCN)$_2$		4.53×10^{-7}	2-probe film diode		dense	218
Cd(4-bpd)(SCN)$_2$		2.9×10^{-6}	2-probe film diode		dense	219
Cd(azbpy)(mglu)		1.29×10^{-5}	2-probe film diode		dense	217
Cd(azbpy)(msuc)		2.64×10^{-5}	2-probe film diode		dense	217
Cd(azbpy)(suc)		3.20×10^{-5}	2-probe film diode		dense	217
$Cd_{1.5}(azbpy)_2(glu)(NO_3)$		2.07×10^{-5}	2-probe film diode		dense	217
$Cd_2(azbpy)_2(HIP)_2$		1.86	2-probe film diode		dense	212
Zn(azbpy)(HIP)		1.1×10^{-4}	2-probe film diode		dense	216
$Zn(azbpy)_{0.5}(HIP)$		2.5×10^{-5}	2-probe film diode		106	216
$Co_3[Co(TCPP)]_2$		3.62×10^{-8}	2-probe film (EIS)			227
$Mg_3Fe_2[Co(OPc)]$	ox. (I_2)	1×10^{-5}	2-probe sc		1481	101
Ni/Fe(NDC)	nanosheets	$1.0(2) \times 10^{-5}$	4-probe film		dense	229
Ni/Fe(NDC)	bulk	$1.0(5) \times 10^{-8}$	4-probe film		dense	229
$Na_3Pb_6(THT)_2(OH)$		1.1×10^{-6}	2-probe pellet			226
$Sm_2(BHC)$		1.46×10^{-5}	2-probe pellet		dense	232
Sr(1,2,4-BTC)		6×10^{-6}	2-probe pellet	0.17	dense	230
Sr(ntca)		1×10^{-4}	diode		dense	89
[Zn(SIP)][EMIM]		4.35×10^{-11} (373 K)	2-probe pellet (AC)	1.17	dense	231
Co-DAPV	no structure	0.035	4-probe film			233
Cu-BTC	no structure	8.3×10^{-8} to 5.3×10^{-11}	2-probe pellet		dense−850	234

[a]See Abbreviations. [b]Measured at room temperature (exact temperature unspecified) or 300 K unless otherwise indicated. [c]Derived from Arrhenius model. For materials exhibiting more than one distinct activation regions, E_a at 300 K is given. [d]Calculated from N_2 adsorption isotherms.

closer redox hopping distances along the *c* direction. As expected from the generation of more charge carriers (i.e., radical ligand species), the conductivity values obtained by this method (up to 1.2×10^{-7} S/cm) were significantly higher than those reported for NU-1000 without an applied potential (9.1×10^{-12} S/cm).[224]

Dawood et al. fabricated thin film devices of interpenetrated $Zn_4O(NDC)_3$ (NDC = 2,6-naphthalenedicarboxylate) using electron beam deposition of copper electrodes.[225] Surprisingly, these devices exhibited high conductivities up to 3.98×10^{-2} S/cm despite relatively discontinuous stacking in the structure of the MOF. The authors hypothesized that the interpenetrated arrangement of naphthalene cores allows for charge hopping.

5.3. Mixed Metal- and Linker-Based Hopping

Ghoshal and co-workers have reported several Zn^{II} and Cd^{II} frameworks with the 4,4′-azobispyridine linker and other carboxylate ligands, including 5-hydroxyisophthlate,[212,216] methylsuccinate, methylglutarate, and glutarate.[217] Their conductivities ranged from 1.29×10^{-5} S/cm[217] to 1.86 S/cm.[212] Roy and co-workers made Cd^{II} frameworks with an extended azo-based linker, 1,4-bis(3-pyridyl)-2,3-diaza-1,3-butadiene, with conductivities of 4.53×10^{-7} S/cm[218] and 2.90×10^{-6} S/cm.[219] All of these azo materials also exhibited Schottky diode-like behavior in thin film devices, with some increases in conductivity upon photoillumination. They were dense except for one Zn^{II} framework with 4,4′-azobispyridine and 5-hydroxyisophthlate, which displayed a BET surface area

https://dx.doi.org/10.1021/acs.chemrev.9b00766
Chem. Rev. 2020, 120, 8536−8580

of 105.8 m^2/g.[216] Redox-hopping among metal centers and $\pi-\pi$ interactions among the linkers were both proposed to contribute to the observed conductivity.

Huang et al. combined the triphenylenehexathiol (THT) ligand with Pb^{II} in order to obtain a framework with the formula $[Pb_6(THT)_2(OH)]^{3-}$ (charge-balanced by Na^+ in the pores).[226] While other MOFs with the THT ligands exhibit extended conjugation in 2D structures, the reaction conditions used in this study (using in situ deprotection of the linker to slow down crystallization) appeared to favor the formation of a 3D framework without close $\pi-\pi$ interactions or continuous through-bond pathways. The conductivity of this MOF (1.1×10^{-6} S/cm) was accordingly lower compared to other THT-based materials.

The charge transport and electrochemical properties of a porphyrin-based framework, $Co_3[Co(TCPP)]_2$ (TCPP = 5,10,15,20-(4-carboxyphenyl)porphyrin), was investigated by Ahrenholtz et al.[227] The conductivity measured by EIS on a thin film grown on FTO was 3.62×10^{-8} S/cm. Charge diffusion parameters from cyclic voltammetry and spectroelectrochemical analysis combined with the relatively low conductivity value were deemed consistent with a redox hopping mechanism of conduction between framework Co centers and the linker porphyrins. Another study reported the charge mobilities obtained by FP-TRMC measurements of two porphyrin-based MOF films, Zn[Pd(DPPDB)] and Zn[(H_2DPPDB)] (Pd(DPPDB) = palladium(II) 4,4′-(10,20-diphenylporphyrin-5,15-diyl)dibenzoate, and (H_2DPPDB) its free base porphyrin analog). These films, grown on conductive fluorine-doped tin oxide, showed mobilities of 0.002 $cm^2 V^{-1} s^{-1}$ for Zn[Pd(DPPDB)] and 0.003−0.004 $cm^2 V^{-1} s^{-1}$ for Zn[(H_2DPPDB)].[228]

Matheu et al. recently reported a 3D framework based on Co^{II} phthalocyanine with the OPc linker and Fe^{III} as the framework metal with the formula $Mg_3Fe_2[Co(OPc)]$.[101] Unlike other OPc frameworks, which form 2D sheets with extended metal−linker conjugation, this MOF contains no $\pi-\pi$ stacking, with all ligands being separated by more than 13 Å. The octahedral coordination of Co^{II} centers in the Pc units (with two axial aquo ligands) and the formation of $Fe_3(-C_2O_2-)_6(OH_2)_2$ SBUs likely both favor this more porous structure. Despite the long separation distance, the single-crystal conductivity (measured along the c direction, which contains continuous SBU−OPc linkages) was $\sim 10^{-5}$ S/cm. The relatively high value was attributed to charge hopping between redox-active Pc molecules and SBUs.

Duan et al. synthesized thin nanosheets of the dense 2D mixed-metal MOF (Ni/Fe)(NDC) for electrocatalytic water splitting.[229] The nanostructured MOF was significantly more conductive ($1.0(2) \times 10^{-5}$ S/cm) than the bulk MOF ($1.0(5) \times 10^{-8}$ S/cm), which was attributed to defects and vacancies induced by nanostructuring. The mixed-metal approach may also have introduced free charge carriers into the framework.

The conductivities of several dense frameworks with benzene-based carboxylate linkers without open-shell transition metals have been studied.[230−232] These values range from 10^{-11} to 10^{-5} S/cm. Hopping between the ligands or carboxylate-coordinated metal centers is likely to be responsible for the transport behaviors observed.

6. GUEST-PROMOTED TRANSPORT

Using host−guest interactions to increase conductivity is perhaps the strategy most specific to MOFs. By leveraging the intrinsic microporosity of MOFs, high loadings of electroactive molecules can be introduced into the pores to increase electrical conductivity (Table 8). In contrast with charge doping, which increases the number of charge carriers by reacting the material with (usually small quantities of) oxidizing or reducing species, guest-mediated conductivity commonly involves the introduction of stoichiometric amounts of new species into the MOF. These relatively high loadings of guests are usually necessary to form continuous charge transport pathways (and hence obtain high mobilities). Guests with extended structures, including conductive polymers and inorganic oxides, have also been introduced. In most cases, charge transfer between the framework and the guest appears to be important for increasing conductivity, presumably as a mechanism for generating free charge carriers.

The advantages of this strategy lie chiefly with the possibility of tuning the guest and framework properties in a synergistic fashion. Materials with highly tunable conductivities can be realized,[235] and conductivity modulation across 11 orders of magnitude have been demonstrated.[236] In addition, by selecting starting frameworks with high porosities and different pore sizes, the resulting guest@MOFs can retain high surface areas.[224,236−239] For frameworks that are less porous in their original state, partial loading of guests can potentially allow for the optimization of conductivity versus surface area. Matching the reduction potentials of the framework and guest,[236] as well as the sizes of the guest and pores,[240] are promising routes toward further customization of transport properties in this class of materials.

Although examples of crystallographically resolved guests exist,[224,241,242] the inclusion of guests and the formation of conductive pathways are often inferred from spectroscopic data that do not provide atomistic resolution. Finally, growth of conductive side products during guest infiltration can further complicate the attribution of increased conductivity to the guest@MOF assembly.[243] Detailed compositional and crystallographic studies, therefore, can clarify the mechanisms behind conductivity enhancement achieved through this strategy.

6.1. Iodine and Polyiodides

Although iodine loading into MOFs has been explored predominantly in the context of doping—with the charge transport happening through pathways intrinsic to the framework—conductivity mediated by encapsulated channels of iodide species has also been demonstrated. Zeng et al. found that a double-walled MOF $Zn_3(lac)_2(pybz)_2$ (pybz = 4-(pyridin-4-yl)benzoate, lac = DL-lactate) with 1D square channels incorporated I_2 upon soaking in a cyclohexane solution.[244] Conductivity measurements on single monoliths (loss of crystallinity was observed upon reaction with I_2) revealed a value of 3.42×10^{-3} S/cm along the direction of the channels. The Co^{II} analog incorporated a similar amount of I_2 but exhibited a lower pellet conductivity of 7×10^{-6} S/cm.[245] The authors of these studies proposed that charge transfer between iodide species and pybz π-electrons led to these relatively high conductivities (we note that the conductivities of the guest-free frameworks were not reported). However, loss of crystallinity upon I_2 incorporation made mechanistic interpretation challenging.

Yin et al. uncovered more definitive evidence of the role of polyiodide inclusion in a related system.[241] By including I_2 in the solvothermal reaction with Cu^{II} and pybz, they obtained

https://dx.doi.org/10.1021/acs.chemrev.9b00766
Chem. Rev. 2020, 120, 8536−8580

Table 8. Selected Properties of MOFs with Guest-Mediated Charge Transport Pathways

material[a]	description, guests	σ (S/cm)[b]	σ method[c]	E_a (eV)[d]	BET SA (m^2/g)[e]	ref
		iodine and polyiodides				
$Co_3(BDC)_3(bpz)_2$	I_2	1.56×10^{-6} (2.59×10^{-9})	2-probe pellet			242
$Co_3(lac)_2(pybz)_2$	I_2	7×10^{-6}	2-probe pellet			245
$Co_3(NDC)_2$	I_2	1.88×10^{-6}	Hall bar film			250
$Cu_6(pybz)_8(OH)_2$	I_5^-, I_7^-	8.11×10^{-7} (8.4×10^{-9})	2-probe film			241
$Eu_4(BPT)_4$	I_2	8.27×10^{-7}	2-probe pellet (EIS)	0.602	69.6	248
$Tb(Cu_4I_4)(PCA)_3$	I_2	2.16×10^{-4} (5.72×10^{-11})	2-probe sc			246
$V_2(OH)_2(BPTC)$	I_2, I_3^-	1.2×10^{-4} (1.7×10^{-10})	2-probe pellet (AC)			247
$Zn_3(lac)_2(pybz)_2$	I_2	3.42×10^{-3}	2-probe sc (∥)			244
	I_2	1.65×10^{-4}	2-probe sc (⊥)			244
		organic and organometallic molecules				
$Cd(TTF(py)_4)(TCNQ^{\bullet-})_{0.5}(NO_3)$	$TCNQ^{\bullet-}$	2.63×10^{-8}	2-probe pellet			209
$Cd(TTF(py)_4)(TCNQ^{2-})_{0.5}(NO_3)_{0.5}$	$TCNQ^{\bullet-}$ (air)	4.77×10^{-8}	2-probe pellet			209
$Cd(TTF(py)_4)(TCNQ^{2-})_{0.5}(NO_3)_{0.5}$	$TCNQ^{\bullet-}$ (air, I_2-treated)	5.97×10^{-8}	2-probe pellet			209
$Cd(TTF(py)_4)(TCNQ^{\bullet-})_{0.5}(NO_3)_{0.5}$	I_3^-	2.16×10^{-7}	2-probe pellet			209
$Cd(TTF(py)_4)(TCNQ^{2-})_{0.5}(NO_3)$	pristine	(1.05×10^{-8})	2-probe pellet			209
$Zn(TTF(py)_4)(TCNQ^{\bullet-})_{0.5}(NO_3)$	$TCNQ^{\bullet-}$	2.48×10^{-8}	2-probe pellet			209
$Cu(TPyP)Cu_2(OAc)_4$	TCNQ	1×10^{-6} (1×10^{-9})	4-probe film			258
$Cu_2(TATAB)_3$	TCNQ	2.67×10^{-7} (9.75×10^{-12})	2-probe pellet			256
$Cu_3(BTC)_2$ (HKUST-1)	TCNQ	0.07	2-probe film	0.041	214	235
	TCNQ	3×10^{-3}	2-probe film			253
	TCNQ	1.5×10^{-4}	2-probe pellet		573.7	243
	TCNQ	1.92×10^{-10}	2-probe Hg drop film			252
	ferrocene	3.57×10^{-15}	2-probe Hg drop film			259
	pristine	(2×10^{-9})	2-probe film			220
$Zn_2(TCPB)(BPDPNDI)$	MV^{2+}	$2.3(3) \times 10^{-3}$	4-probe film			240
	DFDNB	$3.5(6) \times 10^{-4}$	4-probe film			240
	DNT	$1.5(2) \times 10^{-4}$	4-probe film			240
	C_{60}	$4.0(6) \times 10^{-5}$	4-probe film			240
	pristine	(5.8×10^{-5})	4-probe film			240
$Fe_3O(TTFTB)_3$ (MUV-2)	C_{60}	4.7×10^{-9} (3.7×10^{-11})	2-probe pellet		1040	237
Zn(TPP)	C_{60}	1.5×10^{-11} (2×10^{-13})	2-probe film			260
$Zr_6(OH)_{16}(TBAPy)_2$ (NU-1000)	Ni(IV) bis(dicarbollide)	4.3×10^{-9} (9.1×10^{-12})	2-probe pellet		1260	224
$Zr_6(OH)_{16}(TBAPy)_2$ (NU-901)	C_{60}	1×10^{-3} ($<10^{-14}$)	2-probe pellet		1550	236
		conductive polymers and oxides				
$Cd_2(NDC)(PCA)_2$	polypyrrole	1×10^{-3}	4-probe pellet		dense	264
	polypyrrole	0.2	Hall bar pellet		dense	264
	I_2 (control)	2.9×10^{-7}	4-probe pellet			264
	pristine	(1×10^{-12})	4-probe pellet			264
Cr(OH)(BDC) (Cr-MIL-53)	PEDOT	1.1×10^{-3} ($<10^{-11}$)	2-probe pellet (EIS)		803	238
La(BTC)	PEDOT	2.3×10^{-8}	2-probe pellet (EIS)			238
$Zn_3(lac)_2(pybz)_2$	polypyrrole	0.01	2-probe sc		135	261
Al(OH)(BDC) (Al-MIL-53)	S	1.2×10^{-10}	2-probe pellet			215
	polypyrrole + S	2.71	4-probe pellet			215
	pristine	(1.39×10^{-7})	4-probe pellet		1370	215
$Cr_3OF(BDC)_3$ (Cr-MIL-101)	S	4.91×10^{-9}	2-probe pellet			215
	polypyrrole + S	0.472	4-probe pellet			215
	pristine	(4.42×10^{-7})	2-probe pellet		3250	215
$[Zr_6(OH)_{16}]_2(TCPP)_3$ (PCN-224)	S	1.2×10^{-10}	2-probe pellet			215
	polypyrrole + S	0.113	4-probe pellet			215
	pristine	(5.74×10^{-7})	2-probe pellet		2660	215
$Zr_6(OH)_{16}(TBAPy)_2$ (NU-1000)	SnO	1.8×10^{-7} (9.1×10^{-12})	2-probe film		680	239

[a]See Abbreviations. [b]Measured at room temperature (exact temperature unspecified) or 298 K. Value given in parentheses corresponds to pristine guest-free material. [c]∥ denotes device contacted parallel to guest-filled channels; ⊥ denotes device contacted perpendicular to channels. [d]Derived from Arrhenius model. For materials exhibiting more than one distinct activation regions, E_a at 300 K is given. [e]Calculated from N_2 adsorption isotherms.

$Cu_6(pybz)_8(OH)_2 \cdot I_5^- \cdot I_7^-$ with crystallographically resolved polyiodide anions incorporated into the channels. The conductivity of a thin film of the material was 8.11×10^{-7} S/cm. Soaking in methanol removed I_2 from the polyiodides to afford $Cu_6(pybz)_8(OH)_2(I^-)_2$ and lowered the conductivity by 2 orders of magnitude (8.04×10^{-9} S/cm). We note that,

https://dx.doi.org/10.1021/acs.chemrev.9b00766
Chem. Rev. 2020, 120, 8536−8580

while these pybz materials were porous in their original forms, with BET surface areas up to 800 m^2/g for $Co_3(DL\text{-}lac)_2(pybz)_2$, their porosities were likely not maintained after iodide inclusion. No adsorption measurements were attempted for any of these iodine-treated materials.

Hu et al. combined thorough crystallographic and physical characterization to explain the enhancement of transport properties in $Tb(Cu_4I_4)(PCA)_3$ (PCA = 4-pyridinecarboxylate) upon uptake of I_2.[246] The single-crystal conductivity of the parent material, which included framework iodide anions, was 5.72×10^{-11} S/cm. After I_2 inclusion, the conductivity increased by 7 orders of magnitude to reach 2.16×10^{-4} S/cm. This dramatic change was attributed to the extended $\{Cu_4I_5\}$ layer formed by strong $I^-\cdots I_2\cdots I^-$ interactions, as seen from single-crystal X-ray diffraction (Figure 26). Notably, this work demonstrated reversible adsorption/desorption of I_2 and associated modulation of the conductivity.

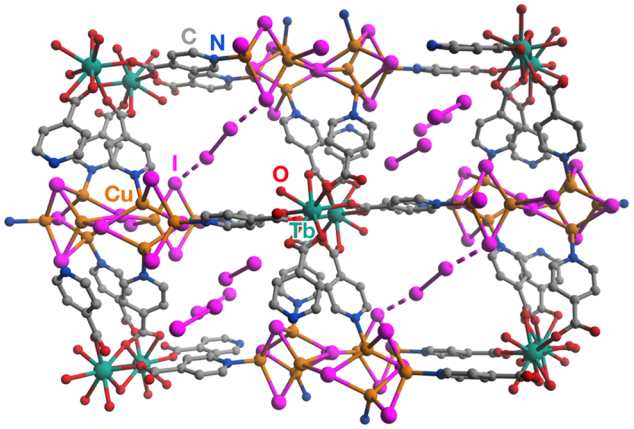

Figure 26. Structure of $Tb(Cu_4I_4)(PCA)_3$[246] containing crystallographically resolved I_2 guests with close $I^-\cdots I_2\cdots I^-$ contacts highlighted.

Another example of crystallographically resolved iodine inclusion is $Co_3(BDC)_3(bpz)_2{\cdot}0.5\,I_2$ (BDC = benzene-1,4-dicarboxylate, bpz = 3,3′,5,5′-tetramethyl-4,4′-bipyrazole), which contained I_2 in the channels.[242] While no evidence of the reduction of I_2 to iodide species by the framework was found, the conductivity nevertheless increased by 3 orders of magnitude to 1.56×10^{-6} S/cm upon introduction of I_2.

Zhang et al. found that iodine adsorption in the $V_2(OH)_2(BPTC)$ framework resulted in oxidation of about 30% of the native V^{III} centers to V^{IV}.[247] Powder and single-crystal X-ray diffraction analyses revealed the presence of both I_2 and I_3^- in the channels, forming a helical chain. The conductivity of the iodine-containing MOF increased to 1.2×10^{-4} S/cm from an original value of 1.7×10^{-10} S/cm. The authors attributed conductivity to both mixed-valent V centers and charge hopping along the iodine chains.

Other instances of iodine incorporation resulting in electrical conductivity have also been reported. Encapsulation of ∼17% iodine by weight into $Eu_4(BPT)_4$ (BPT = biphenyl-3,4′,5-tricarboxylate) yielded a conductivity of 8.27×10^{-7} S/cm (the conductivity of the parent material was not reported).[248] Uptake of I_2 and I_3^- by $Co_3(NDC)_3$ (NDC = 2,6-naphthalenedicarboxylate)[249] resulted in a conductivity of 1.88×10^{-6} S/cm for a thin film device.[250] Hall effect measurements were also carried out, yielding a hole mobility of 21.2 $cm^2\ V^{-1}\ s^{-1}$ and a carrier concentration of 5×10^{11} cm^{-3}. Hall effect measurements on films of CoBDC and CoNDC grown on TiO_2 and doped with I_2 showed similar mobility values of 21.2 and 87.6 $cm^2\ V^{-1}\ s^{-1}$, respectively.[251]

Finally, stoichiometric polyiodide incorporation also increased the conductivity of several tetrathiafulvalene-based MOFs, as discussed in more detail above.[87,198,207,209] In most cases, these changes were attributed to oxidation of the ligand core, although we note that transport through iodide channels may also play a role.

6.2. Organic and Organometallic Molecules

The *guest-promoted* approach is not limited to smaller inorganic species, as large organic molecules have also been incorporated in MOFs to increase their conductivity. Talin et al. reported that soaking thin films of $Cu_3(BTC)_2$ (or HKUST-1; BTC = benzene-1,3,5-tricarboxylate) in a saturated solution of TCNQ, an electron acceptor, increased its conductivity 6 orders of magnitude from 10^{-8} to 0.07 S/cm after 72 h.[235] The decrease in the BET surface area from 1844 to 214 m^2/g indicated that TCNQ was incorporated into the pores. The conductivities increased with longer exposure times in good agreement with percolation theory, leading the authors to propose that conducting regions were formed in the MOF by TCNQ bridging the copper paddlewheel SBUs (Figure 27). Vibrational and UV−vis spectroscopic data were consistent with partially reduced TCNQ, implying charge transfer between the framework and TCNQ.

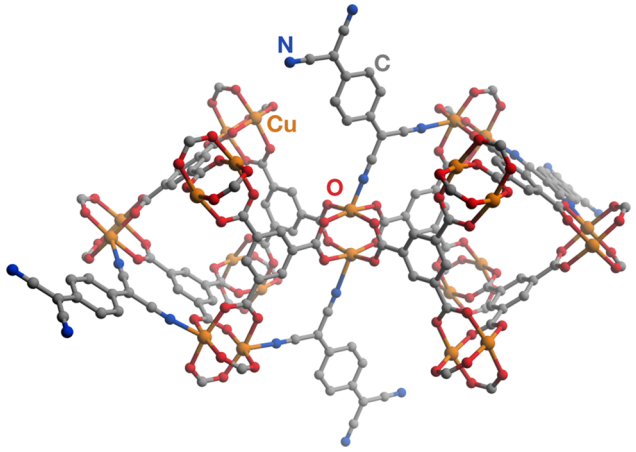

Figure 27. Predicted structure of TCNQ@$Cu_3(BTC)_2$ with TCNQ bridging the Cu^{II} paddlewheel clusters of the MOF to form a continuous charge transport pathway.[235,243]

Higher conductivities in TCNQ@$Cu_3(BTC)_2$ compared to the pristine MOF were corroborated by other reports.[243,252,253] However, Schneider et al.[243] and Thürmer et al.[254] showed that partial or full conversion of $Cu_3(BTC)_2$ into the dense coordination polymer Cu(TCNQ) ($\sigma \sim 0.1$ S/cm[82,255]) upon exposure to TCNQ proceeded under certain conditions. These works highlighted the importance of verifying the phase composition of MOFs after treatment with redox-active species and raise the question of whether the formation of a highly conductive parasitic phase contributes to the improved conductivity. Hence, additional investigation into the mechanism of conductivity enhancement in this system remains important.

TCNQ incorporation led to a 10^4-fold improvement in conductivity in $Cu_2(TATAB)_3$ (TATAB = 4,4′,4″-((1,3,5-

https://dx.doi.org/10.1021/acs.chemrev.9b00766
Chem. Rev. 2020, 120, 8536−8580

triazine-2,4,6-triyl)tris(azanediyl)) tribenzoate), a denser MOF-based on the same copper paddlewheel SBU.[256] Although the overall structure and metal environment in $Cu_2(TATAB)_3$ is similar to $Cu_3(BTC)_2$, the larger size of the linker leads to formation of an interpenetrated framework, with reduced porosity compared to $Cu_3(BTC)_2$. When reacted with a methanolic solution of TCNQ, $Cu_2(TATAB)_3$ darkened in color, and its conductivity increased from 9.75×10^{-12} to 2.67×10^{-7} S/cm, as determined from two-probe pressed pellet measurements. No discussion of the exact mechanism of TCNQ interactions with the framework was provided; however, the denser arrangement of the copper paddlewheels in the material makes it difficult to envision a bridging binding mode for the TCNQ, as was proposed for $Cu_3(BTC)_2$.

TCNQ incorporation was also reported to increase the conductance of thin-film MOF devices via charge transfer between TCNQ and the framework for both $Co_2(DOBDC)$[257] and a 2D MOF constructed of Cu^{II} acetate paddlewheels and a tetrapyridyl porphyrin linker.[258]

The effects of ferrocene doping on the conductivity of thin films of $Cu_3(BTC)_2$ have also been investigated.[259] Activated thin films of the MOF were exposed to ferrocene vapors, which led to a slight improvement of the electrical conductivity, from 1.47×10^{-15} to 3.57×10^{-15} S/cm. From the thickness dependence of the current density in the films, the authors concluded that the conduction mechanism was not tunneling through the films but rather hopping-type.

Guo et al. demonstrated that soaking films of a pillared paddlewheel MOF with an electron-rich pyridyl- and dipyrrolidyl-substituted naphthalene diimide (NDI) ligand in a solution of methyl viologen dication (MV^{2+}) increased the conductivity from 6×10^{-7} to 2×10^{-5} S/cm.[240] Soaking in solutions of the weaker π-acids dinitrotoluene and 1,5-difluoro-2,4-dinitrobenzene also improved the conductivity, though by less than one order of magnitude. In contrast, treatment with a solution of C_{60} resulted in unchanged conductivity, which was attributed to size exclusion by the MOF pores. The authors proposed that donor–acceptor interactions between the π-acid guests and the electron-rich ligand introduced charge carriers and potentially also increased the charge mobility via π–π interactions.

Yet larger redox-active guests have been incorporated in more porous frameworks. Goswami et al. reported that C_{60} uptake dramatically increased the conductivity of $Zr_6(OH)_{16}(TBAPy)_2$ (NU-901; TBAPy = tetrakis(*p*-benzoate) pyrene).[236] The conductivity of C_{60}@NU-901 was on the order of 10^{-3} S/cm, $\sim 10^{11}$ times higher than guest-free NU-901 ($<10^{-14}$ S/cm). A related study by Kung et al. reported the incorporation of an electron-deficient metallacarborane, nickel(IV) bis(dicarbollide) (NiCB), into a different polymorph of $Zr_6(OH)_{16}(TBAPy)_2$ known as NU-1000.[224] EIS yielded an estimated conductivity of 2.7×10^{-7} S/cm for NiCB@NU-1000. The value from a more conventional two-probe pressed pellet measurement was lower (4.3×10^{-9} S/cm) but still exceeded that of pristine NU-1000 (9.1×10^{-12} S/cm) by several orders of magnitude. UV–vis spectroscopy data for both of these guest@MOFs revealed charge transfer bands corresponding to donor–acceptor interactions between the guests and pyrene-based linkers, which ostensibly enhanced the conductivities. Notably, both NiCB@NU-1000 and C_{60}@NU-901 retained significant porosity, with BET surface areas of 1260 and 1550 m^2/g, respectively.

Souto et al. encapsulated C_{60} in a similarly mesoporous MOF with the formula $Fe_3O(TTFTB)_3$ (MUV-2) with a redox-active TTF-based ligand.[237] Similar to the pyrene-based MOFs, a charge transfer band in the UV–vis spectroscopy data indicated donor–acceptor interactions between C_{60} and the TTF core. While DFT calculations predicted favorable ligand-to-guest charge transfer and a lowered bandgap in the C_{60}-encapsulated material, the conductivity increase was modest (from 3.7×10^{-11} S/cm for MUV-2 to 4.7×10^{-9} S/cm for C_{60}@MUV-2). The authors attributed the relatively low conductivity value to low C_{60} loading (C_{60}@MUV-2 remained highly porous, with a BET surface area of 1040 m^2/g) and long distances separating the ligand TTF moieties.

C_{60} incorporation into thin films of surface-mounted metal–organic frameworks (SURMOFs) has also been demonstrated to increase their conductivities. Deposition of C_{60}@Cu(BPDC) (BPDC = biphenyl-4,4′-dicarboxylate) and C_{60}@Zn(TPP) (TPP = 5,15-bis(3,4,5-trimethoxyphenyl)-10,20-bis(4-carboxyphenyl)porphyrin) SURMOFs was carried out by spin-coating alternating layers of solutions of the metal salt, linker, and C_{60}.[260] The conductivities of the C_{60}-containing frameworks ($\sim 10^{-11}$ S/cm) were at least 2 orders of magnitude higher than the pristine SURMOFs ($<2 \times 10^{-13}$ S/cm). For C_{60}@Zn(TPP), a C_{60} loading of about 0.9 molecules per unit cell was assigned based on UV–vis spectroscopy and mass spectrometry. C_{60}@Zn(TPP) also exhibited photoconductivity, reaching a maximum conductivity of 1.3×10^{-9} S/cm when irradiated with 455 nm light. No surface area measurements were carried out on these materials.

6.3. Conductive Polymers and Oxides

Conductive extended solids—both organic and inorganic—have been encapsulated in MOFs. For polymer⊃MOF assemblies, conductivities higher than either of the pristine components have been reported. Enhanced transport properties in polymer⊃MOF materials have been generally attributed to charge transfer interactions between polymer chains surrounded by π-donor ligands, as well as high degrees of order and orientation in the polymers. In situ hole doping of the polymers by I_2 during the polymerization process are also likely to play a role.

Polymer chains have been incorporated into MOFs by loading monomers into the channels and then reacting the material with I_2 to induce polymerization. Wang et al. first demonstrated this approach with polypyrrole (PPy) and $Zn_3(lac)_2(pybz)_2$,[261] likely inspired by an earlier work,[262] in which well-ordered polypyrrole was grown inside a layered coordination polymer. The resulting PPy⊃$Zn_3(lac)_2(pybz)_2$ material (Figure 28) reached a conductivity of 1.0×10^{-2} S/cm, higher than both I_2@$Zn_3(lac)_2(pybz)_2$ (3.42×10^{-3} S/cm),[244] and bulk PPy synthesized by the same group in similar conditions to the MOF loading procedure ($\sim 10^{-5}$ S/cm). (Much higher values for the conductivity of PPy have been obtained with different synthetic procedures.[263]) Interestingly, PPy extracted from the MOF showed significantly higher conductivity compared to the bulk powder. Dhara et al. obtained PPy⊃$Cd_2(NDC)(PCA)_2$ (NDC = 2,6-napthalenedicarboxylate, PCA = 4-pyridinecarboxylate) using the same strategy,[264] resulting in a 10^9-fold increase in conductivity to $\sim 10^{-3}$ S/cm (via I–V measurements). From Hall effect measurements, a higher conductivity of 0.2 S/cm was estimated, along with an electron mobility of 8.15 $cm^2\ V^{-1}\ s^{-1}$ and electron density of 1.50×10^{17} cm^{-3}.

https://dx.doi.org/10.1021/acs.chemrev.9b00766
Chem. Rev. 2020, 120, 8536–8580

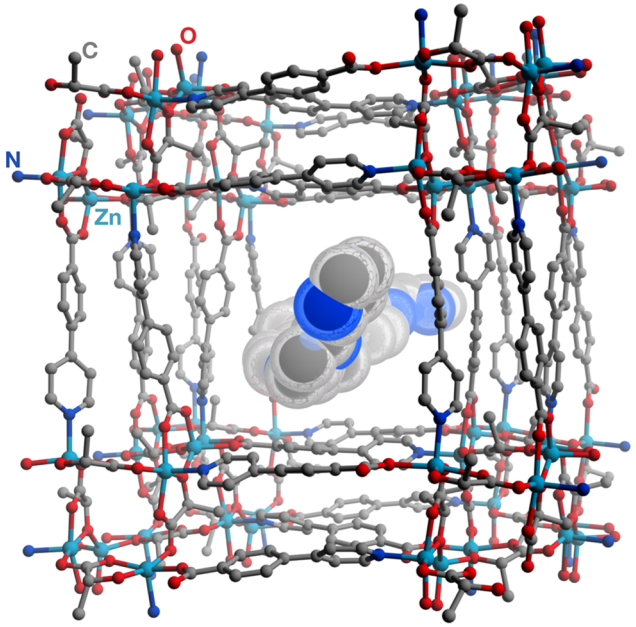

Figure 28. Illustration of a chain of polypyrrole occupying the pore volume of $Zn_3(lac)_2(pybz)_2$.[244,261]

Jiang et al. investigated co-incorporation of both PPy and elemental sulfur into a number of highly porous MOFs for potential applications in lithium−sulfur batteries.[215] The MOFs $Cr_3OF(BDC)_3$ (Cr-MIL-101), Al(OH)(BDC) (Al-MIL-53), and $[Zr_6(OH)_{16}]_2(TCPP)_3$ (PCN-224; TCPP = 5,10,15,20-(4-carboxyphenyl)porphyrin) were first loaded with sulfur by heating the activated materials in a sealed tube together with powdered sulfur. Then, the sulfur-loaded frameworks were put into a solution of pyrrole to which Fe^{III} was added to induce polymerization. This resulted in overall compositions of roughly 1:1:1 S:PPy:MOF for Cr-MIL-101 and Al-MIL-53, and roughly 2:1:1 S:PPy:MOF. While loading with sulfur slightly decreased the electrical conductivities of the three MOFs (from $\sim 10^{-7}$ to $\sim 10^{-9}$ S/cm), incorporation of polypyrrole caused dramatic increases in conductivity (0.113−2.71 S/cm). That said, these values are similar to polypyrrole grown on sulfur in the same study (1.73 S/cm).

Le Ouay et al. incorporated poly(3,4-ethylenedioxythiophene) (PEDOT) into Cr-MIL-101.[238] The conductivity of the PEDOT⊃Cr-MIL-101 material with 57% polymer loading by weight was 1.1×10^{-3} S/cm (compared to $<10^{-11}$ S/cm for Cr-MIL-101 alone). This material had a BET surface area of 803 m^2/g, partially retaining the high porosity of the Cr-MIL-101 host. The mass fraction of PEDOT in Cr-MIL-101 was found to correlate directly with the conductivity and inversely with the surface area. Interestingly, when PEDOT was incorporated into La(BTC), a MOF with 1D channels, the composite showed a much smaller increase in conductivity than PEDOT⊃Cr-MIL-101, reaching only 2.3×10^{-8} S/cm. The authors hypothesized that the 3D architecture of Cr-MIL-101 may enable higher conductivity by allowing for more PEDOT interchain interactions.

Motivated by the ubiquitous conductive tin oxide glasses, Kung et al. investigated the modification of $Zr_6(OH)_{16}(TBAPy)_2$ (NU-1000) with postsynthetically installed tetratin(IV) oxy clusters.[239] The activated MOF was immersed in a solution of a tin precursor, which readily hydrolyzed at the hydroxyl and aqua sites of the Zr cluster. The material was then subjected to a steam treatment, and this whole process was repeated several times. The authors found that the unmodified MOF, as well as the same MOF after one or two cycles of the installation process (in which the concentration of the installed clusters was low enough to give isolated tin(IV) oxy clusters), were both insulating. However, after three cycles, the clusters formed continuous strands of tin(IV) oxide, leading to a significant improvement in conductivity, with values as high as 1.8×10^{-7} S/cm. Despite the considerable amount of tin(IV) oxide in the material, it was still porous, with BET surface areas of 680 m^2/g. This study demonstrated that conductive MOFs can be attained through the guest-promoted design strategy using extended inorganic solids, in addition to the more commonly utilized organic and organometallic molecules and polymers.

7. CONCLUSIONS AND OUTLOOK

Recent years have witnessed a broad diversification of strategies used to imbue MOFs with mobile charge carriers and pathways for charge transport. These strategies have centered upon various intrinsic structural components of MOFs, including the inorganic SBU, extended bonding between the metal and linker, and noncovalent interactions among linkers. Additionally, the porosity of MOFs has been leveraged to introduce extrinsic guests that mediate conductivity. Across these distinct approaches, we summarize unifying characteristics among the materials we have discussed:

(1) *The ubiquity of mixed-valence motifs.* Mixed valency among metal centers or linkers can both introduce charge carriers into MOFs. For example, frameworks containing $Fe^{II/III}$ in chain SBUs are more conductive than those containing only divalent metals. Semiquinonate MOFs (and their imino- and thio-analogs) contain both radical and closed-shell oxidation states of the linkers in the solid state. Conductive MOFs based on tetrathiafulvalene and other conjugated organic molecules also contain a mixture of the radical cation and neutral forms of the organic cores. Some of these materials are grown with a mixture of ligand oxidation states (often with the presence of atmospheric oxygen serving as an in situ oxidant) and contain intrinsic mixed-valency in their as-synthesized forms. In other cases, mixed-valent motifs are postsynthetically introduced (e.g., deliberate oxidation of Fe^{II} centers to Fe^{III}, reduction of Fe^{III} to Fe^{II}, or partial oxidation of tetrathiafulvalene to its radical cation form using I_2). Materials in which the concentration of different charge states can be tuned have generally exhibited conductivities correlating with the extent of mixed-valency.

(2) *The presence of continuous charge transport pathways.* Regardless of whether conduction proceeds by charge hopping or band conduction mechanisms, close proximity of the sites that charges can occupy correlates with conductivity. Moreover, continuous arrangement of these sites throughout the structure of the material is important to enable long-range charge transport. Continuous 1D, 2D, and 3D covalently bonded motifs have been demonstrated to facilitate conductivity in MOFs. In addition, in frameworks containing extensive $\pi-\pi$ stacking, closer contact distances throughout the stack are correlated with higher conductivities.

https://dx.doi.org/10.1021/acs.chemrev.9b00766
Chem. Rev. 2020, 120, 8536−8580

Table 9. Charge Mobility Values of Metal−Organic Frameworks

material[a]	description	μ (cm^2 V^{-1} s^{-1})	method	carrier type	ref
		through-bond			
$Fe_2(BDP)_3$		0.02	FP-TRMC		69
$K_{0.8}Fe_2(BDP)_3$	red. ($K^+[C_{10}H_8]^{\bullet-}$)	0.29	FP-TRMC		69
$K_{0.98}Fe_2(BDP)_3$	red. ($K^+[C_{10}H_8]^{\bullet-}$)	0.84	FET	*e*	69
Mn_2(DSBDC)	MeOH-exchanged	0.02	FP-TRMC		67
	act.	0.01	FP-TRMC		67
		extended conjugation			
Cu_3(BHT)		99	FET	*h*	76
		116	FET	*e*	76
$Fe_3(THT)_2(NH_4)_3$		125(9)	TRTS		78
		211(7)	TRTS		78
		229(33)	Hall		78
Ni_3(HITP)$_2$		48.6	FET	*h*	190
		45.4	FET	*h*	197
		through-space			
[In(isophthalate)$_2$]		4.6×10^{-3}	FET		211
Zn_2(TTFTB)		0.2	FP-TRMC		37
		hopping			
Zn(H_2DPPDB)		$3-4 \times 10^{-3}$	FP-TRMC		228
Zn[Pd(DPPDB)]		2×10^{-3}	FP-TRMC		228
		guest-promoted			
Co(BDC)	I_2-doped	21.2	Hall (film on TiO_2/FTO)	*h*	251
$Co_3(NDC)_3$	I_2-doped	87.6	Hall (film on TiO_2/FTO)	*h*	251
$Co_3(NDC)_3$	I_2-doped	21.2	Hall (film on TiO_2/FTO)	*h*	250

[a]See Abbreviations.

(3) *The inherent chemical tunability of MOFs and resulting control over transport properties.* Harnessing the modular nature of MOFs, comparative studies have begun to systematically change the identities of the metal and ligands to compare their effects on the resulting transport properties. Additional framework compositions are accessible through a combination of de novo synthesis and postsynthetic modification strategies. Routes to control $\pi-\pi$ stacking motifs, as well as the connectivity and dimensionality of the frameworks, have also been demonstrated to correlate with conductivities. Finally, harnessing the inherent porosity of MOFs toward guest-promoted conductivity opens up the door to near-endless host−guest combinations with different properties.

This field has seen immense growth and progress in the past five years, allowing for the relationships among structure, composition, and physical properties discussed in this Review to be established from existing studies. Nevertheless, many worthwhile directions remain to be pursued in terms of both fundamental studies and potential applications of conductive MOFs. We highlight some of the most intriguing questions and pressing challenges:

(1) *Disentangling the properties of charge carriers in MOFs.* Only a handful of charge mobility values have been reported for MOFs (Table 9), and many of these studies have used noncontact methods, such as FP-TRMC and TRTS. Hall effect measurements and FET devices using high-quality thin films or ideally single crystals of MOFs can determine the nature of the charge carriers (i.e., electrons or holes), as well as the carrier concentration and mobility. In general, deeper investigations into the mechanisms underlying high conductivities will yield more useful insights than a race toward record conductivity values. Additionally, computational studies (e.g., band structure calculations) will be important in corroborating experimental findings in this area.

(2) *Realizing more examples of isotropic conduction pathways in MOFs.* The majority of conductive MOFs have anisotropic structures. For most MOFs with through-bond and through-space conduction pathways, charge transport dominates in a single crystallographic direction. For MOFs displaying extended conjugation, even though both in-plane and out-of-plane directions are expected to contribute to conductivity, different relative contributions may still result in anisotropic character in the bulk transport. Only isolated examples of conductive MOFs with isotropic structures and crystallographically resolved transport pathways have been reported.[68,71,72,153] The problem of installing charge carriers in close proximity to one another in an isotropic, porous network presents an intriguing intellectual and synthetic challenge. On the practical side, isotropic materials should offer some advantages for integration into devices on account of their orientation-independent properties.

(3) *Conductivity in mixed-metal and mixed-linker systems.* Apart from mixed-valent motifs, targeting MOFs with more than one metal or ligand can be a strategy to dope these materials and increase their conductivities. Such systems could conceivably be realized through either direct synthesis or postsynthetic cation- or ligand-exchange.[265,266] Preliminary examples of mixed-metal approaches[191,220,229,267] portend promising capabilities to further tune the conductivity of MOFs through compositional variation.

(4) *Further elucidation of transport mechanisms responsible for excellent bulk conductivities in selected 2D MOFs, especially*

https://dx.doi.org/10.1021/acs.chemrev.9b00766
Chem. Rev. 2020, 120, 8536−8580

$Ni_3(HITP)_2$. Very recent single-crystal transport studies on materials with triphenylene-based linkers (namely, $Ni_3(HITP)_2$ and $Cu_3(HOTP)_2$) have indicated that the in-plane conductivities are similar in magnitude to the cross-plane conductivities.[79] These findings suggest that $\pi-\pi$ stacking interactions between the layers may play an important role in determining the bulk transport properties of these materials. In addition to more characterization of high-quality single crystals, unambiguously determining the crystal structures, stacking motifs, and metal and linker oxidation states in these materials can address this question. Finally, studies that systematically vary the identities of the metal and ligand and examine the resulting conductivities may offer further insights.

(5) *Isolation and characterization of single layers of 2D MOFs.* Several theoretical works have predicted monolayers of 2D MOFs with extended conjugation to be materials with topologically nontrivial electronic states.[31−36] Although exfoliation down to single layers has been demonstrated for nonporous 2D coordination polymers that are conductive,[268] the transport properties of isolated mono- or few-layer samples of 2D MOFs with extended π−d conjugation have not been reported in detail. The realization of such materials could reveal new platforms for studying transport phenomena at the forefront of experimental physics research. On a related note, further dimensional reduction of the motifs that facilitate charge transport in MOFs to 1D and 0D structures can shed light on specific coupling mechanisms.[269]

(6) *Expanding the library of ligands for MOFs featuring through-space charge transport pathways.* To date, most conductive MOFs with transport pathways comprising $\pi-\pi$ stacking are made with TTF-based ligands. Though a large variety of different donor and acceptor molecules are utilized in organic electronics, most of these have not yet been incorporated into MOFs. Clever ligand designs that overcome synthetic hurdles that may be encountered in using such molecules can lead to new MOFs with through-space charge transport pathways and potentially notable photophysical properties.

(7) *More detailed structural investigations of host−guest interactions in MOFs.* In MOFs with guest-promoted conductivities, the locations of most guest species within the pores of the MOF have not been crystallographically resolved. Determining the nature of charge-transfer interactions that increase conductivity in such systems would benefit from crystallographic investigation. Additionally, side reactivity between the guest and framework decomposition products is a potential concern in some of these systems. More in-depth structural studies (e.g., Rietveld refinement for crystalline powders, pair distribution function analysis for less crystalline materials) can also allow for more definitive assignment of enhanced transport properties to the host−guest composite versus conductive side products.

(8) *Influence of environment and atmosphere on MOF conductivity values.* The successful application of conductive MOFs to chemiresistive sensing is a consequence of the sensitivity of the electronic properties of these materials to the atmosphere in which they are measured. Both reversible and irreversible changes in conductivity of MOFs may be observed upon exposure to different atmosphere (e.g., oxygen, moisture, volatile organic compounds, corrosive vapors). While such responses have been productively harnessed toward tunable conductivities and sensing applications, unmonitored atmospheric effects may also influence reported conductivity values. Hence, controlling and purposefully studying the impact of environmental effects can lead to more reproducible values in the literature and new materials for chemiresistive sensing.

(9) *Best practices for materials preparation and measurement techniques.* As a corollary to the previous point, depending on the material and use case, the standard (or ideal) conditions under which to measure the transport characteristics of a MOF may vary. In addition, the same material (nominally, in terms of structure and composition) prepared under different conditions or measured in different form factors may exhibit conductivity values varying over several orders of magnitude. To maintain clarity in this growing field and ensure reproducibility, we believe it is increasingly important for researchers to document their sample and device preparation procedures, as well as the details of the measurement conditions (e.g., temperature, atmosphere, illumination, nature of the electrical contacts, as well as details on the measurement apparatus).[56] In addition, reporting the temperature dependence of the conductivity (from which an activation energy and transport mechanism can be extracted) is more instructive than the room temperature value alone.

We note in closing that conductivity values relevant to real-world applications have already been attained in MOFs. Inventive synthetic approaches, optimized growth techniques, and improved device fabrication can (and should) all continue to raise the ceiling of the transport properties attainable in porous, crystalline framework materials. However, equally important are the continuing refinement of design principles and more detailed mechanistic investigations into charge transport in MOFs. Future work along these lines will undoubtedly reveal novel fundamental properties and opportunities for application for this versatile class of materials.

AUTHOR INFORMATION

Corresponding Author

Mircea Dincă − *Department of Chemistry, Massachusetts Institute of Technology, Cambridge, Massachusetts 02139, United States;* orcid.org/0000-0002-1262-1264; Email: mdinca@mit.edu

Authors

Lilia S. Xie − *Department of Chemistry, Massachusetts Institute of Technology, Cambridge, Massachusetts 02139, United States*

Grigorii Skorupskii − *Department of Chemistry, Massachusetts Institute of Technology, Cambridge, Massachusetts 02139, United States*

Complete contact information is available at: https://pubs.acs.org/10.1021/acs.chemrev.9b00766

Author Contributions

†L.S.X. and G.S. contributed equally to this work.

https://dx.doi.org/10.1021/acs.chemrev.9b00766
Chem. Rev. 2020, 120, 8536−8580

Notes

The authors declare no competing financial interest.

Biographies

Lilia S. Xie is a Ph.D. student and an NSF Graduate Research Fellow in Mircea Dincă's group at MIT. Her current research focuses on electrically conductive metal−organic frameworks with through-space charge transport pathways. She received her A.B. in chemistry in 2014 from Princeton University, where she worked with Robert Cava on the crystal growth of topological semimetals and superconductors.

Grigorii Skorupskii is a Ph.D. student in Mircea Dincă's group at MIT. His research focuses on charge transport in metal−organic frameworks with extended conjugation conductivity pathways. He received his B.Sc. in materials science in 2015 from Moscow State University where he worked on metal-ion battery electrode materials.

Mircea Dincă is a Professor in the Department of Chemistry at MIT. His group's research is broadly focused on understanding and changing materials' physical and chemical properties through means that are not typically applicable to solids. He also gets excited about making new materials that combine canonically antithetical properties, such as porosity and electrical transport, to yield something that is greater than the sum of its parts. Educated at Princeton University (A.B. in Chemistry, 2003) and UC Berkeley (PhD in Inorganic Chemistry, 2008), he aspires to one day create and control (chemical) disorder.

ACKNOWLEDGMENTS

We are thankful for generous support on primary research for various aspects of electrically conductive MOFs from the Army Research Office (W911NF-17-1-0174) and the Department of Energy, Office of Science, Office of Basic Energy Sciences (DE-SC0018235). L.S.X. thanks the National Science Foundation for support through the Graduate Research Fellowship Program (1122374). We are grateful to Prof. Christopher Hendon for helpful discussions and providing graphics of electronic band structures.

ABBREVIATIONS

1,2,4-BTC	benzene-1,2,4-tricarboxylate
1D	one-dimensional
2D	two-dimensional
3-bpd	1,4-bis(3-pyridyl)-2,3-diaza-1,3-butadiene
3D	three-dimensional
4-bpd	1,4-bis(4-pyridyl)-2,3-diaza-1,3-butadiene
act.	activated (all solvent removed)
AnBEB	4,4′-(anthracene-9,10-diylbis(ethyne-2,1-diyl))-dibenzoate
AnBHB	4,4′-(anthracene-9,10-diyl)bis(2-hydroxybenzoate)
azbpy	trans-4,4′-azobispyridine
BCMTC	4,4′-(cyclopent-1-ene-1,2-diyl)bis(5-methylthiophene-2-carboxylate)
BDC	benzene-1,4-dicarboxylate
BDP	benzene-1,4-dipyrazolate
BDT	benzene-1,4-ditetrazolate
BET (SA)	Brunauer−Emmett−Teller (surface area)
BHC	benzenehexacarboxylate
BHSe	benzenehexaselenolate
BHT	benzenehexathiolate
BPDC	biphenyl-4,4′-dicarboxylate
BPDPNDI	*N*,*N*′-bis(4-pyridyl)-2,6-dipyrrolidyl-1,4,5,8-naphthalenetetracarboxydiimide
BPMTC	bis(5-pyridyl-2-methyl-3-thienyl)cyclopentane
BPT	biphenyl-3,4′,5-tricarboxylate
BPTC	biphenyl-3,3′,5,5′-tetracarboxylate
bpz	3,3′,5,5′-tetramethyl-4,4′-bipyrazole
Br_2dhbq	2,5-dibromo-3,6-dihydroxo-1,4-benzoquinone
BTC	benzene-1,3,5-tricarboxylate
BTDD	bis(1*H*-1,2,3-triazolo[4,5-*b*],[4,′5′-i]dibenzo[1,4]-dioxin
Cl_2dhbq	2,5-dichloro-3,6-dihydroxo-1,4-benzoquinone
Cp_2Co	cobaltocene
DAPV	di(3-diaminopropyl)-viologen
dca	dicyanamide
desolv.	desolvated (pore solvents removed)
DFDNB	1,5-difluoro-2,4-dinitrobenzene
DFT	density functional theory
dhbq	2,5-dihydroxy-1,4-benzoquinone
DNT	dinitrotoluene
DOBDC	2,5-dioxybenzene-1,4-dicarboxylate
DPNDI	*N*,*N*′-di(4-pyridyl)-1,4,5,8-naphthalenetetracarboxydiimide
DSBDC	2,5-disulfidobenzene-1,4-dicarboxylate
E_a	activation energy
EIS	electrochemical impedance spectroscopy
EMIM	1-ethyl-3-methylimidazolium
EPR	electron paramagnetic resonance
FET	field-effect transistor
FP-TRMC	flash photolysis time-resolved microwave conductivity
glu	glutarate
H_2DPPDB	free base 4,4′-(10,20-diphenylporphyrin-5,15-diyl)dibenzoate
HIB	hexaiminobenzene
HIP	5-hydroxyisophthalate
HITP	2,3,6,7,10,11-hexaiminotriphenylene
Hmna	6-mercaptonicotinic acid
HOB	hexaoxybenzene
HOTP	2,3,6,7,10,11-hexaoxytriphenylene
IPc	2,3,9,10,16,17,23,24-octaiminophthalocyanine
IR	infrared
lac	lactate
Me_2BPDC	2,2′-dimethylbiphenyl-4,4′-dicarboxylate
mglu	methylglutarate
MOF	metal−organic framework
msuc	methylsuccinate
MV^{2+}	methyl viologen (1,1′-dimethyl-4,4′-bipyridinium)
NDC	2,6-naphthalenedicarboxylate
NiCB	nickel(IV) bis(dicarbollide)
ntca	1,4,5,8-naphthalenetetracarboxylate
ONPc	3,4,12,13,21,22,30,31-octaoxynaphthalocyanine
OPc	2,3,9,10,16,17,23,24-octaoxyphthalocyanine
ox.	oxidized
PCA	4-pyridinecarboxylate
pdt	2,3-pyrazinedithiolene
PEDOT	poly(3,4-ethylenedioxythiophene)
PES	photoelectron spectroscopy
phz	phenazine
PTC	perthiolated coronene
PXRD	powder X-ray diffraction
pybz	4-(pyridin-4-yl)benzoate
pyz	pyrazine
red.	reduced

https://dx.doi.org/10.1021/acs.chemrev.9b00766
Chem. Rev. 2020, 120, 8536−8580

sc	single crystal
SDC	stilbene-4,4′-dicarboxylate
SEM	scanning electron microscopy
SIP	5-sulfoisophthalate
solv.	solvated
suc	succinate
TABTT	1,3,5-triaminobenzene-2,4,6-trithiol
TATAB	4,4′,4″-((1,3,5-triazine-2,4,6-triyl)tris(azane diyl)) tribenzoate
TBAPy	tetrakis(p-benzoate) pyrene
TCNQ	tetracyanoquinodimethane
TCPB	1,2,4,5-tetrakis(4-carboxyphenyl)benzene
TCPP	5,10,15,20-(4-carboxyphenyl)porphyrin
TEM	transmission electron microscopy
$Th^{\bullet+}BF_4^-$	thianthrene tetrafluoroborate
THQ	tetrahydroxy-1,4-quinone
THT	triphenylene-2,3,6,7,10,11-hexathiolate
TPDAP	2,5,8-tri(4-pyridyl)1,3-diazaphenalene
TPP	5,15-bis(3,4,5-trimethoxyphenyl)-10,20-bis(4-carboxyphenyl)porphyrin
TPyP	5,10,15,20-tetra-4-pyridyl-porphyrin
TRTS	time-resolved terahertz spectroscopy
TTF	tetrathiafulvalene
$TTF(py)_4$	tetrathiafulvalene tetrapyridyl
TTFTB	tetrathiafulvalene tetrabenzoate
UV−vis	ultraviolet−visible
vac.	under vacuum
vdP	van der Pauw
VRH	variable range hopping
XPS	X-ray photoelectron spectroscopy
μ	carrier mobility (e = electron mobility, h = hole mobility)
σ	conductivity

REFERENCES

(1) James, S. L. Metal-Organic Frameworks. *Chem. Soc. Rev.* **2003**, *32*, 276.

(2) Rowsell, J. L. C.; Yaghi, O. M. Metal-Organic Frameworks: A New Class of Porous Materials. *Microporous Mesoporous Mater.* **2004**, *73*, 3−14.

(3) Furukawa, H.; Cordova, K. E.; O'Keeffe, M.; Yaghi, O. M. The Chemistry and Applications of Metal-Organic Frameworks. *Science* **2013**, *341*, 1230444.

(4) Murray, L. J.; Dincă, M.; Long, J. R. Hydrogen Storage in Metal-Organic Frameworks. *Chem. Soc. Rev.* **2009**, *38*, 1294−1314.

(5) Suh, M. P.; Park, H. J.; Prasad, T. K.; Lim, D.-W. Hydrogen Storage in Metal−Organic Frameworks. *Chem. Rev.* **2012**, *112*, 782−835.

(6) Sumida, K.; Rogow, D. L.; Mason, J. A.; McDonald, T. M.; Bloch, E. D.; Herm, Z. R.; Bae, T.-H.; Long, J. R. Carbon Dioxide Capture in Metal−Organic Frameworks. *Chem. Rev.* **2012**, *112*, 724−781.

(7) Mason, J. A.; Veenstra, M.; Long, J. R. Evaluating Metal−Organic Frameworks for Natural Gas Storage. *Chem. Sci.* **2014**, *5*, 32−51.

(8) Li, J.-R.; Kuppler, R. J.; Zhou, H.-C. Selective Gas Adsorption and Separation in Metal-Organic Frameworks. *Chem. Soc. Rev.* **2009**, *38*, 1477−1504.

(9) Li, J.-R.; Sculley, J.; Zhou, H.-C. Metal−Organic Frameworks for Separations. *Chem. Rev.* **2012**, *112*, 869−932.

(10) Herm, Z. R.; Bloch, E. D.; Long, J. R. Hydrocarbon Separations in Metal-Organic Frameworks. *Chem. Mater.* **2014**, *26*, 323−338.

(11) Adil, K.; Belmabkhout, Y.; Pillai, R. S.; Cadiau, A.; Bhatt, P. M.; Assen, A. H.; Maurin, G.; Eddaoudi, M. Gas/Vapour Separation Using Ultra-Microporous Metal−Organic Frameworks: Insights into the Structure/Separation Relationship. *Chem. Soc. Rev.* **2017**, *46*, 3402−3430.

(12) Ma, L.; Abney, C.; Lin, W. Enantioselective Catalysis with Homochiral Metal-Organic Frameworks. *Chem. Soc. Rev.* **2009**, *38*, 1248−1256.

(13) Lee, J.; Farha, O. K.; Roberts, J.; Scheidt, K. A.; Nguyen, S. T.; Hupp, J. T. Metal-Organic Framework Materials as Catalysts. *Chem. Soc. Rev.* **2009**, *38*, 1450−1459.

(14) Corma, A.; García, H.; Llabrés i Xamena, F. X. Engineering Metal Organic Frameworks for Heterogeneous Catalysis. *Chem. Rev.* **2010**, *110*, 4606−4655.

(15) Yang, D.; Gates, B. C. Catalysis by Metal Organic Frameworks: Perspective and Suggestions for Future Research. *ACS Catal.* **2019**, *9*, 1779−1798.

(16) Clough, A. J.; Yoo, J. W.; Mecklenburg, M. H.; Marinescu, S. C. Two-Dimensional Metal−Organic Surfaces for Efficient Hydrogen Evolution from Water. *J. Am. Chem. Soc.* **2015**, *137*, 118−121.

(17) Miner, E. M.; Fukushima, T.; Sheberla, D.; Sun, L.; Surendranath, Y.; Dincă, M. Electrochemical Oxygen Reduction Catalysed by Ni_3(Hexaiminotriphenylene)$_2$. *Nat. Commun.* **2016**, *7*, 10942.

(18) Dong, R.; Zheng, Z.; Tranca, D. C.; Zhang, J.; Chandrasekhar, N.; Liu, S.; Zhuang, X.; Seifert, G.; Feng, X. Immobilizing Molecular Metal Dithiolene−Diamine Complexes on 2D Metal−Organic Frameworks for Electrocatalytic H_2 Production. *Chem. - Eur. J.* **2017**, *23*, 2255−2260.

(19) Downes, C. A.; Clough, A. J.; Chen, K.; Yoo, J. W.; Marinescu, S. C. Evaluation of the H_2 Evolving Activity of Benzenehexathiolate Coordination Frameworks and the Effect of Film Thickness on H 2 Production. *ACS Appl. Mater. Interfaces* **2018**, *10*, 1719−1727.

(20) Miner, E. M.; Wang, L.; Dincă, M. Modular O_2 Electroreduction Activity in Triphenylene-Based Metal-Organic Frameworks. *Chem. Sci.* **2018**, *9*, 6286−6291.

(21) Campbell, M. G.; Sheberla, D.; Liu, S. F.; Swager, T. M.; Dincă, M. Cu_3(Hexaiminotriphenylene)^2: An Electrically Conductive 2D Metal-Organic Framework for Chemiresistive Sensing. *Angew. Chem., Int. Ed.* **2015**, *54*, 4349−4352.

(22) Campbell, M. G.; Liu, S. F.; Swager, T. M.; Dincă, M. Chemiresistive Sensor Arrays from Conductive 2D Metal-Organic Frameworks. *J. Am. Chem. Soc.* **2015**, *137*, 13780−13783.

(23) Smith, M. K.; Mirica, K. A. Self-Organized Frameworks on Textiles (SOFT): Conductive Fabrics for Simultaneous Sensing, Capture, and Filtration of Gases. *J. Am. Chem. Soc.* **2017**, *139*, 16759−16767.

(24) Rubio-Gimenez, V.; Almora-Barrios, N.; Escorcia-Ariza, G.; Galbiati, M.; Sessolo, M.; Tatay, S.; Marti-Gastaldo, C. Origin of the Chemiresistive Response of Ultrathin Films of Conductive Metal-Organic Frameworks. *Angew. Chem., Int. Ed.* **2018**, *57*, 15086−15090.

(25) Meng, Z.; Aykanat, A.; Mirica, K. A. Welding Metallophthalocyanines into Bimetallic Molecular Meshes for Ultrasensitive, Low-Power Chemiresistive Detection of Gases. *J. Am. Chem. Soc.* **2019**, *141*, 2046−2053.

(26) Aubrey, M. L.; Kapelewski, M. T.; Melville, J. F.; Oktawiec, J.; Presti, D.; Gagliardi, L.; Long, J. R. Chemiresistive Detection of Gaseous Hydrocarbons and Interrogation of Charge Transport in Cu[Ni(2,3-Pyrazinedithiolate)$_2$] by Gas Adsorption. *J. Am. Chem. Soc.* **2019**, *141*, 5005−5013.

(27) Sheberla, D.; Bachman, J. C.; Elias, J. S.; Sun, C.-J.; Shao-Horn, Y.; Dinca, M. Conductive MOF Electrodes for Stable Supercapacitors with High Areal Capacitance. *Nat. Mater.* **2017**, *16*, 220−224.

(28) Park, J.; Lee, M.; Feng, D.; Huang, Z.; Hinckley, A. C.; Yakovenko, A.; Zou, X.; Cui, Y.; Bao, Z. Stabilization of Hexaaminobenzene in a 2D Conductive Metal-Organic Framework for High Power Sodium Storage. *J. Am. Chem. Soc.* **2018**, *140*, 10315−10323.

(29) Feng, D.; Lei, T.; Lukatskaya, M. R.; Park, J.; Huang, Z.; Lee, M.; Shaw, L.; Chen, S.; Yakovenko, A. A.; Kulkarni, A.; et al. Robust and Conductive Two-Dimensional Metal-Organic Frameworks with

https://dx.doi.org/10.1021/acs.chemrev.9b00766
Chem. Rev. 2020, 120, 8536−8580

Exceptionally High Volumetric and Areal Capacitance. *Nat. Energy* **2018**, *3*, 30−36.
(30) Shinde, S. S.; Lee, C. H.; Jung, J.-Y.; Wagh, N. K.; Kim, S.-H.; Kim, D.-H.; Lin, C.; Lee, S. U.; Lee, J.-H. Unveiling Dual-Linkage 3D Hexaiminobenzene Metal-Organic Frameworks towards Long-Lasting Advanced Reversible Zn-Air Batteries. *Energy Environ. Sci.* **2019**, *12*, 727−738.
(31) Wang, Z. F.; Su, N.; Liu, F. Prediction of a Two-Dimensional Organic Topological Insulator. *Nano Lett.* **2013**, *13*, 2842−2845.
(32) Dong, L.; Kim, Y.; Er, D.; Rappe, A. M.; Shenoy, V. B. Two-Dimensional π-Conjugated Covalent-Organic Frameworks as Quantum Anomalous Hall Topological Insulators. *Phys. Rev. Lett.* **2016**, *116*, 096601.
(33) Yamada, M. G.; Soejima, T.; Tsuji, N.; Hirai, D.; Dincă, M.; Aoki, H. First-Principles Design of a Half-Filled Flat Band of the Kagome Lattice in Two-Dimensional Metal-Organic Frameworks. *Phys. Rev. B: Condens. Matter Mater. Phys.* **2016**, *94*, 081102.
(34) Chakravarty, C.; Mandal, B.; Sarkar, P. Bis(Dithioline)-Based Metal−Organic Frameworks with Superior Electronic and Magnetic Properties: Spin Frustration to Spintronics and Gas Sensing. *J. Phys. Chem. C* **2016**, *120*, 28307−28319.
(35) Li, W.; Sun, L.; Qi, J.; Jarillo-Herrero, P.; Dincă, M.; Li, J. High Temperature Ferromagnetism in π-Conjugated Two-Dimensional Metal−Organic Frameworks. *Chem. Sci.* **2017**, *8*, 2859−2867.
(36) Wu, M.; Wang, Z.; Liu, J.; Li, W.; Fu, H.; Sun, L.; Liu, X.; Pan, M.; Weng, H.; Dincă, M.; et al. Conetronics in 2D Metal-Organic Frameworks: Double/Half Dirac Cones and Quantum Anomalous Hall Effect. *2D Mater.* **2017**, *4*, 015015.
(37) Narayan, T. C.; Miyakai, T.; Seki, S.; Dincă, M. High Charge Mobility in a Tetrathiafulvalene-Based Microporous Metal-Organic Framework. *J. Am. Chem. Soc.* **2012**, *134*, 12932−12935.
(38) Chen, D.; Xing, H.; Su, Z.; Wang, C. Electrical Conductivity and Electroluminescence of a New Anthracene-Based Metal-Organic Framework with π-Conjugated Zigzag Chains. *Chem. Commun.* **2016**, *52*, 2019−2022.
(39) Batten, S. R.; Champness, N. R.; Chen, X.-M.; Garcia-Martinez, J.; Kitagawa, S.; Öhrström, L.; O'Keeffe, M.; Paik Suh, M.; Reedijk, J. Terminology of Metal-Organic Frameworks and Coordination Polymers (IUPAC Recommendations 2013). *Pure Appl. Chem.* **2013**, *85*, 1715−1724.
(40) Sun, L.; Campbell, M. G.; Dincă, M. Electrically Conductive Porous Metal−Organic Frameworks. *Angew. Chem., Int. Ed.* **2016**, *55*, 3566−3579.
(41) Medina, D. D.; Maehringer, A.; Bein, T. Electroactive Metalorganic Frameworks. *Isr. J. Chem.* **2018**, *58*, 1089−1101.
(42) D'Alessandro, D. M.; Kanga, J. R. R.; Caddy, J. S. Towards Conducting Metal-Organic Frameworks. *Aust. J. Chem.* **2011**, *64*, 718−722.
(43) Hendon, C. H.; Tiana, D.; Walsh, A. Conductive Metal-Organic Frameworks and Networks: Fact or Fantasy? *Phys. Chem. Chem. Phys.* **2012**, *14*, 13120−13132.
(44) Leong, C. F.; Usov, P. M.; D'Alessandro, D. M. Intrinsically Conducting Metal−Organic Frameworks. *MRS Bull.* **2016**, *41*, 858−864.
(45) Walsh, A.; Butler, K. T.; Hendon, C. H. Chemical Principles for Electroactive Metal-Organic Frameworks. *MRS Bull.* **2016**, *41*, 870−876.
(46) Murase, R.; Ding, B.; Gu, Q.; D'Alessandro, D. M. Prospects for Electroactive and Conducting Framework Materials. *Philos. Trans. R. Soc., A* **2019**, *377*, 20180226.
(47) Ko, M.; Mendecki, L.; Mirica, K. A. Conductive Two-Dimensional Metal−Organic Frameworks as Multifunctional Materials. *Chem. Commun.* **2018**, *54*, 7873−7891.
(48) Zheng, W.; Tsang, C.-S.; Lee, L. Y. S.; Wong, K.-Y. Two-Dimensional Metal-Organic Framework and Covalent-Organic Framework: Synthesis and Their Energy-Related Applications. *Mater. Today Chem.* **2019**, *12*, 34−60.
(49) Solomos, M. A.; Claire, F. J.; Kempa, T. J. 2D Molecular Crystal Lattices: Advances in Their Synthesis, Characterization, and Application. *J. Mater. Chem. A* **2019**, *7*, 23537−23562.
(50) Murase, R.; Leong, C. F.; D'Alessandro, D. M. Mixed Valency as a Strategy for Achieving Charge Delocalization in Semiconducting and Conducting Framework Materials. *Inorg. Chem.* **2017**, *56*, 14373−14382.
(51) Downes, C. A.; Marinescu, S. C. Electrocatalytic Metal−Organic Frameworks for Energy Applications. *ChemSusChem* **2017**, *10*, 4374−4392.
(52) Campbell, M. G.; Dincă, M. Metal−Organic Frameworks as Active Materials in Electronic Sensor Devices. *Sensors* **2017**, *17*, 1108.
(53) Koo, W.-T.; Jang, J.-S.; Kim, I.-D. Metal-Organic Frameworks for Chemiresistive Sensors. *Chem.* **2019**, *5*, 1938−1963.
(54) Meng, Z.; Stolz, R. M.; Mendecki, L.; Mirica, K. A. Electrically-Transduced Chemical Sensors Based on Two-Dimensional Nanomaterials. *Chem. Rev.* **2019**, *119*, 478−598.
(55) Stassen, I.; Burtch, N.; Talin, A.; Falcaro, P.; Allendorf, M.; Ameloot, R. An Updated Roadmap for the Integration of Metal-Organic Frameworks with Electronic Devices and Chemical Sensors. *Chem. Soc. Rev.* **2017**, *46*, 3185−3241.
(56) Sun, L.; Park, S. S.; Sheberla, D.; Dincă, M. Measuring and Reporting Electrical Conductivity in Metal−Organic Frameworks: Cd_2(TTFTB) as a Case Study. *J. Am. Chem. Soc.* **2016**, *138*, 14772−14782.
(57) Givaja, G.; Amo-Ochoa, P.; Gómez-García, C. J.; Zamora, F. Electrical Conductive Coordination Polymers. *Chem. Soc. Rev.* **2012**, *41*, 115−147.
(58) Kittel, C. *Introduction to Solid State Physics*; Wiley, 2004.
(59) Robin, M. B.; Day, P. Mixed Valence Chemistry—A Survey and Classification. In *Advances in Inorganic Chemistry and Radiochemistry*; Academic Press, 1968; pp 247−422.
(60) Mott, N. F.; Davis, E. A. *Electronic Processes in Non-Crystalline Materials*; Oxford University Press, 2012.
(61) Shklovskii, B. I.; Efros, A. L. *Electronic Properties of Doped Semiconductors*; Springer Series in Solid-State Sciences; Springer: Berlin, 1984; Vol. 45.
(62) Mataré, H. F. Carrier Transport at Grain Boundaries in Semiconductors. *J. Appl. Phys.* **1984**, *56*, 2605−2631.
(63) Foster, M. E.; Sohlberg, K.; Allendorf, M. D.; Talin, A. A. Unraveling the Semiconducting/Metallic Discrepancy in Ni_3(HITP)$_2$. *J. Phys. Chem. Lett.* **2018**, *9*, 481−486.
(64) Takaishi, S.; Hosoda, M.; Kajiwara, T.; Miyasaka, H.; Yamashita, M.; Nakanishi, Y.; Kitagawa, Y.; Yamaguchi, K.; Kobayashi, A.; Kitagawa, H. Electroconductive Porous Coordination Polymer Cu[Cu(Pdt)$_2$] Composed of Donor and Acceptor Building Units. *Inorg. Chem.* **2009**, *48*, 9048−9050.
(65) Kambe, T.; Sakamoto, R.; Hoshiko, K.; Takada, K.; Miyachi, M.; Ryu, J.-H.; Sasaki, S.; Kim, J.; Nakazato, K.; Takata, M.; et al. π-Conjugated Nickel Bis(Dithiolene) Complex Nanosheet. *J. Am. Chem. Soc.* **2013**, *135*, 2462−2465.
(66) Sun, L.; Miyakai, T.; Seki, S.; Dincă, M. Mn_2(2,5-Disulfhydrylbenzene-1,4-Dicarboxylate): A Microporous Metal−Organic Framework with Infinite $(-Mn-S-)_\infty$ Chains and High Intrinsic Charge Mobility. *J. Am. Chem. Soc.* **2013**, *135*, 8185−8188.
(67) Sun, L.; Hendon, C. H.; Minier, M. A.; Walsh, A.; Dincă, M. Million-Fold Electrical Conductivity Enhancement in Fe_2(DEBDC) versus Mn_2(DEBDC) (E = S, O). *J. Am. Chem. Soc.* **2015**, *137*, 6164−6167.
(68) Sun, L.; Hendon, C. H.; Park, S. S.; Tulchinsky, Y.; Wan, R.; Wang, F.; Walsh, A.; Dincă, M. Is Iron Unique in Promoting Electrical Conductivity in MOFs? *Chem. Sci.* **2017**, *8*, 4450−4457.
(69) Aubrey, M. L.; Wiers, B. M.; Andrews, S. C.; Sakurai, T.; Reyes-Lillo, S. E.; Hamed, S. M.; Yu, C.-J.; Darago, L. E.; Mason, J. A.; Baeg, J.-O.; et al. Electron Delocalization and Charge Mobility as a Function of Reduction in a Metal−Organic Framework. *Nat. Mater.* **2018**, *17*, 625−632.
(70) Xie, L. S.; Sun, L.; Wan, R.; Park, S. S.; DeGayner, J. A.; Hendon, C. H.; Dincă, M. Tunable Mixed-Valence Doping toward

https://dx.doi.org/10.1021/acs.chemrev.9b00766
Chem. Rev. 2020, 120, 8536−8580

Record Electrical Conductivity in a Three-Dimensional Metal−Organic Framework. *J. Am. Chem. Soc.* **2018**, *140*, 7411−7414.
(71) Gándara, F.; Uribe-Romo, F. J.; Britt, D. K.; Furukawa, H.; Lei, L.; Cheng, R.; Duan, X.; O'Keeffe, M.; Yaghi, O. M. Porous, Conductive Metal-Triazolates and Their Structural Elucidation by the Charge-Flipping Method. *Chem. - Eur. J.* **2012**, *18*, 10595−10601.
(72) Park, J. G.; Aubrey, M. L.; Oktawiec, J.; Chakarawet, K.; Darago, L. E.; Grandjean, F.; Long, G. J.; Long, J. R. Charge Delocalization and Bulk Electronic Conductivity in the Mixed-Valence Metal−Organic Framework Fe(1,2,3-Triazolate)$_2$(BF$_4$)$_x$. *J. Am. Chem. Soc.* **2018**, *140*, 8526−8534.
(73) Silvestre, J.; Hoffmann, R. Tetrahedral and Square-Planar One-Dimensional Chains: The Interplay of Crystal Field and Bandwidth in MS_2 Compounds. *Inorg. Chem.* **1985**, *24*, 4108−4119.
(74) Holliday, B. J.; Swager, T. M. Conducting Metallopolymers: The Roles of Molecular Architecture and Redox Matching. *Chem. Commun.* **2005**, 23−36.
(75) Sheberla, D.; Sun, L.; Blood-Forsythe, M. A.; Er, S.; Wade, C. R.; Brozek, C. K.; Aspuru-Guzik, A.; Dincă, M. High Electrical Condutivity in Ni_3(2,3,6,7,10,11-Hexaiminotriphenylene)$_2$, a Semiconducting Metal−Organic Graphene Analogue. *J. Am. Chem. Soc.* **2014**, *136*, 8859−8862.
(76) Huang, X.; Sheng, P.; Tu, Z.; Zhang, F.; Wang, J.; Geng, H.; Zou, Y.; Di, C.; Yi, Y.; Sun, Y.; et al. A Two-Dimensional π−d Conjugated Coordination Polymer with Extremely High Electrical Conductivity and Ambipolar Transport Behaviour. *Nat. Commun.* **2015**, *6*, 7408.
(77) Dou, J. H.; Sun, L.; Ge, Y.; Li, W.; Hendon, C. H.; Li, J.; Gul, S.; Yano, J.; Stach, E. A.; Dincă, M. Signature of Metallic Behavior in the Metal-Organic Frameworks M_3(Hexaiminobenzene)$_2$ (M = Ni, Cu). *J. Am. Chem. Soc.* **2017**, *139*, 13608−13611.
(78) Dong, R.; Han, P.; Arora, H.; Ballabio, M.; Karakus, M.; Zhang, Z.; Shekhar, C.; Adler, P.; Petkov, P. S.; Erbe, A.; et al. High-Mobility Band-like Charge Transport in a Semiconducting Two-Dimensional Metal−Organic Framework. *Nat. Mater.* **2018**, *17*, 1027−1032.
(79) Day, R. W.; Bediako, D. K.; Rezaee, M.; Parent, L. R.; Skorupskii, G.; Arguilla, M. Q.; Hendon, C. H.; Stassen, I.; Gianneschi, N.; Kim, P.; et al. Single Crystals of Electrically Conductive 2D MOFs: Structural and Electrical Transport Properties. *ACS Cent. Sci.* **2019**, *5*, 1959−1964.
(80) Coropceanu, V.; Cornil, J.; da Silva Filho, D. A.; Olivier, Y.; Silbey, R.; Brédas, J.-L. Charge Transport in Organic Semiconductors. *Chem. Rev.* **2007**, *107*, 926−952.
(81) Avendano, C.; Zhang, Z.; Ota, A.; Zhao, H.; Dunbar, K. R. Dramatically Different Conductivity Properties of Metal-Organic Framework Polymorphs of Tl(TCNQ): An Unexpected Room-Temperature Crystal-to-Crystal Phase Transition. *Angew. Chem., Int. Ed.* **2011**, *50*, 6543−6547.
(82) Heintz, R. A.; Zhao, H.; Ouyang, X.; Grandinetti, G.; Cowen, J.; Dunbar, K. R. New Insight into the Nature of Cu(TCNQ): Solution Routes to Two Distinct Polymorphs and Their Relationship to Crystalline Films That Display Bistable Switching Behavior. *Inorg. Chem.* **1999**, *38*, 144−156.
(83) Zhang, X.; Wang, Z.-X.; Xie, H.; Li, M.-X.; Woods, T. J.; Dunbar, K. R. A Cobalt(II) Spin-Crossover Compound with Partially Charged TCNQ Radicals and an Anomalous Conducting Behavior. *Chem. Sci.* **2016**, *7*, 1569−1574.
(84) Park, S. S.; Hontz, E. R.; Sun, L.; Hendon, C. H.; Walsh, A.; Van Voorhis, T.; Dincă, M. Cation-Dependent Intrinsic Electrical Conductivity in Isostructural Tetrathiafulvalene-Based Microporous Metal-Organic Frameworks. *J. Am. Chem. Soc.* **2015**, *137*, 1774−1777.
(85) Xie, L. S.; Alexandrov, E. V.; Skorupskii, G.; Proserpio, D. M.; Dincă, M. Diverse π−π Stacking Motifs Modulate Electrical Conductivity in Tetrathiafulvalene-Based Metal−Organic Frameworks. *Chem. Sci.* **2019**, *10*, 8558−8565.
(86) Castells-Gil, J.; Mañas-Valero, S.; Vitórica-Yrezábal, I. J.; Ananias, D.; Rocha, J.; Santiago, R.; Bromley, S. T.; Baldoví, J. J.; Coronado, E.; Souto, M.; et al. Electronic, Structural and Functional Versatility in Tetrathiafulvalene-Lanthanide Metal-Organic Frameworks. *Chem. - Eur. J.* **2019**, *25*, 12636−12643.
(87) Su, J.; Hu, T.-H.; Murase, R.; Wang, H.-Y.; D'Alessandro, D. M.; Kurmoo, M.; Zuo, J.-L. Redox Activities of Metal-Organic Frameworks Incorporating Rare-Earth Metal Chains and Tetrathiafulvalene Linkers. *Inorg. Chem.* **2019**, *58*, 3698−3706.
(88) Xie, L. S.; Dincă, M. Novel Topology in Semiconducting Tetrathiafulvalene Lanthanide Metal-Organic Frameworks. *Isr. J. Chem.* **2018**, *58*, 1119−1122.
(89) Haider, G.; Usman, M.; Chen, T.-P.; Perumal, P.; Lu, K.-L.; Chen, Y.-F. Electrically Driven White Light Emission from Intrinsic Metal−Organic Framework. *ACS Nano* **2016**, *10*, 8366−8375.
(90) Qu, L.; Iguchi, H.; Takaishi, S.; Habib, F.; Leong, C. F.; D'Alessandro, D. M.; Yoshida, T.; Abe, H.; Nishibori, E.; Yamashita, M. Porous Molecular Conductor: Electrochemical Fabrication of Through-Space Conduction Pathways among Linear Coordination Polymers. *J. Am. Chem. Soc.* **2019**, *141*, 6802−6806.
(91) Kuang, X.; Chen, S.; Meng, L.; Chen, J.; Wu, X.; Zhang, G.; Zhong, G.; Hu, T.; Li, Y.; Lu, C.-Z. Supramolecular Aggregation of a Redox-Active Copper-Naphthalenediimide Network with Intrinsic Electron Conduction. *Chem. Commun.* **2019**, *55*, 1643−1646.
(92) Skorupskii, G.; Trump, B. A.; Kasel, T. W.; Brown, C. M.; Hendon, C. H.; Dincă, M. Efficient and Tunable One-Dimensional Charge Transport in Layered Lanthanide Metal-Organic Frameworks. *Nat. Chem.* **2020**, *12*, 131−136.
(93) Hoffmann, R. *Solids and Surfaces: A Chemist's View of Bonding in Extended Structures*; VCH: New York, 1988.
(94) Kambe, T.; Sakamoto, R.; Kusamoto, T.; Pal, T.; Fukui, N.; Hoshiko, K.; Shimojima, T.; Wang, Z.; Hirahara, T.; Ishizaka, K.; et al. Redox Control and High Conductivity of Nickel Bis(Dithiolene) Complex π-Nanosheet: A Potential Organic Two-Dimensional Topological Insulator. *J. Am. Chem. Soc.* **2014**, *136*, 14357−14360.
(95) Butler, K. T.; Hendon, C. H.; Walsh, A. Electronic Chemical Potentials of Porous Metal-Organic Frameworks. *J. Am. Chem. Soc.* **2014**, *136*, 2703−2706.
(96) Leong, C. F.; Wang, C.-H.; Ling, C. D.; D'Alessandro, D. M. A Spectroscopic and Electrochemical Investigation of a Tetrathiafulvalene Series of Metal−Organic Frameworks. *Polyhedron* **2018**, *154*, 334−342.
(97) Wang, L.; Han, Y.; Feng, X.; Zhou, J.; Qi, P.; Wang, B. Metal−Organic Frameworks for Energy Storage: Batteries and Supercapacitors. *Coord. Chem. Rev.* **2016**, *307*, 361−381.
(98) Wang, H.; Zhu, Q.-L.; Zou, R.; Xu, Q. Metal-Organic Frameworks for Energy Applications. *Chem.* **2017**, *2*, 52−80.
(99) Wu, H. B.; Lou, X. W. Metal-Organic Frameworks and Their Derived Materials for Electrochemical Energy Storage and Conversion: Promises and Challenges. *Sci. Adv.* **2017**, *3*, eaap9252.
(100) Stassen, I.; Dou, J.-H.; Hendon, C.; Dincă, M. Chemiresistive Sensing of Ambient CO_2 by an Autogenously Hydrated Cu_3(Hexaiminobenzene)$_2$ Framework. *ACS Cent. Sci.* **2019**, *5*, 1425−1431.
(101) Matheu, R.; Gutierrez-Puebla, E.; Monge, M. Á.; Diercks, C. S.; Kang, J.; Prévot, M. S.; Pei, X.; Hanikel, N.; Zhang, B.; Yang, P.; et al. Three-Dimensional Phthalocyanine Metal-Catecholates for High Electrochemical Carbon Dioxide Reduction. *J. Am. Chem. Soc.* **2019**, *141*, 17081−17085.
(102) Rosi, N. L.; Kim, J.; Eddaoudi, M.; Chen, B.; O'Keeffe, M.; Yaghi, O. M. Rod Packings and Metal−Organic Frameworks Constructed from Rod-Shaped Secondary Building Units. *J. Am. Chem. Soc.* **2005**, *127*, 1504−1518.
(103) Férey, G.; Millange, F.; Morcrette, M.; Serre, C.; Doublet, M.-L.; Grenèche, J.-M.; Tarascon, J.-M. Mixed-Valence Li/Fe-Based Metal−Organic Frameworks with Both Reversible Redox and Sorption Properties. *Angew. Chem., Int. Ed.* **2007**, *46*, 3259−3263.
(104) Medina, M. E.; Dumont, Y.; Grenèche, J.-M.; Millange, F. FeIII/FeII Regular Charge Order in Metal-Organic Framework. *Chem. Commun.* **2010**, *46*, 7987−7989.
(105) Leclerc, H.; Devic, T.; Devautour-Vinot, S.; Bazin, P.; Audebrand, N.; Férey, G.; Daturi, M.; Vimont, A.; Clet, G. Influence

https://dx.doi.org/10.1021/acs.chemrev.9b00766
Chem. Rev. 2020, 120, 8536−8580

of the Oxidation State of the Metal Center on the Flexibility and Adsorption Properties of a Porous Metal Organic Framework: MIL-47(V). *J. Phys. Chem. C* **2011**, *115*, 19828−19840.
(106) Dietzel, P. D. C.; Blom, R.; Fjellvåg, H. Base-Induced Formation of Two Magnesium Metal-Organic Framework Compounds with a Bifunctional Tetratopic Ligand. *Eur. J. Inorg. Chem.* **2008**, *2008*, 3624−3632.
(107) Zhou, W.; Wu, H.; Yildirim, T. Enhanced H_2 Adsorption in Isostructural Metal-Organic Frameworks with Open Metal Sites: Strong Dependence of the Binding Strength on Metal Ions. *J. Am. Chem. Soc.* **2008**, *130*, 15268−15269.
(108) Bhattacharjee, S.; Choi, J.-S.; Yang, S.-T.; Choi, S. B.; Kim, J.; Ahn, W.-S. Solvothermal Synthesis of Fe-MOF-74 and Its Catalytic Properties in Phenol Hydroxylation. *J. Nanosci. Nanotechnol.* **2010**, *10*, 135−141.
(109) Bloch, E. D.; Murray, L. J.; Queen, W. L.; Chavan, S.; Maximoff, S. N.; Bigi, J. P.; Krishna, R.; Peterson, V. K.; Grandjean, F.; Long, G. J.; et al. Selective Binding of O_2 over N_2 in a Redox-Active Metal-Organic Framework with Open Iron(II) Coordination Sites. *J. Am. Chem. Soc.* **2011**, *133*, 14814−14822.
(110) Dietzel, P. D. C.; Morita, Y.; Blom, R.; Fjellvåg, H. An in Situ High-Temperature Single-Crystal Investigation of a Dehydrated Metal-Organic Framework Compound and Field-Induced Magnetization of One-Dimensional Metal-Oxygen Chains. *Angew. Chem., Int. Ed.* **2005**, *44*, 6354−6358.
(111) Dietzel, P. D. C.; Panella, B.; Hirscher, M.; Blom, R.; Fjellvåg, H. Hydrogen Adsorption in a Nickel Based Coordination Polymer with Open Metal Sites in the Cylindrical Cavities of the Desolvated Framework. *Chem. Commun.* **2006**, 959−961.
(112) Sanz, R.; Martínez, F.; Orcajo, G.; Wojtas, L.; Briones, D. Synthesis of a Honeycomb-like Cu-Based Metal-Organic Framework and Its Carbon Dioxide Adsorption Behaviour. *Dalt. Trans.* **2013**, *42*, 2392−2398.
(113) Scheurle, P. I.; Mähringer, A.; Jakowetz, A. C.; Hosseini, P.; Richter, A. F.; Wittstock, G.; Medina, D. D.; Bein, T. A Highly Crystalline Anthracene-Based MOF-74 Series Featuring Electrical Conductivity and Luminescence. *Nanoscale* **2019**, *11*, 20949−20955.
(114) Sun, L.; Hendon, C. H.; Dincă, M. Coordination-Induced Reversible Electrical Conductivity Variation in the MOF-74 Analogue Fe_2(DSBDC). *Dalt. Trans.* **2018**, *47*, 11739−11743.
(115) Fuma, Y.; Ebihara, M.; Kutsumizu, S.; Kawamura, T. A Diamondoid Network of Tetrakis(Acetamidato)Dirhodium in Mixed Oxidation States Linked by μ_4-Iodide Having a 10^5 Enhancement of Its Electrical Conductivity by Water of Molecules of Hydration. *J. Am. Chem. Soc.* **2004**, *126*, 12238−12239.
(116) Katritzky, A. R.; Ramsden, C. A.; Joule, J. A.; Zhdankin, V. V. *Handbook of Heterocyclic Chemistry*, 3rd ed.; Elsevier: Amsterdam, 2010.
(117) Zhang, J.-P.; Zhang, Y.-B.; Lin, J.-B.; Chen, X.-M. Metal Azolate Frameworks: From Crystal Engineering to Functional Materials. *Chem. Rev.* **2012**, *112*, 1001−1033.
(118) Kahn, O.; Martinez, C. J. Spin-Transition Polymers: From Molecular Materials toward Memory Devices. *Science* **1998**, *279*, 44−48.
(119) Bousseksou, A.; Molnár, G.; Salmon, L.; Nicolazzi, W. Molecular Spin Crossover Phenomenon: Recent Achievements and Prospects. *Chem. Soc. Rev.* **2011**, *40*, 3313−3335.
(120) Koningsbruggen, P. J. Special Classes of Iron(II) Azole Spin Crossover Compounds. *Top. Curr. Chem.* **2012**, *233*, 123−149.
(121) Reed, D. A.; Keitz, B. K.; Oktawiec, J.; Mason, J. A.; Runčevski, T.; Xiao, D. J.; Darago, L. E.; Crocellà, V.; Bordiga, S.; Long, J. R. A Spin Transition Mechanism for Cooperative Adsorption in Metal−Organic Frameworks. *Nature* **2017**, *550*, 96−100.
(122) Tulchinsky, Y.; Hendon, C. H.; Lomachenko, K. A.; Borfecchia, E.; Melot, B. C.; Hudson, M. R.; Tarver, J. D.; Korzyński, M. D.; Stubbs, A. W.; Kagan, J. J.; et al. Reversible Capture and Release of Cl_2 and Br_2 with a Redox-Active Metal−-Organic Framework. *J. Am. Chem. Soc.* **2017**, *139*, 5992−5997.
(123) Creutz, C. Mixed Valence Complexes of d^5-d^6 Metal Centers. *Prog. Inorg. Chem.* **1983**, *30*, 1−73.
(124) Zhou, X. H.; Peng, Y. H.; Du, X. Di; Zuo, J. L.; You, X. Z. Hydrothermal Syntheses and Structures of Three Novel Coordination Polymers Assembled from 1,2,3-Triazolate Ligands. *CrystEngComm* **2009**, *11*, 1964−1970.
(125) Yan, Z.; Li, M.; Gao, H.-L.; Huang, X.-C.; Li, D. High-Spin versus Spin-Crossover versus Low-Spin: Geometry Intervention in Cooperativity in a 3D Polymorphic Iron(II)−Tetrazole MOFs System. *Chem. Commun.* **2012**, *48*, 3960−3962.
(126) Manumpil, M. A.; Leal-Cervantes, C.; Hudson, M. R.; Brown, C. M.; Karunadasa, H. I. Electronic Conductivity in a Porous Vanadyl Prussian Blue Analogue upon Air Exposure. *Inorg. Chem.* **2017**, *56*, 12682−12686.
(127) Rieth, A. J.; Tulchinsky, Y.; Dincă, M. High and Reversible Ammonia Uptake in Mesoporous Azolate Metal-Organic Frameworks with Open Mn, Co, and Ni Sites. *J. Am. Chem. Soc.* **2016**, *138*, 9401−9404.
(128) Rieth, A. J.; Wright, A. M.; Dincă, M. Kinetic Stability of Metal-Organic Frameworks for Corrosive and Coordinating Gas Capture. *Nat. Rev. Mater.* **2019**, *4*, 708−725.
(129) Pathak, A.; Shen, J.-W.; Usman, M.; Wei, L.-F.; Mendiratta, S.; Chang, Y.-S.; Sainbileg, B.; Ngue, C.-M.; Chen, R.-S.; Hayashi, M.; et al. Integration of a $(-Cu-S-)_n$ Plane in a Metal-Organic Framework Affords High Electrical Conductivity. *Nat. Commun.* **2019**, *10*, 1721.
(130) Novoselov, K. S.; Geim, A. K.; Morozov, S. V.; Jiang, D.; Zhang, Y.; Dubonos, S. V.; Grigorieva, I. V.; Firsov, A. A. Electric Field Effect in Atomically Thin Carbon Films. *Science* **2004**, *306*, 666−669.
(131) Castro Neto, A. H.; Peres, N. M. R.; Novoselov, K. S.; Geim, A. K.; et al. The Electronic Properties of Graphene. *Rev. Mod. Phys.* **2009**, *81*, 109−162.
(132) Allen, M. J.; Tung, V. C.; Kaner, R. B. Honeycomb Carbon: A Review of Graphene. *Chem. Rev.* **2010**, *110*, 132−145.
(133) Wang, Q. H.; Kalantar-Zadeh, K.; Kis, A.; Coleman, J. N.; Strano, M. S. Electronics and Optoelectronics of Two-Dimensional Transition Metal Dichalcogenides. *Nat. Nanotechnol.* **2012**, *7*, 699−712.
(134) Xu, M.; Liang, T.; Shi, M.; Chen, H. Graphene-Like Two-Dimensional Materials. *Chem. Rev.* **2013**, *113*, 3766−3798.
(135) Butler, S. Z.; Hollen, S. M.; Cao, L.; Cui, Y.; Gupta, J. A.; Gutiérrez, H. R.; Heinz, T. F.; Hong, S. S.; Huang, J.; Ismach, A. F.; et al. Progress, Challenges, and Opportunities in Two-Dimensional Materials Beyond Graphene. *ACS Nano* **2013**, *7*, 2898−2926.
(136) Molle, A.; Goldberger, J.; Houssa, M.; Xu, Y.; Zhang, S.-C.; Akinwande, D. Buckled Two-Dimensional Xene Sheets. *Nat. Mater.* **2017**, *16*, 163−169.
(137) Gutzler, R.; Perepichka, D. F. π-Electron Conjugation in Two Dimensions. *J. Am. Chem. Soc.* **2013**, *135*, 16585−16594.
(138) Boott, C. E.; Nazemi, A.; Manners, I. Synthetic Covalent and Non-Covalent 2D Materials. *Angew. Chem., Int. Ed.* **2015**, *54*, 13876−13894.
(139) Sproules, S.; Wieghardt, K. Dithiolene Radicals: Sulfur K-Edge X-Ray Absorption Spectroscopy and Harry's Intuition. *Coord. Chem. Rev.* **2011**, *255*, 837−860.
(140) Eisenberg, R.; Gray, H. B. Noninnocence in Metal Complexes: A Dithiolene Dawn. *Inorg. Chem.* **2011**, *50*, 9741−9751.
(141) Robertson, N.; Cronin, L. Metal Bis-1,2-Dithiolene Complexes in Conducting or Magnetic Crystalline Assemblies. *Coord. Chem. Rev.* **2002**, *227*, 93−127.
(142) Stiefel, E. I.; Waters, J. H.; Billig, E.; Gray, H. B. The Myth of Nickel(III) and Nickel(IV) in Planar Complexes. *J. Am. Chem. Soc.* **1965**, *87*, 3016−3017.
(143) Noro, S.; Chang, H.-C.; Takenobu, T.; Murayama, Y.; Kanbara, T.; Aoyama, T.; Sassa, T.; Wada, T.; Tanaka, D.; Kitagawa, S.; et al. Metal−Organic Thin-Film Transistor (MOTFT) Based on a Bis(o-Diiminobenzosemiquinonate) Nickel(II) Complex. *J. Am. Chem. Soc.* **2005**, *127*, 10012−10013.

https://dx.doi.org/10.1021/acs.chemrev.9b00766
Chem. Rev. 2020, 120, 8536−8580

(144) Bachler, V.; Olbrich, G.; Neese, F.; Wieghardt, K. Theoretical Evidence for the Singlet Diradical Character of Square Planar Nickel Complexes Containing Two O-Semiquinonato Type Ligands. *Inorg. Chem.* **2002**, *41*, 4179−4193.
(145) Kitagawa, S.; Kawata, S. Coordination Compounds of 1,4-Dihydroxybenzoquinone and Its Homologues. Structures and Properties. *Coord. Chem. Rev.* **2002**, *224*, 11−34.
(146) Min, K. S.; DiPasquale, A. G.; Golen, J. A.; Rheingold, A. L.; Miller, J. S. Synthesis, Structure, and Magnetic Properties of Valence Ambiguous Dinuclear Antiferromagnetically Coupled Cobalt and Ferromagnetically Coupled Iron Complexes Containing the Chloranilate(2−) and the Significantly Stronger Coupling Chloranilate(•3−) Radical Trianion. *J. Am. Chem. Soc.* **2007**, *129*, 2360−2368.
(147) Demir, S.; Jeon, I.-R.; Long, J. R.; Harris, T. D. Radical Ligand-Containing Single-Molecule Magnets. *Coord. Chem. Rev.* **2015**, *289*−*290*, 149−176.
(148) Hmadeh, M.; Lu, Z.; Liu, Z.; Gándara, F.; Furukawa, H.; Wan, S.; Augustyn, V.; Chang, R.; Liao, L.; Zhou, F.; et al. New Porous Crystals of Extended Metal-Catecholates. *Chem. Mater.* **2012**, *24*, 3511−3513.
(149) DeGayner, J. A.; Jeon, I.-R.; Sun, L.; Dincă, M.; Harris, T. D. 2D Conductive Iron-Quinoid Magnets Ordering up to T c = 105 K via Heterogenous Redox Chemistry. *J. Am. Chem. Soc.* **2017**, *139*, 4175−4184.
(150) Liu, L.; DeGayner, J. A.; Sun, L.; Zee, D. Z.; Harris, T. D. Reversible Redox Switching of Magnetic Order and Electrical Conductivity in a 2D Manganese Benzoquinoid Framework. *Chem. Sci.* **2019**, *10*, 4652−4661.
(151) Benmansour, S.; Abhervé, A.; Gómez-Claramunt, P.; Vallés-García, C.; Gómez-García, C. J. Nanosheets of Two-Dimensional Magnetic and Conducting Fe(II)/Fe(III) Mixed-Valence Metal−Organic Frameworks. *ACS Appl. Mater. Interfaces* **2017**, *9*, 26210−26218.
(152) Ziebel, M. E.; Darago, L. E.; Long, J. R. Control of Electronic Structure and Conductivity in Two-Dimensional Metal−Semiquinoid Frameworks of Titanium, Vanadium, and Chromium. *J. Am. Chem. Soc.* **2018**, *140*, 3040−3051.
(153) Darago, L. E.; Aubrey, M. L.; Yu, C. J.; Gonzalez, M. I.; Long, J. R. Electronic Conductivity, Ferrimagnetic Ordering, and Reductive Insertion Mediated by Organic Mixed-Valence in a Ferric Semiquinoid Metal−Organic Framework. *J. Am. Chem. Soc.* **2015**, *137*, 15703−15711.
(154) Wang, Y.; Liu, X.; Li, X.; Zhai, F.; Yan, S.; Liu, N.; Chai, Z.; Xu, Y.; Ouyang, X.; Wang, S.; et al. Direct Radiation Detection by a Semiconductive Metal-Organic Framework. *J. Am. Chem. Soc.* **2019**, *141*, 8030−8034.
(155) Weiss, A.; Riegler, E.; Robl, C. Polymeric 2,5-Dihydroxy-1,4-Benzoquinone Transition Metal Complexes $Na_2(H_2O)_{24}[M_2(C_6H_2O_4)_3]$ (M = Mn^{2+}, Cd^{2+}). *Z. Naturforsch., B: J. Chem. Sci.* **1986**, *41*, 1501−1505.
(156) Shilov, G. V.; Nikitina, Z. K.; Ovanesyan, N. S.; Aldoshin, S. M.; Makhaev, V. D. Phenazineoxonium Chloranilatomanganate and Chloranilatoferrate: Synthesis, Structure, Magnetic Properties, and Mössbauer Spectra. *Russ. Chem. Bull.* **2011**, *60*, 1209−1219.
(157) Pedersen, K. S.; Perlepe, P.; Aubrey, M. L.; Woodruff, D. N.; Reyes-Lillo, S. E.; Reinholdt, A.; Voigt, L.; Li, Z.; Borup, K.; Rouzières, M.; et al. Formation of the Layered Conductive Magnet $CrCl_2(Pyrazine)_2$ through Redox-Active Coordination Chemistry. *Nat. Chem.* **2018**, *10*, 1056−1061.
(158) Abrahams, B. F.; Hudson, T. A.; McCormick, L. J.; Robson, R. Coordination Polymers of 2,5-Dihydroxybenzoquinone and Chloranilic Acid with the (10,3)-*a* Topology. *Cryst. Growth Des.* **2011**, *11*, 2717−2720.
(159) Abrahams, B. F.; Coleiro, J.; Ha, K.; Hoskins, B. F.; Orchard, S. D.; Robson, R. Dihydroxybenzoquinone and Chloranilic Acid Derivatives of Rare Earth Metals. *J. Chem. Soc. Dalt. Trans.* **2002**, *8*, 1586−1594.
(160) Hoppe, B.; Hindricks, K. D. J.; Warwas, D. P.; Schulze, H. A.; Mohmeyer, A.; Pinkvos, T. J.; Zailskas, S.; Krey, M. R.; Belke, C.; König, S.; et al. Graphene-like Metal−Organic Frameworks: Morphology Control, Optimization of Thin Film Electrical Conductivity and Fast Sensing Applications. *CrystEngComm* **2018**, *20*, 6458−6471.
(161) Mähringer, A.; Jakowetz, A. C.; Rotter, J. M.; Bohn, B. J.; Stolarczyk, J. K.; Feldmann, J.; Bein, T.; Medina, D. D. Oriented Thin Films of Electroactive Triphenylene Catecholate-Based Two-Dimensional Metal−Organic Frameworks. *ACS Nano* **2019**, *13*, 6711−6719.
(162) Yao, M.-S.; Lv, X.-J.; Fu, Z.-H.; Li, W.-H.; Deng, W.-H.; Wu, G.-D.; Xu, G. Layer-by-Layer Assembled Conductive Metal-Organic Framework Nanofilms for Room-Temperature Chemiresistive Sensing. *Angew. Chem., Int. Ed.* **2017**, *56*, 16510−16514.
(163) Ko, M.; Aykanat, A.; Smith, M. K.; Mirica, K. A. Drawing Sensors with Ball-Milled Blends of Metal-Organic Frameworks and Graphite. *Sensors* **2017**, *17*, 2192.
(164) Smith, M. K.; Jensen, K. E.; Pivak, P. A.; Mirica, K. A. Direct Self-Assembly of Conductive Nanorods of Metal−Organic Frameworks into Chemiresistive Devices on Shrinkable Polymer Films. *Chem. Mater.* **2016**, *28*, 5264−5268.
(165) Li, W.-H.; Ding, K.; Tian, H.-R.; Yao, M.-S.; Nath, B.; Deng, W.-H.; Wang, Y.; Xu, G. Conductive Metal-Organic Framework Nanowire Array Electrodes for High-Performance Solid-State Supercapacitors. *Adv. Funct. Mater.* **2017**, *27*, 1702067.
(166) Rubio-Giménez, V.; Galbiati, M.; Castells-Gil, J.; Almora-Barrios, N.; Navarro-Sánchez, J.; Escorcia-Ariza, G.; Mattera, M.; Arnold, T.; Rawle, J.; Tatay, S.; et al. Bottom-Up Fabrication of Semiconductive Metal-Organic Framework Ultrathin Films. *Adv. Mater.* **2018**, *30*, 1704291.
(167) Nam, K. W.; Park, S. S.; dos Reis, R.; Dravid, V. P.; Kim, H.; Mirkin, C. A.; Stoddart, J. F. Conductive 2D Metal-Organic Framework for High-Performance Cathodes in Aqueous Rechargeable Zinc Batteries. *Nat. Commun.* **2019**, *10*, 4948.
(168) Wu, H.; Zhang, W.; Kandambeth, S.; Shekhah, O.; Eddaoudi, M.; Alshareef, H. N. Conductive Metal-Organic Frameworks Selectively Grown on Laser-Scribed Graphene for Electrochemical Microsupercapacitors. *Adv. Energy Mater.* **2019**, *9*, 1900482.
(169) Song, X.; Wang, X.; Li, Y.; Zheng, C.; Zhang, B.; Di, C.; Li, F.; Jin, C.; Mi, W.; Chen, L.; et al. 2D Semiconducting Metal-Organic Framework Thin Films for Organic Spin Valves. *Angew. Chem., Int. Ed.* **2020**, *59*, 1118−1123.
(170) Park, J.; Hinckley, A. C.; Huang, Z.; Feng, D.; Yakovenko, A. A.; Lee, M.; Chen, S.; Zou, X.; Bao, Z. Synthetic Routes for a 2D Semiconductive Copper Hexahydroxybenzene Metal−Organic Framework. *J. Am. Chem. Soc.* **2018**, *140*, 14533−14537.
(171) Yao, M.; Zheng, J.-J.; Wu, A.-Q.; Xu, G.; Nagarkar, S. S.; Zhang, G.; Tsujimoto, M.; Sakaki, S.; Horike, S.; Otake, K.; et al. Dual-Ligand Porous Coordination Polymer Chemiresistor with Modulated Conductivity and Porosity. *Angew. Chem., Int. Ed.* **2020**, *59*, 172−176.
(172) Nagatomi, H.; Yanai, N.; Yamada, T.; Shiraishi, K.; Kimizuka, N. Synthesis and Electric Properties of a Two-Dimensional Metal-Organic Framework Based on Phthalocyanine. *Chem. - Eur. J.* **2018**, *24*, 1806−1810.
(173) Yang, C.; Dong, R.; Wang, M.; Petkov, P. St.; Zhang, Z.; Wang, M.; Han, P.; Ballabio, M.; Bräuninger, S. A.; Liao, Z.; et al. A Semiconducting Layered Metal-Organic Framework Magnet. *Nat. Commun.* **2019**, *10*, 3260.
(174) Cui, J.; Xu, Z. An Electroactive Porous Network from Covalent Metal−Dithiolene Links. *Chem. Commun.* **2014**, *50*, 3986−3988.
(175) Kato, R. Conducting Metal Dithiolene Complexes: Structural and Electronic Properties. *Chem. Rev.* **2004**, *104*, 5319−5346.
(176) Clough, A. J.; Skelton, J. M.; Downes, C. A.; De La Rosa, A. A.; Yoo, J. W.; Walsh, A.; Melot, B. C.; Marinescu, S. C. Metallic Conductivity in a Two-Dimensional Cobalt Dithiolene Metal-Organic Framework. *J. Am. Chem. Soc.* **2017**, *139*, 10863−10867.
(177) Clough, A. J.; Orchanian, N. M.; Skelton, J. M.; Neer, A. J.; Howard, S. A.; Downes, C. A.; Piper, L. F. J.; Walsh, A.; Melot, B. C.; Marinescu, S. C. Room Temperature Metallic Conductivity in a

https://dx.doi.org/10.1021/acs.chemrev.9b00766
Chem. Rev. 2020, 120, 8536−8580

Metal−Organic Framework Induced by Oxidation. *J. Am. Chem. Soc.* **2019**, *141*, 16323−16330.
(178) Dong, R.; Zhang, Z.; Tranca, D. C.; Zhou, S.; Wang, M.; Adler, P.; Liao, Z.; Liu, F.; Sun, Y.; Shi, W.; et al. A Coronene-Based Semiconducting Two-Dimensional Metal-Organic Framework with Ferromagnetic Behavior. *Nat. Commun.* **2018**, *9*, 2637.
(179) Mendecki, L.; Ko, M.; Zhang, X.; Meng, Z.; Mirica, K. A. Porous Scaffolds for Electrochemically Controlled Reversible Capture and Release of Ethylene. *J. Am. Chem. Soc.* **2017**, *139*, 17229−17232.
(180) Pal, T.; Kambe, T.; Kusamoto, T.; Foo, M. L.; Matsuoka, R.; Sakamoto, R.; Nishihara, H. Interfacial Synthesis of Electrically Conducting Palladium Bis(Dithiolene) Complex Nanosheet. *ChemPlusChem* **2015**, *80*, 1255−1258.
(181) Huang, X.; Zhang, S.; Liu, L.; Yu, L.; Chen, G.; Xu, W.; Zhu, D. Superconductivity in a Copper(II)-Based Coordination Polymer with Perfect Kagome Structure. *Angew. Chem., Int. Ed.* **2018**, *57*, 146−150.
(182) Cui, Y.; Yan, J.; Chen, Z.; Zhang, J.; Zou, Y.; Sun, Y.; Xu, W.; Zhu, D. $Cu_3(C_6Se_6)]_n$: The First Highly Conductive 2D π-d Conjugated Coordination Polymer Based on Benzenehexaselenolate. *Adv. Sci.* **2019**, *6*, 1802235.
(183) Turner, D. L.; Vaid, T. P.; Stephens, P. W.; Stone, K. H.; DiPasquale, A. G.; Rheingold, A. L. Semiconducting Lead−Sulfur−Organic Network Solids. *J. Am. Chem. Soc.* **2008**, *130*, 14−15.
(184) Huang, X.; Li, H.; Tu, Z.; Liu, L.; Wu, X.; Chen, J.; Liang, Y.; Zou, Y.; Yi, Y.; Sun, J.; et al. Highly Conducting Neutral Coordination Polymer with Infinite Two-Dimensional Silver−Sulfur Networks. *J. Am. Chem. Soc.* **2018**, *140*, 15153−15156.
(185) Chen, I.-F.; Lu, C.-F.; Su, W.-F. Highly Conductive 2D Metal-Organic Framework Thin Film Fabricated by Liquid-Liquid Interfacial Reaction Using One-Pot-Synthesized Benzenehexathiol. *Langmuir* **2018**, *34*, 15754−15762.
(186) Jin, Z.; Yan, J.; Huang, X.; Xu, W.; Yang, S.; Zhu, D.; Wang, J. Solution-Processed Transparent Coordination Polymer Electrode for Photovoltaic Solar Cells. *Nano Energy* **2017**, *40*, 376−381.
(187) Huang, X.; Yao, H.; Cui, Y.; Hao, W.; Zhu, J.; Xu, W.; Zhu, D. Conductive Copper Benzenehexathiol Coordination Polymer as a Hydrogen Evolution Catalyst. *ACS Appl. Mater. Interfaces* **2017**, *9*, 40752−40759.
(188) Herebian, D.; Bothe, E.; Neese, F.; Weyhermüller, T.; Wieghardt, K. Molecular and Electronic Structures of Bis-(o-Diiminobenzosemiquinonato)Metal(II) Complexes (Ni, Pd, Pt), Their Monocations and -Anions, and of Dimeric Dications Containing Weak Metal−Metal Bonds. *J. Am. Chem. Soc.* **2003**, *125*, 9116−9128.
(189) Yuan, K.; Song, T.; Zhu, X.; Li, B.; Han, B.; Zheng, L.; Li, J.; Zhang, X.; Hu, W. Construction of Large-Area Ultrathin Conductive Metal−Organic Framework Films through Vapor-Induced Conversion. *Small* **2019**, *15*, 1804845.
(190) Wu, G.; Huang, J.; Zang, Y.; He, J.; Xu, G. Porous Field-Effect Transistors Based on a Semiconductive Metal−Organic Framework. *J. Am. Chem. Soc.* **2017**, *139*, 1360−1363.
(191) Lian, Y.; Yang, W.; Zhang, C.; Sun, H.; Deng, Z.; Xu, W.; Song, L.; Ouyang, Z.; Wang, Z.; Guo, J.; et al. Unpaired 3d Electron on Atomically Dispersed Cobalt Centre in Coordination Polymers to Regulate Both ORR Activity and Selectivity. *Angew. Chem., Int. Ed.* **2020**, *59*, 286−294.
(192) Lahiri, N.; Lotfizadeh, N.; Tsuchikawa, R.; Deshpande, V. V.; Louie, J. Hexaaminobenzene as a Building Block for a Family of 2D Coordination Polymers. *J. Am. Chem. Soc.* **2017**, *139*, 19−22.
(193) Jia, H.; Yao, Y.; Zhao, J.; Gao, Y.; Luo, Z.; Du, P. A Novel Two-Dimensional Nickel Phthalocyanine-Based Metal−Organic Framework for Highly Efficient Water Oxidation Catalysis. *J. Mater. Chem. A* **2018**, *6*, 1188−1195.
(194) Jiang, Y.; Oh, I.; Joo, S. H.; Buyukcakir, O.; Chen, X.; Lee, S. H.; Huang, M.; Seong, W. K.; Kwak, S. K.; Yoo, J.-W.; et al. Partial Oxidation-Induced Electrical Conductivity and Paramagnetism in a Ni(II) Tetraaza[14]Annulene-Linked Metal Organic Framework. *J. Am. Chem. Soc.* **2019**, *141*, 16884−16893.
(195) Sun, X.; Wu, K.-H.; Sakamoto, R.; Kusamoto, T.; Maeda, H.; Nishihara, H. Conducting π-Conjugated Bis(Iminothiolato)Nickel Nanosheet. *Chem. Lett.* **2017**, *46*, 1072−1075.
(196) Sun, X.; Wu, K.-H.; Sakamoto, R.; Kusamoto, T.; Maeda, H.; Ni, X.; Jiang, W.; Liu, F.; Sasaki, S.; Masunaga, H.; et al. Bis(Aminothiolato)Nickel Nanosheet as a Redox Switch for Conductivity and an Electrocatalyst for the Hydrogen Evolution Reaction. *Chem. Sci.* **2017**, *8*, 8078−8085.
(197) Wang, B.; Luo, Y.; Liu, B.; Duan, G. Field-Effect Transistor Based on an in Situ Grown Metal−Organic Framework Film as a Liquid-Gated Sensing Device. *ACS Appl. Mater. Interfaces* **2019**, *11*, 35935−35940.
(198) Leong, C. F.; Wang, C. H.; Ling, C. D.; D'Alessandro, D. M. A Spectroscopic and Electrochemical Investigation of a Tetrathiafulvalene Series of Metal−Organic Frameworks. *Polyhedron* **2018**, *154*, 334−342.
(199) Park, S. S.; Hendon, C. H.; Fielding, A. J.; Walsh, A.; O'Keeffe, M.; Dincă, M. The Organic Secondary Building Unit: Strong Intermolecular π Interactions Define Topology in MIT-25, a Mesoporous MOF with Proton-Replete Channels. *J. Am. Chem. Soc.* **2017**, *139*, 3619−3622.
(200) Wudl, F.; Smith, G. M.; Hufnagel, E. J. Bis-1,3-Dithiolium Chloride: An Unusually Stable Organic Radical Cation. *J. Chem. Soc. D* **1970**, 1453−1454.
(201) Bryce, M. R. Recent Progress on Conducting Organic Charge-Transfer Salts. *Chem. Soc. Rev.* **1991**, *20*, 355−390.
(202) Jørgensen, T.; Hansen, T. K.; Becher, J. Tetrathiafulvalenes as Building-Blocks in Supramolecular Chemistry. *Chem. Soc. Rev.* **1994**, *23*, 41−51.
(203) Nielsen, M. B.; Lomholt, C.; Becher, J. Tetrathiafulvalenes as Building Blocks in Supramolecular Chemistry II. *Chem. Soc. Rev.* **2000**, *29*, 153−164.
(204) Nguyen, T. L. A.; Demir-Cakan, R.; Devic, T.; Morcrette, M.; Ahnfeldt, T.; Auban-Senzier, P.; Stock, N.; Goncalves, A.-M.; Filinchuk, Y.; Tarascon, J.-M.; et al. 3-D Coordination Polymers Based on the Tetrathiafulvalenetetracarboxylate (TTF-TC) Derivative: Synthesis, Characterization, and Oxidation Issues. *Inorg. Chem.* **2010**, *49*, 7135−7143.
(205) Wang, H.-Y.; Cui, L.; Xie, J.-Z.; Leong, C. F.; D'Alessandro, D. M.; Zuo, J.-L. Functional Coordination Polymers Based on Redox-Active Tetrathiafulvalene and Its Derivatives. *Coord. Chem. Rev.* **2017**, *345*, 342−361.
(206) Pattengale, B.; Neu, J.; Ostresh, S.; Hu, G.; Spies, J. A.; Okabe, R.; Brudvig, G. W.; Schmuttenmaer, C. A. Metal−Organic Framework Photoconductivity via Time-Resolved Terahertz Spectroscopy. *J. Am. Chem. Soc.* **2019**, *141*, 9793−9797.
(207) Wang, H.-Y.; Ge, J.-Y.; Hua, C.; Jiao, C.-Q.; Wu, Y.; Leong, C. F.; D'Alessandro, D. M.; Liu, T.; Zuo, J.-L. Photo- and Electronically Switchable Spin-Crossover Iron(II) Metal-Organic Frameworks Based on a Tetrathiafulvalene Ligand. *Angew. Chem., Int. Ed.* **2017**, *56*, 5465−5470.
(208) Yu, Q.; Su, J.; Ma, J. P.; Leong, C. F.; D'Alessandro, D. M.; Wang, H. Y.; Kurmoo, M.; Zuo, J. L. Progressive Structure Designing and Property Tuning of Manganese(II) Coordination Polymers with the Tetra(4-Pyridyl)-Tetrathiafulvalene Ligand. *Cryst. Growth Des.* **2019**, *19*, 3012−3018.
(209) Wang, H.-Y.; Su, J.; Ma, J.-P.; Yu, F.; Leong, C. F.; D'Alessandro, D. M.; Kurmoo, M.; Zuo, J.-L. Concomitant Use of Tetrathiafulvalene and 7,7,8,8-Tetracyanoquinodimethane within the Skeletons of Metal-Organic Frameworks: Structures, Magnetism, and Electrochemistry. *Inorg. Chem.* **2019**, *58*, 8657−8664.
(210) Koo, J. Y.; Yakiyama, Y.; Lee, G. R.; Lee, J.; Choi, H. C.; Morita, Y.; Kawano, M. Selective Formation of Conductive Network by Radical-Induced Oxidation. *J. Am. Chem. Soc.* **2016**, *138*, 1776−1779.
(211) Panda, T.; Banerjee, R. High Charge Carrier Mobility in Two Dimensional Indium(III) Isophthalic Acid Based Frameworks. *Proc. Natl. Acad. Sci., India, Sect. A* **2014**, *84*, 331−336.

https://dx.doi.org/10.1021/acs.chemrev.9b00766
Chem. Rev. 2020, 120, 8536−8580

(212) Bhattacharya, B.; Layek, A.; Mehboob Alam, M.; Maity, D. K.; Chakrabarti, S.; Ray, P. P.; Ghoshal, D. Cd(II) Based Metal−Organic Framework Behaving as a Schottky Barrier Diode. *Chem. Commun.* **2014**, *50*, 7858−7861.
(213) Dolgopolova, E. A.; Galitskiy, V. A.; Martin, C. R.; Gregory, H. N.; Yarbrough, B. J.; Rice, A. M.; Berseneva, A. A.; Ejegbavwo, O. A.; Stephenson, K. S.; Kittikhunnatham, P.; et al. Connecting Wires: Photoinduced Electronic Structure Modulation in Metal−Organic Frameworks. *J. Am. Chem. Soc.* **2019**, *141*, 5350−5358.
(214) Kobayashi, Y.; Jacobs, B.; Allendorf, M. D.; Long, J. R. Conductivity, Doping, and Redox Chemistry of a Microporous Dithiolene-Based Metal−Organic Framework. *Chem. Mater.* **2010**, *22*, 4120−4122.
(215) Jiang, H.; Liu, X.-C.; Wu, Y.; Shu, Y.; Gong, X.; Ke, F.-S.; Deng, H. Metal-Organic Frameworks for High Charge-Discharge Rates in Lithium-Sulfur Batteries. *Angew. Chem., Int. Ed.* **2018**, *57*, 3916−3921.
(216) Bhattacharya, B.; Maity, D. K.; Layek, A.; Jahiruddin, S.; Halder, A.; Dey, A.; Ghosh, S.; Chowdhury, C.; Datta, A.; Ray, P. P.; et al. Multifunctional Mixed Ligand Metal Organic Frameworks: X-Ray Structure, Adsorption, Luminescence and Electrical Conductivity with Theoretical Correlation. *CrystEngComm* **2016**, *18*, 5754−5763.
(217) Maity, D. K.; Dey, A.; Ghosh, S.; Halder, A.; Ray, P. P.; Ghoshal, D. Set of Multifunctional Azo Functionalized Semi-conducting Cd(II)-MOFs Showing Photoswitching Property and Selective CO_2 Adsorption. *Inorg. Chem.* **2018**, *57*, 251−263.
(218) Halder, S.; Layek, A.; Ghosh, K.; Rizzoli, C.; Ray, P. P.; Roy, P. A Cd (II) Based Metal Organic Framework: A Photosensitive Current Conductor. *Dalt. Trans.* **2015**, *44*, 16149−16155.
(219) Halder, S.; Dey, A.; Bhattacharjee, A.; Ortega-Castro, J.; Frontera, A.; Ray, P. P.; Roy, P. A. Cd(II)-Based MOF as a Photosensitive Schottky Diode: Experimental and Theoretical Studies. *Dalt. Trans.* **2017**, *46*, 11239−11249.
(220) Dolgopolova, E. A.; Brandt, A. J.; Ejegbavwo, O. A.; Duke, A. S.; Maddumapatabandi, T. D.; Galhenage, R. P.; Larson, B. W.; Reid, O. G.; Ammal, S. C.; Heyden, A.; et al. Electronic Properties of Bimetallic Metal−Organic Frameworks (MOFs): Tailoring the Density of Electronic States through MOF Modularity. *J. Am. Chem. Soc.* **2017**, *139*, 5201−5209.
(221) Choi, J. H.; Choi, Y. J.; Lee, J. W.; Shin, W. H.; Kang, J. K. Tunability of Electronic Band Gaps from Semiconducting to Metallic States via Tailoring Zn Ions in MOFs with Co Ions. *Phys. Chem. Chem. Phys.* **2009**, *11*, 628−631.
(222) Ejegbavwo, O. A.; Martin, C. R.; Olorunfemi, O. A.; Leith, G. A.; Ly, R. T.; Rice, A. M.; Dolgopolova, E. A.; Smith, M. D.; Karakalos, S. G.; Birkner, N.; et al. Thermodynamics and Electronic Properties of Heterometallic Multinuclear Actinide-Containing Metal−Organic Frameworks with "Structural Memory". *J. Am. Chem. Soc.* **2019**, *141*, 11628−11640.
(223) Goswami, S.; Hod, I.; Duan, J. D.; Kung, C.-W.; Rimoldi, M.; Malliakas, C. D.; Palmer, R. H.; Farha, O. K.; Hupp, J. T. Anisotropic Redox Conductivity within a Metal−Organic Framework. *J. Am. Chem. Soc.* **2019**, *141*, 17696−17702.
(224) Kung, C.-W.; Otake, K.; Buru, C. T.; Goswami, S.; Cui, Y.; Hupp, J. T.; Spokoyny, A. M.; Farha, O. K. Increased Electrical Conductivity in a Mesoporous Metal−Organic Framework Featuring Metallacarboranes Guests. *J. Am. Chem. Soc.* **2018**, *140*, 3871−3875.
(225) Dawood, S.; Yarbrough, R.; Davis, K.; Rathnayake, H. Self-Assembly and Optoelectronic Properties of Isoreticular MOF Nanocrystals. *Synth. Met.* **2019**, *252*, 107−112.
(226) Huang, J.; He, Y.; Yao, M.-S.; He, J.; Xu, G.; Zeller, M.; Xu, Z. A Semiconducting Gyroidal Metal-Sulfur Framework for Chemiresistive Sensing. *J. Mater. Chem. A* **2017**, *5*, 16139−16143.
(227) Ahrenholtz, S. R.; Epley, C. C.; Morris, A. J. Solvothermal Preparation of an Electrocatalytic Metalloporphyrin MOF Thin Film and Its Redox Hopping Charge-Transfer Mechanism. *J. Am. Chem. Soc.* **2014**, *136*, 2464−2472.
(228) Liu, J.; Zhou, W.; Liu, J.; Howard, I.; Kilibarda, G.; Schlabach, S.; Coupry, D.; Addicoat, M.; Yoneda, S.; Tsutsui, Y.; et al. Photoinduced Charge-Carrier Generation in Epitaxial MOF Thin Films: High Efficiency as a Result of an Indirect Electronic Band Gap? *Angew. Chem., Int. Ed.* **2015**, *54*, 7441−7445.
(229) Duan, J.; Chen, S.; Zhao, C. Ultrathin Metal-Organic Framework Array for Efficient Electrocatalytic Water Splitting. *Nat. Commun.* **2017**, *8*, 15341.
(230) Usman, M.; Mendiratta, S.; Batjargal, S.; Haider, G.; Hayashi, M.; Rao Gade, N.; Chen, J.-W.; Chen, Y.-F.; Lu, K.-L. Semiconductor Behavior of a Three-Dimensional Strontium-Based Metal-Organic Framework. *ACS Appl. Mater. Interfaces* **2015**, *7*, 22767−22774.
(231) Tong, Y.-B.; Liu, S.-X.; Zou, Y.; Xue, C.; Duan, H.-B.; Liu, J.-L.; Ren, X.-M. Insight into Understanding Dielectric Behavior of a Zn-MOF Using Variable-Temperature Crystal Structures, Electrical Conductance, and Solid-State ^{13}C NMR Spectra. *Inorg. Chem.* **2016**, *55*, 11716−11726.
(232) Pathak, A.; Chiou, G. R.; Gade, N. R.; Usman, M.; Mendiratta, S.; Luo, T.-T.; Tseng, T. W.; Chen, J.-W.; Chen, F.-R.; Chen, K.-H.; et al. High-κ Samarium-Based Metal-Organic Framework for Gate Dielectric Applications. *ACS Appl. Mater. Interfaces* **2017**, *9*, 21872−21878.
(233) Ahn, D. Y.; Lee, D. Y.; Shin, C. Y.; Bui, H. T.; Shrestha, N. K.; Giebeler, L.; Noh, Y.-Y.; Han, S.-H. Novel Solid-State Solar Cell Based on Hole-Conducting MOF-Sensitizer Demonstrating Power Conversion Efficiency of 2.1%. *ACS Appl. Mater. Interfaces* **2017**, *9*, 12930−12935.
(234) Sahiner, N.; Sel, K.; Ozturk, O. F.; Demirci, S.; Terzi, G. Facile Synthesis and Characterization of Trimesic Acid-Cu Based Metal Organic Frameworks. *Appl. Surf. Sci.* **2014**, *314*, 663−669.
(235) Talin, A. A.; Centrone, A.; Ford, A. C.; Foster, M. E.; Stavila, V.; Haney, P.; Kinney, R. A.; Szalai, V.; El Gabaly, F.; Yoon, H. P.; et al. Tunable Electrical Conductivity in Metal-Organic Framework Thin-Film Devices. *Science* **2014**, *343*, 66−69.
(236) Goswami, S.; Ray, D.; Otake, K.; Kung, C.-W.; Garibay, S. J.; Islamoglu, T.; Atilgan, A.; Cui, Y.; Cramer, C. J.; Farha, O. K.; et al. A Porous, Electrically Conductive Hexa-Zirconium(IV) Metal−Organic Framework. *Chem. Sci.* **2018**, *9*, 4477−4482.
(237) Souto, M.; Calbo, J.; Mañas-Valero, S.; Walsh, A.; Minguez Espallargas, G. Charge-Transfer Interactions between Fullerenes and a Mesoporous Tetrathiafulvalene-Based Metal−Organic Framework. *Beilstein J. Nanotechnol.* **2019**, *10*, 1883−1893.
(238) Le Ouay, B.; Boudot, M.; Kitao, T.; Yanagida, T.; Kitagawa, S.; Uemura, T. Nanostructuration of PEDOT in Porous Coordination Polymers for Tunable Porosity and Conductivity. *J. Am. Chem. Soc.* **2016**, *138*, 10088−10091.
(239) Kung, C.-W.; Platero-Prats, A. E.; Drout, R. J.; Kang, J.; Wang, T. C.; Audu, C. O.; Hersam, M. C.; Chapman, K. W.; Farha, O. K.; Hupp, J. T. Inorganic "Conductive Glass" Approach to Rendering Mesoporous Metal−Organic Frameworks Electronically Conductive and Chemically Responsive. *ACS Appl. Mater. Interfaces* **2018**, *10*, 30532−30540.
(240) Guo, Z.; Panda, D. K.; Maity, K.; Lindsey, D.; Parker, T. G.; Albrecht-Schmitt, T. E.; Barreda-Esparza, J. L.; Xiong, P.; Zhou, W.; Saha, S. Modulating the Electrical Conductivity of Metal−Organic Framework Films with Intercalated Guest π-Systems. *J. Mater. Chem. C* **2016**, *4*, 894−899.
(241) Yin, Z.; Wang, Q.-X.; Zeng, M.-H. Iodine Release and Recovery, Influence of Polyiodide Anions on Electrical Conductivity and Nonlinear Optical Activity in an Interdigitated and Interpenetrated Bipillared-Bilayer Metal-Organic Framework. *J. Am. Chem. Soc.* **2012**, *134*, 4857−4863.
(242) Li, G.-P.; Zhang, K.; Zhao, H.-Y.; Hou, L.; Wang, Y.-Y. Increased Electric Conductivity upon I_2 Uptake and Gas Sorption in a Pillar-Layered Metal-Organic Framework. *ChemPlusChem* **2017**, *82*, 716−720.
(243) Schneider, C.; Ukaj, D.; Koerver, R.; Talin, A. A.; Kieslich, G.; Pujari, S. P.; Zuilhof, H.; Janek, J.; Allendorf, M. D.; Fischer, R. A. High Electrical Conductivity and High Porosity in a Guest@MOF Material: Evidence of TCNQ Ordering within Cu_3BTC_2 Micropores. *Chem. Sci.* **2018**, *9*, 7405−7412.

https://dx.doi.org/10.1021/acs.chemrev.9b00766
Chem. Rev. 2020, 120, 8536−8580

(244) Zeng, M.-H.; Wang, Q.-X.; Tan, Y.-X.; Hu, S.; Zhao, H.-X.; Long, L.-S.; Kurmoo, M. Rigid Pillars and Double Walls in a Porous Metal-Organic Framework: Single-Crystal to Single-Crystal, Controlled Uptake and Release of Iodine and Electrical Conductivity. *J. Am. Chem. Soc.* **2010**, *132*, 2561−2563.
(245) Zeng, M.-H.; Yin, Z.; Tan, Y.-X.; Zhang, W.-X.; He, Y.-P.; Kurmoo, M. Nanoporous Cobalt(II) MOF Exhibiting Four Magnetic Ground States and Changes in Gas Sorption upon Post-Synthetic Modification. *J. Am. Chem. Soc.* **2014**, *136*, 4680−4688.
(246) Hu, Y.-Q.; Li, M.-Q.; Wang, Y.; Zhang, T.; Liao, P.-Q.; Zheng, Z.; Chen, X.-M.; Zheng, Y.-Z. Direct Observation of Confined $I^-\cdots I_2\cdots I^-$ Interactions in a Metal-Organic Framework: Iodine Capture and Sensing. *Chem. - Eur. J.* **2017**, *23*, 8409−8413.
(247) Zhang, X.; da Silva, I.; Fazzi, R.; Sheveleva, A. M.; Han, X.; Spencer, B. F.; Sapchenko, S. A.; Tuna, F.; McInnes, E. J. L.; Li, M.; et al. Iodine Adsorption in a Redox-Active Metal−Organic Framework: Electrical Conductivity Induced by Host−Guest Charge-Transfer. *Inorg. Chem.* **2019**, *58*, 14145−14150.
(248) Hao, Z.; Yang, G.; Song, X.; Zhu, M.; Meng, X.; Zhao, S.; Song, S.; Zhang, H. A Europium(III) Based Metal-Organic Framework: Bifunctional Properties Related to Sensing and Electronic Conductivity. *J. Mater. Chem. A* **2014**, *2*, 237−244.
(249) Liu, B.; Zou, R.-Q.; Zhong, R.-Q.; Han, S.; Shioyama, H.; Yamada, T.; Maruta, G.; Takeda, S.; Xu, Q. Microporous Coordination Polymers of Cobalt(II) and Manganese(II) 2,6-Naphthalenedicarboxylate: Preparations, Structures and Gas Sorptive and Magnetic Properties. *Microporous Mesoporous Mater.* **2008**, *111*, 470−477.
(250) Lee, D. Y.; Kim, E.-K.; Shrestha, N. K.; Boukhvalov, D. W.; Lee, J. K.; Han, S.-H. Charge Transfer-Induced Molecular Hole Doping into Thin Film of Metal−Organic Frameworks. *ACS Appl. Mater. Interfaces* **2015**, *7*, 18501−18507.
(251) Lee, D. Y.; Lim, I.; Shin, C. Y.; Patil, S. A.; Lee, W.; Shrestha, N. K.; Lee, J. K.; Han, S.-H. Facile Interfacial Charge Transfer across Hole Doped Cobalt-Based MOFs/TiO_2 Nano-Hybrids Making MOFs Light Harvesting Active Layers in Solar Cells. *J. Mater. Chem. A* **2015**, *3*, 22669−22676.
(252) Neumann, T.; Liu, J.; Wächter, T.; Friederich, P.; Symalla, F.; Welle, A.; Mugnaini, V.; Meded, V.; Zharnikov, M.; Wöll, C.; et al. Superexchange Charge Transport in Loaded Metal Organic Frameworks. *ACS Nano* **2016**, *10*, 7085−7093.
(253) Chen, X.; Wang, Z.; Hassan, Z. M.; Lin, P.; Zhang, K.; Baumgart, H.; Redel, E. Seebeck Coefficient Measurements of Polycrystalline and Highly Ordered Metal-Organic Framework Thin Films. *ECS J. Solid State Sci. Technol.* **2017**, *6*, 150−153.
(254) Thurmer, K.; Schneider, C.; Stavila, V.; Friddle, R. W.; Leonard, F.; Fischer, R. A.; Allendorf, M. D.; Talin, A. A. Surface Morphology and Electrical Properties of Cu_3BTC_2 Thin Films Before and After Reaction with TCNQ. *ACS Appl. Mater. Interfaces* **2018**, *10*, 39400−39410.
(255) Melby, L. R.; Harder, R. J.; Hertler, W. R.; Mahler, W.; Benson, R. E.; Mochel, W. E. Substituted Quinodimethans. II. Anion-Radical Derivatives and Complexes of 7,7,8,8-Tetracyanoquinodimethan. *J. Am. Chem. Soc.* **1962**, *84*, 3374−3387.
(256) Huang, Q.-Q.; Lin, Y.-J.; Zheng, R.; Deng, W.-H.; Kashi, C.; Kumar, P. N.; Wang, G.-E.; Xu, G. Tunable Electrical Conductivity of a New 3D MOFs: Cu-TATAB. *Inorg. Chem. Commun.* **2019**, *105*, 119−124.
(257) Shiozawa, H.; Bayer, B. C.; Peterlik, H.; Meyer, J. C.; Lang, W.; Pichler, T. Doping of Metal−Organic Frameworks towards Resistive Sensing. *Sci. Rep.* **2017**, *7*, 2439.
(258) Sengupta, A.; Datta, S.; Su, C.; Herng, T. S.; Ding, J.; Vittal, J. J.; Loh, K. P. Tunable Electrical Conductivity and Magnetic Property of the Two Dimensional Metal Organic Framework [Cu(TPyP)-$Cu_2(O_2CCH_3)_4$]. *ACS Appl. Mater. Interfaces* **2016**, *8*, 16154−16159.
(259) Liu, J.; Wächter, T.; Irmler, A.; Weidler, P. G.; Gliemann, H.; Pauly, F.; Mugnaini, V.; Zharnikov, M.; Wöll, C. Electric Transport Properties of Surface-Anchored Metal−Organic Frameworks and the Effect of Ferrocene Loading. *ACS Appl. Mater. Interfaces* **2015**, *7*, 9824−9830.
(260) Liu, X.; Kozlowska, M.; Okkali, T.; Wagner, D.; Higashino, T.; Brenner-Weiß, G.; Marschner, S. M.; Fu, Z.; Zhang, Q.; Imahori, H.; et al. Photoconductivity in Metal-Organic Framework Thin Films. *Angew. Chem., Int. Ed.* **2019**, *58*, 9590−9595.
(261) Wang, Q.-X.; Zhang, C.-Y. Oriented Synthesis of One-Dimensional Polypyrrole Molecule Chains in a Metal-Organic Framework. *Macromol. Rapid Commun.* **2011**, *32*, 1610−1614.
(262) Yanai, N.; Uemura, T.; Ohba, M.; Kadowaki, Y.; Maesato, M.; Takenaka, M.; Nishitsuji, S.; Hasegawa, H.; Kitagawa, S. Fabrication of Two-Dimensional Polymer Arrays: Template Synthesis of Polypyrrole between Redox-Active Coordination Nanoslits. *Angew. Chem., Int. Ed.* **2008**, *47*, 9883−9886.
(263) Vernitskaya, T. V.; Efimov, O. N. Polypyrrole: A Conducting Polymer; Its Synthesis, Properties and Applications. *Russ. Chem. Rev.* **1997**, *66*, 443−457.
(264) Dhara, B.; Nagarkar, S. S.; Kumar, J.; Kumar, V.; Jha, P. K.; Ghosh, S. K.; Nair, S.; Ballav, N. Increase in Electrical Conductivity of MOF to Billion-Fold upon Filling the Nanochannels with Conducting Polymer. *J. Phys. Chem. Lett.* **2016**, *7*, 2945−2950.
(265) Brozek, C. K.; Dincă, M. Cation Exchange at the Secondary Building Units of Metal−Organic Frameworks. *Chem. Soc. Rev.* **2014**, *43*, 5456−5467.
(266) Deria, P.; Mondloch, J. E.; Karagiaridi, O.; Bury, W.; Hupp, J. T.; Farha, O. K. Beyond Post-Synthesis Modification: Evolution of Metal−Organic Frameworks via Building Block Replacement. *Chem. Soc. Rev.* **2014**, *43*, 5896−5912.
(267) Yoon, H.; Lee, S.; Oh, S.; Park, H.; Choi, S.; Oh, M. Synthesis of Bimetallic Conductive 2D Metal-Organic Framework (Co_xNi_y-CAT) and Its Mass Production: Enhanced Electrochemical Oxygen Reduction Activity. *Small* **2019**, *15*, 1805232.
(268) Gallego, A.; Hermosa, C.; Castillo, O.; Berlanga, I.; Gómez-García, C. J.; Mateo-Martí, E.; Martínez, J. I.; Flores, F.; Gómez-Navarro, C.; Gómez-Herrero, J.; et al. Solvent-Induced Delamination of a Multifunctional Two Dimensional Coordination Polymer. *Adv. Mater.* **2013**, *25*, 2141−2146.
(269) Yang, L.; He, X.; Dincă, M. Triphenylene-Bridged Trinuclear Complexes of Cu: Models for Spin Interactions in Two-Dimensional Electrically Conductive MOFs. *J. Am. Chem. Soc.* **2019**, *141*, 10475−10480.
(270) Herm, Z. R.; Wiers, B. M.; Mason, J. A.; van Baten, J. M.; Hudson, M. R.; Zajdel, P.; Brown, C. M.; Masciocchi, N.; Krishna, R.; Long, J. R. Separation of Hexane Isomers in a Metal-Organic Framework with Triangular Channels. *Science* **2013**, *340*, 960−964.

https://dx.doi.org/10.1021/acs.chemrev.9b00766
Chem. Rev. 2020, 120, 8536−8580